Novel Organic Polymer based Photodetector Structures

A Thesis

Submitted for the Degree of

Doctor of Philosophy

By

Th. Birendra Singh

Chemistry and Physics of Materials Unit
Jawaharlal Nehru Centre for Advanced Scientific Research
(A Deemed University)
Bangalore - 560064
INDIA

December 2003

JAWAHARLAL NEHRU CENTRE FOR ADVANCED SCIENTIFIC RESEARCH
Jakkur, Bangalore 560064, India

K. S. Narayan
Associate Professor
Chemistry and Physics of Materials Unit

PHONE: 91 80 8462750-57
FAX: 91 80 8462766
e-mail: narayan@jncasr.ac.in

19th Dec. 2003

Certificate

Certified that the work described in this thesis entitled **"Novel Organic Polymer based Photodetector Structures"** is the result of investigations carried out by Mr. Th. Birendra Singh under my supervision at the Molecular Electronics Laboratory, Chemistry and Physics of Materials Unit, Jawaharlal Nehru Centre for Advanced Scientific Research, Bangalore, India. Results presented in the thesis have not previously formed the basis for the award of any other diploma, degree or fellowship.

Prof. K. S. Narayan

DECLARATION

Bangalore, 19th Dec 2003

I hereby declare that the matter embodied in this thesis entitled, **"Novel Organic Polymer based Photodetector Structures"**, is the result of the investigations carried out by me in the Chemistry and Physics of Materials Unit, Jawaharlal Nehru Center for Advanced Scientific Research, Jakkur, Bangalore, India, under the supervision of Prof. K. S. Narayan.

In keeping with general practice of reporting observations, due acknowledgement has been made whenever the work described has been based on the findings of the other investigators. Any omission, which might have occurred by oversight or error of judgment, is regretted.

Th. Birendra Singh

Th. Birendra Singh

Dedicated to

My Parents

ACKNOWLEDGEMENT

I would like to place on record, my respect as well as gratitude for my guide, Prof. K. S. Narayan. Not only has he guided my research activities but also helped me develop. His sheer presence gives me untold enthusiasm and zeal to reach new heights. One striking aspect that is unique to him, is his mammoth knowledge coupled with his legendary speed; a sight that is obvious in all the activities he pursues. I consider myself among the privileged few who have had the privilege to be under his tutelage. I am grateful to him for the opportunities he has provided me.

I take this opportunity to thank Professors, C. N. R. Rao, FRS, S. Ramakrishnan, V. Krishnan, N. Mukunda and K. S. Valdia, K. Srihari for their help and timely guidance on various occasions.

I would like to thank all my course teachers in JNCASR as well as IISc, Prof. R. M. Vasu, Dr. K. S. Sanguni, Prof. J. Pasupathi, Dr. S. Balasubramanian, Prof. S. Natarajan, Dr. Shobhana Narasimhan and all the others for their guidance.

Thanks are due to Dr. Umesh Waghmare and Dr. N. Chandrabhas for their constant help and encouragement. The collaboration with Dr. Umesh Waghmare was very fruitful and informative.

I extend my gratitude to Prof. Mohan Rao, IISc, Bangalore, Prof. B. M. Arora, TIFR, Mumbai, Prof. P. Natarajan, NCUFP, Chennai, Dr. Govindacharalu, GAETECH Hyderabad, Dr. Narasimha Rao, IISc, Bangalore, Prof. A. J. Epstein of Ohio State University for timely help.

I thank my former and present colleagues, Dr. Alagiri, Dr. Geetha, Manoj, Soumya, Dinesh and Arun, My friends: Krishnan, Arpita, Gargi Raina, Lakshmi Ramakrishna, Anupama, Ashwin, Kavitha Siva, Aruna, Kruti, Shveta, Sanjeev, Uma, Kamala, Narayanan, Bishwa, Anand, Srikanth, Sarita, Umesh, Rohini, Harini, Sandeep, Partha, Geepee, Geeta, Robindro, Sophi, Itao, Shanta, Kantimoy, Satarupa, Dilip, Joykumar, Gagan, Ruhikant and rest of my friends for their never ending support and encouragement. Special thanks are due to Sonali for proof reading the thesis.

I would like to acknowledge the help rendered by the entire administrative, academic, library and computer lab staff.

I would like to thank all my teachers who taught me in every crucial steps of life. I want to thank Mr. B. Ramkrishna of Applied Optics, Inc. for his timely guidance in many occasions.

Last but not the least I would like to express my gratitude to my parents whose blessings and patience have been my strength throughout.

PREFACE

The thesis focuses on studies of polymer based photodetectors and covers the motivation, mechanisms, fabrication and modeling of these devices. The different approaches pursued include: (i) Nanoparticle TiO_2 dispersed conjugated polymer (CP) sandwich structures (ii) Microcavity structures consisting of an active CP layer (iii) Gated metal-CP-metal planar structures.

Photoconduction mechanism in a high electron affinity and Photodetection properties of nanocrystalline titanium dioxide, TiO_2, dispersed Poly-2-Methoxy-5-(2′-ethyl-hexoxy)-1,4 paraphenylenevinylene MEHPPV are studied. Responsivity as high as 50 mA/W is observed in the single-layered composite device. The spectral response is sensitive to the magnitude of the bias in the low-voltage range and the crossover from a symbatic to antibatic response is closely followed. At higher reverse bias, the response is relatively uniform throughout the entire spectral range. Differences in the switching response in the forward bias and reverse bias are observed with a pronounced effect of the persistence photocurrent in the forward bias.

In the second part of thesis a microcavity-enhanced photodiode, consisting of an active semiconducting-polymer layer poly,3-octylthiophene is studied in detail. The photodiode spectral response indicates features, which specifically arise from the cavity geometry factors, as expected from the simulation of the optical-field pattern within the cavity. The results indicate the tuning of photodetection energy range far below the band gap of semiconducting polymer along with sizable gain and speed.

In the third part we studied the changes in the transport mechanism of the photogenerated carriers in the semiconducting poly,3-hexylthiophene P3HT in the surface cell geometry upon insertion of schottky-type-metal strips between two electrodes. The direct evidence of the formation of charge depleted region upon contacting the polymer surface with certain metals viz. Al and Mg from in-situ measurements of lateral conductance, K. Enhanced photo-induced charge generation processes and manipulation of this structure for position sensitive device is also demonstrated. The structure also provides a model system to map the electric field from spatially resolved photocurrent measurements directly with the resolution controlled by the device dimensions and the optical-probe size.

LIST OF PUBLICATIONS

"*Nanocrystalline titanium dioxide dispersed semiconducting polymer photodetectors*", K. S. Narayan and **Th. B. Singh,** Appl. Phys. Lett., 74, 3456 (1999).

"*Photocurrent studies of an active polymer layer in a resonant microcavity*", **Th. B. Singh**, U. V. Waghmare, and K. S. Narayan, Appl. Phys. Lett., 80, 1213(2002)

"*Novel Strategies for polymer based light sensors*", K. S. Narayan, A.G. Manoj, **Th. B. Singh** and A. Alagiriswami, Thin Solid films, 417, 75(2002).

"*Photoinduced Relaxation Effects in 3-Terminal Polymer based device structures*", S. Dutta, **Th. B. Singh** and K. S. Narayan, Synth. Metals, 139, 553(2003)

"*Strategies for efficient photo-induced charge separation and transport in Semiconducting Polymer Systems*" K. S. Narayan, **Th. B. Singh**, A. G. Manoj, V. K. Basavaraj and S. Dutta. Proceedings of *Sixth International Conference on Optoelectronics, Fiber Optics and Photonics,* TIFR, Bombay, India 2002.

Manuscript in Preparation :

"*Gated phototransport across a metal polymer-semiconductor metal structure*", **Th. B. Singh** and K. S. Narayan,

Presentations at Conference:

"*Light Emission From Titanium Dioxide and Dye Dispersed Polymer*" **Th. B. Singh** and K. S. Narayan, presented at 5th International Conference in Asia, International Union of Materials Research Society, Indian Institute of Scince, Bangalore, India, 1998. (Oral)

"*High speed semiconducting polymer photodiodes*", **Th. B. Singh** and K. S. Narayan, presented at "5th International Symposium on Functional π-Electron Systems", Ulm /New Ulm, Germany, 30th May - 5th June, 2002. (Poster)

CONTENTS

Chapter

1

Section: 1

1.1.1 Introduction to Organic polymers

Organic materials are not traditionally associated with high electronic mobilities, but the past three decades have seen the rapid development of these materials as conductors and semiconductors, metals and superconductors [1]. Among the organic materials, the electronic and optical properties of conjugated polymers have received continuous attention over the past two decades. From a technological point of view, the semiconducting nature and the large optical-nonlinearities of these materials are of great interest, while from a fundamental point of view, the unusual excitations in these quasi-one-dimensional systems have stimulated much research [2].

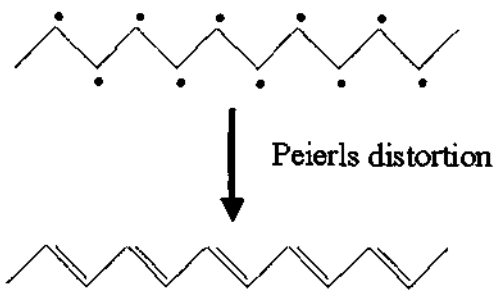

Figure 1.1: Due to Peierls distortion the unpaired electrons in the one-dimensional polyradical structure will bond into pairs leading to bond alternation, "conjugation", and the formation of a gap in the electronic density of states [3].

Undoped conjugated polymer chains are found with their ground state dimerized, which means that along the chain the carbon-carbon bonds have alternative length. In

chemical structures, this alternation is seen as an alternation of single (long) and double (short) bonds. This dimerization contributes to the gap in the electronic excitation as shown in Figure 1.1. Another contribution to this gap originates from the electron-electron interactions and is referred to as the Mott gap [4].

The genesis of the field can be traced back to the mid 1970s, when the first polymer capable of conducting electricity -- polyacetylene -- was reportedly prepared by accident by Shirakawa [5]. The subsequent discovery by Heeger and MacDiarmid [6], that the polymer undergoes an increase in conductivity of 12 orders of magnitude by oxidative doping quickly reverberated around the polymer and electrochemistry communities. An intensive search for other conducting polymers soon followed. The target was (and continues to be) a material which could combine the processibility, environmental stability and weight advantages of a fully organic polymer with the useful electrical properties of a metal.

The essential structural characteristic of all conjugated polymers is their quasi-infinite system extending over a large number of recurring monomer units. This feature results in materials with directional conductivity, which is strongest along the axis of the chain [7]. The simplest possible form is of course the archetype polyacetylene $(CH)_x$ shown in Figure 1.2. While polyacetylene itself is too unstable to be of any practical value, its structure constitutes the core of all conjugated polymers. Owing to its structural and electronic simplicity, polyacetylene is well suited to *ab initio* and semi-empirical calculations and has therefore played a critical role in the elucidation of the theoretical aspects of conducting polymers.

(a) (b) (c)

Figure 1.2: Conjugated polymer structure: (a) trans- and (b) cis-polyacetylene, and (c) polythiophene

It is generally agreed [8] that the mechanism of conductivity in these polymers is based on the motion of charged defects within the conjugated framework. The charge carriers, either *p*ositive p-type or *n*egative n-type, are the products of oxidation or reduction of the polymer respectively. The following overview describes these processes in the context of p-type carriers although the concepts are equally applicable to n-type carriers.

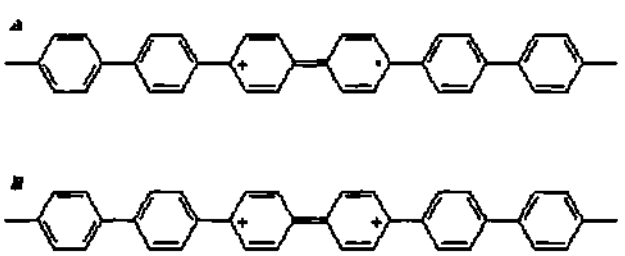

Figure 1.3: Positively charged defects on poly(p-phenylene). A: polaron B: bipolaron

Borrowing a terminology from chemistry, oxidation of the polymer initially generates a radical cation with both spin and charge. In the terminology of solid state physics, this species is referred to as a polaron and comprises of both the hole site and the structural distortion which accompanies it. This condition is depicted in Figure 1.3A. The cation and radical form a bound species, since any increase in the distance between them would necessitate the creation of additional higher energy quinoid units. Theoretical modeling and experimental observations [9,10] have demonstrated that, two nearby polarons combine to form the lower energy bipolaron shown in Figure 1.3B. One bipolaron is more stable than two polarons despite the coulombic repulsion of the two

ions. Since the defect is simply a boundary between two moieties of equal energy -- the infinite conjugation chain on either side, it can migrate in either direction without affecting the energy of the backbone, provided there is no significant energy barrier to the process. It is this charge carrier mobility that leads to the high conductivity of these polymers.

A polymer can be made conductive by oxidation of the material, either during synthesis or by addition of an oxidant to the freshly prepared polymer (p-doping) and/or, less frequently, reduction (n-doping) of the polymer. That is far more difficult to achieve and the materials are less stable than oxidized counterparts. Alternatively, charge carriers can be generated by protonation or deprotonation of suitable precursor polymer, the most successful example being p-doped polyaniline. At sufficiently high doping concentrations (10%), the mid-gap states themselves overlap sufficiently to form bands. This is referred to as the semiconductor-to-metal transition.

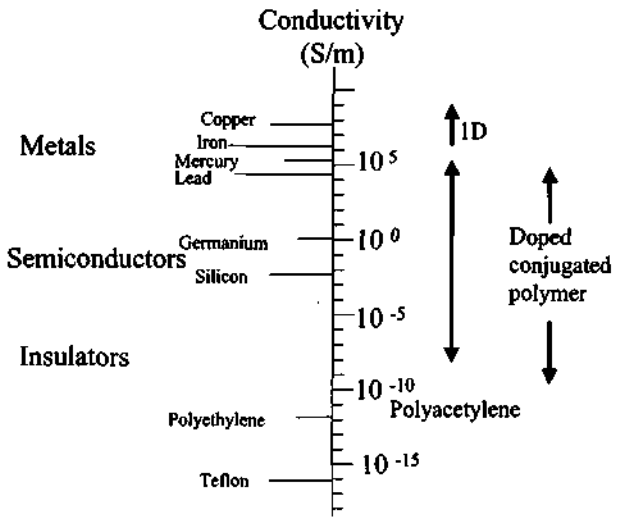

Figure 1.4: Comparison of the room temperature conductivity levels of doped conjugated polymers with conductance of other materials (From S. Roth [11])

1.1.2 Materials Overview

Most common semiconducting polymers used for photovoltiac devices are presented on Figure 1.5. Although the large possibility of positions of sidegroups and substituents seems to lead to an infinite number of conjugated polymers, almost all have two common properties. First of all, the conjugated polymer structure of the backbone is interrupted in one way or the other. In homopolymers the conjugated structure is interrupted naturally by the presence of interacting side groups, chemical defects, etc. In copolymers, conjugated structure of one of the subunits is also interrupted by the presence of the other. The second general property that almost all conjugated polymer have in common, is presence of large side group which improve the solubility of the material in common solvents. These two tools, interruption of the conjugation along the backbone and positioning of sidegroups, are used to realize polymers with the desired functionality.

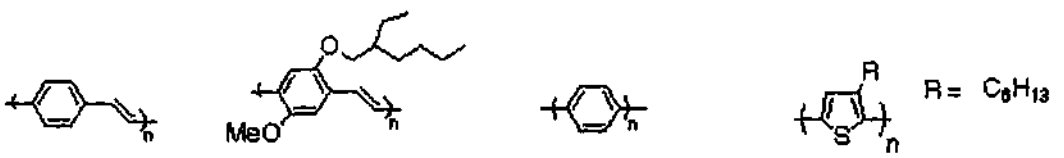

Figure 1.5: Most common semiconducting polymers available for devices: **(a) 'PPV'** Poly (1,4-phenylene vinylene) **(b)'MEHPPV'** Poly [(2-methoxy-5-(2'-ethyl hexyloxy)-1,4-phenylene) vinylene] (c)**'PPP'** Poly (p-phenylene) **(d) 'P3HT'**poly (3 hexyl thiophene)

The general structure of conjugated (polymeric) materials is characterised by alternating single and multiple (double or triple) bonds between the atoms that form the backbone of the polymer. Each carbon atom has a total of 4 valence electrons, 3 of which are place in sp^2 hybrid orbitals, which form covalent σ-bonds with neighboring C or H

atoms. The geometry of these σ-bonds is cylindrically symmetric electron-cloud joining the two nuclei involved.

1.1.3 Charge transport in conjugated polymeric conductors:

The absence of an ideal 3D lattice in thin film of conjugated polymers complicates the description of charge transport processes in terms of standard semiconductor models. Concepts used in the description of non-crystalline solids are of great help. It is obvious that the morphology of the polymer films on a microscopic scale will have large influence on their transport properties. The simple fact that the dimensions of an ordered segment of a polymer chain are very small compared to the inter electrode spacing, conductivity measurements almost naturally lead to a description of transport in terms of a hopping process or delocalization of charge carriers. This contributes to transport in a metallic state (in highly doped and conducting polymers). Central issues in this description are (i) The relative importance of inter-chain hopping sequences in relation to intrachain hopping between conjugated segments on the chain, and (ii) the nature of the transport sites within one polymer chain. The concept of band conduction by free electrons and holes does not apply to strongly disordered systems, like conjugated polymers. In these materials, charge carriers need to make transitions between localized states in the gap. A sequence of these inter-molecular transitions (inter or intra-chain) give rise to electrical conductivity with low carrier mobility.

Transport from site to site in a broad energy landscape (schematically indicated in Figure.1.6) is likely to be limited by inter-site hopping. The hopping probability between localized states will depend on the energy difference between the two states (thus the

height of the energetic barrier that a carrier has to overcome) and on the relative distance between the two sites involved. In the context of the Variable Range

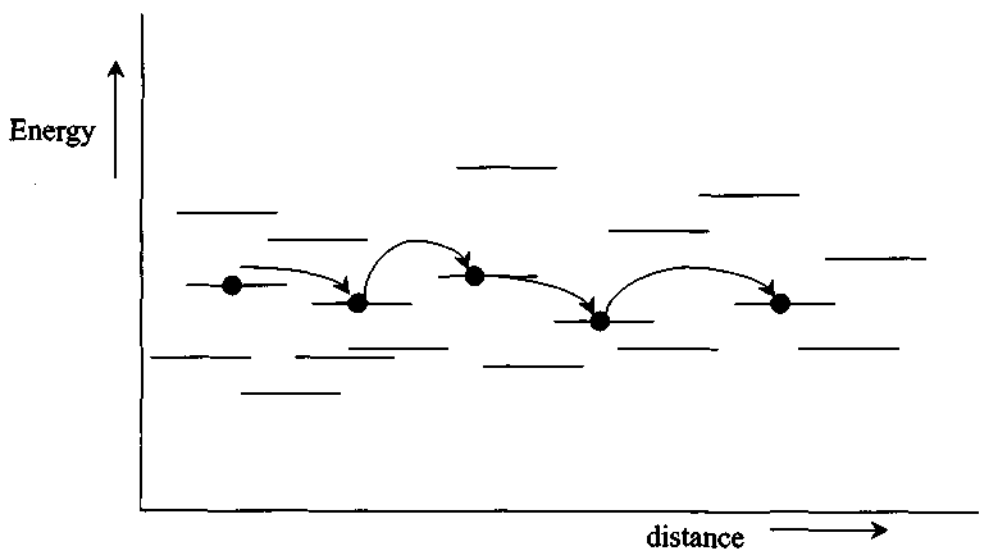

Figure 1.6: Schematic representation of hopping transport of a charge carrier through an ensemble of localized (molecular states).

Hopping- Theory [12] the probability of a hopping transition V_{hop} is given by

$$\nu_{hop} \propto \exp\left[-2\alpha R - (W \pm \varepsilon R)/K_b T\right] \qquad (1.1)$$

In which R is the intersite distance, α is the inverse spatial extension of the (localized) electron wave function W is the potential barrier that the electron needs to overcome, and ε is the external electric field strength. The term exp(-2αR) reflects the probability of being able to overcome the spatial separation between the two sites by quantum mechanical tunneling. The term exp(W/k_BT) is a Boltzmann factor which indicates the probability of an electron to overcome the barrier W thermally.

The jump is facilitated by the electric field term ($e\varepsilon R/K_BT$). Within Mott's variable range hopping theory [13], the general temperature dependence of the mobility μ is given by

$$\mu \propto \mu_0 \exp\left[-(T_0/T)^{\gamma}\right] \qquad (1.2)$$

In which γ is a factor which takes into account the dimensionality of the hopping process. The equation shows that upon increasing the temperature, the number of available states rises and the average hopping distance decreases. This results in a higher conductivity and for materials which has a higher conductivity. This equation should be adjusted for materials in which as a result of a strong electron-lattice coupling, the charge carrier to be transported should first be excited thermally to overcome an activation energy, E_a. In this case the mobility depends on the temperature as is described by equation 1.3 [12]:

$$\mu = \mu_0 \exp\left[-(T_0/T)^{\gamma} - (E_a / K_B T)\right] \qquad (1.3)$$

The temperature dependence predicted by equation 1.2 and 1.3, has been observed experimentally for doped poly(acetylene)s, confirming that these materials can be modeled as quasi one-dimensional semiconductors [14]. A number of modifications to this general theory have been proposed for conducting polymers [14,15].

In conjugated polymers the mobility has been reported to depend strongly on the electric field [16-17], especially in the high field regime. A description of the field dependence of the mobility, similar to the Poole-Frankel hopping model, but which has been adjusted for poly venyle carbozole (PVK) by Pai *et al.* [20] results in equation 1.4

$$\mu = \mu_0 \exp\left[\gamma E^{1/2}\right] \qquad (1.4)$$

in which μ_0 is the zero field mobility and γ is a prefactor similar to the one used in the Poole-Frankel description.

A direct measuremnt of the charge carrier mobility in conjugated polymers is quite complicated. The method used commonly is the time of flight (TOF) method, in which charge carriers are created optically at one of the electrodes. The drift of those photogenerated carriers by the applied electric field is measured by probing the current density as a function of time. The arrival time of the fastest carriers is directly related to the mobility μ by

$$\mu = d / Et \qquad (1.5)$$

in which d is the inter-electrode spacing (the thickness of the sample), t the arrival time of the fastest carrier and E is the electric field strength.

However the use of TOF methods, calls for a necessary conditions to be fulfilled, viz., the dielectric relaxation time must be higher than the charge carrier transit time ($\tau_\sigma >> \tau_{tr}$), through the inter-electrode spacing d.

Particularly in conjugated polymers this method is quite complicated as a result of generation of the two types of charge carriers upon photoexcitation, the uncontrolled width of the photogenerated region, and the dispersive character of the TOF-signal in low mobility materials. As has been argued by Binh *et al* [17], the charge carriers (originating from a photogenerated exciton upon dissociation) relax within the inhomogeneously broadened Density of States (DOS) on a time scale shorter than transit time.

In addition to this, several groups have shown that space charge effects play an important role in low mobility semiconductors. They also showed that build-up of space charge locally modifies the electric field strength. A build-up of space charge at one of the electrodes may also result in a modified injection current from the electrodes into the polymer. This further complicates the balance between electron and hole contributions to the signal.

1.1.4 Space charge limited current:

In low-mobility organic semiconductors, space charge effects determine the bulk transport properties in analogy to the situation in amorphous glasses and molecularly doped polymers. This regime is only manifested, in the absence of injection barriers, at the metallic contacts. This generally results in injection-limited current flow across the device. If however, Ohmic contacts are applied that are able to sustain the maximum current demand of the semiconductor, the current density through the device will be either ohmic or space charge limited. An ohmic dependence ($J \propto V$) will be observed when the injected charge density from the contacts is much smaller than the intrinsic carrier density under equilibrium conditions. In this regime the field distribution across the device is constant, and every injected carrier from the contacts will be transported similarly towards the opposite electrode. A space charge limited current (J), can be observed when the intrinsic charge density in the film is small compared to the injected current density. In this regime not all injected charge can be transported directly to the opposite electrode, which leads to a build-up of space charge in the film (and hence a non-uniform field distribution).

Under experimental conditions both regimes can be observed. The total current density through a device with two ohmic contacts will be

$$J = N_i(x)e\mu E(x) \qquad (1.6)$$

In which $N_i(x)$ and $E(x)$ are the position dependent density of injected charge carriers and the position dependent electric field strength, respectively. If $N_i(x)$ and $E_i(x)$ are mutually dependent (the field distribution is non-uniform as a result of space charge effects) integration of Poisson's equation will yield the current density through the film. The resulting dependence is known as Child's law. That is

$$J_{SCL} = 9/8\varepsilon_0\varepsilon_r\mu V^2/d^3 \qquad (1.7)$$

in which d is the film thickness and ε_r is the relative dielectric constant of the polymer film. In this case V is related to $E(x)$ by $V = \int E(x)dx$. A transition between the ohmic regime and the space charge limited regime will occur in the I-V characteristics at a transition voltage V_T, which is

$$V_T = (8/9)(eN_A d^2/\varepsilon_0\varepsilon_r) \qquad (1.8)$$

In which N_a is the intrinsic charge density in the film at thermal equilibrium.

In organic semiconducting polymers, SSLC have been observed in systems that do not contain large injection barrier at the contacts. Observation of the standard trap free behavior according to Child's Law (equation 1.7) can be observed for hole only devices. When the current density is dominated by electrons, the trap-free limit cannot be observed since deep carrier trapping into defects plays a role, reducing the electron-

mobility significantly. In this case an ohmic dependence at low voltages, changes above a critical voltage where the current increases sharply. This indicates that the trap-free limit is reached. For an exponential distribution of traps within the gap, equation 1.9 describes the trap density as a function of energy.

$$n_t(E) = (N_t/K_B t)\exp[E - E_C]/K_B T \qquad (1.9)$$

In this $n_t(E)$ is the trap density of states at energy E, E_c is the conduction band energy, N_t is the total trap density and ($K_B T$) is an energy characterizing the trap distribution. In the trap free limit this trap distribution leads to a current density, J according to:

$$J = N_c e\mu_n(\varepsilon_0\varepsilon_r/eN_t)^r\left(V^{r+1}/d^{2r+1}\right)C(r) \qquad (1.10)$$

where $r = (T_t/T)$ and N_c the effective density of states in the conduction band. The observation of hole-only and electron-only SCLC in polymeric semiconductor LEDs (21) proves that electrical characteristics are not necessarily dominated by injection from the metallic electrodes. It shows that the current density becomes bulk-limited if the injection barrier at the electrodes are minimized.

1.1.5 Device Prospect:

Conjugated polymers are a very attractive class of materials for industrial applications since they combine the flexible mechanical properties of polymers with semiconducting properties. By the mid-1980s, it was realized however that if π-conjugated polymers were going to succeed as commercial materials, their purity, solubility and processibility has to be improved. The lack of solubility and processibility and problems relating to the characterization, have been overcome by the attachment of

flexible alkyl chains to the conjugated backbone. Due to their improved purity, the device physics of the pure polymers has attracted more attention, since they can be exploited as the active semiconductor element in field-effect transistor (F. Garnier *et al*) [21], light emitting diode (J. H. Burrows *et al*) [22] and photovoltaic devices (G. Yu. *et al*) [23].

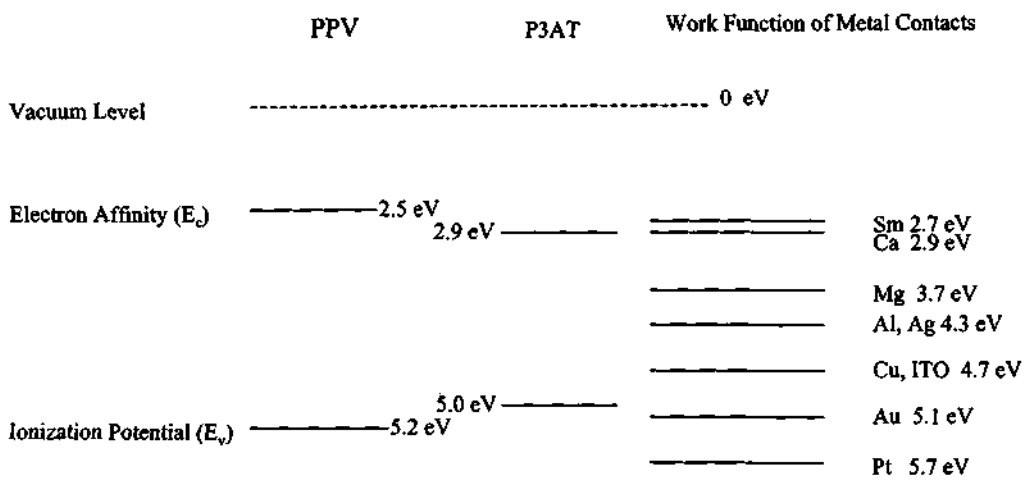

Figure: 1.7 Electron energy level diagram of PPV, P3AT and work function of selected contact metals used in polymer based devices.

Upon sandwiching a polymeric semiconductor between two different metallic electrodes (Figure 1.8) and applying an external voltage, a certain current density is achieved in the system, which varies with the applied bias. If the rectification is observed between the forward and reversed current densities, this should result from the dominating properties of one of the metal-semiconductor contacts, while a completely linear or symmetric IV-characteristics in a non-symmetric device outline would be indicative of bulk-dominated electrical properties. In this condition if this device is illuminated with light, it acts like a photovoltaic cell.

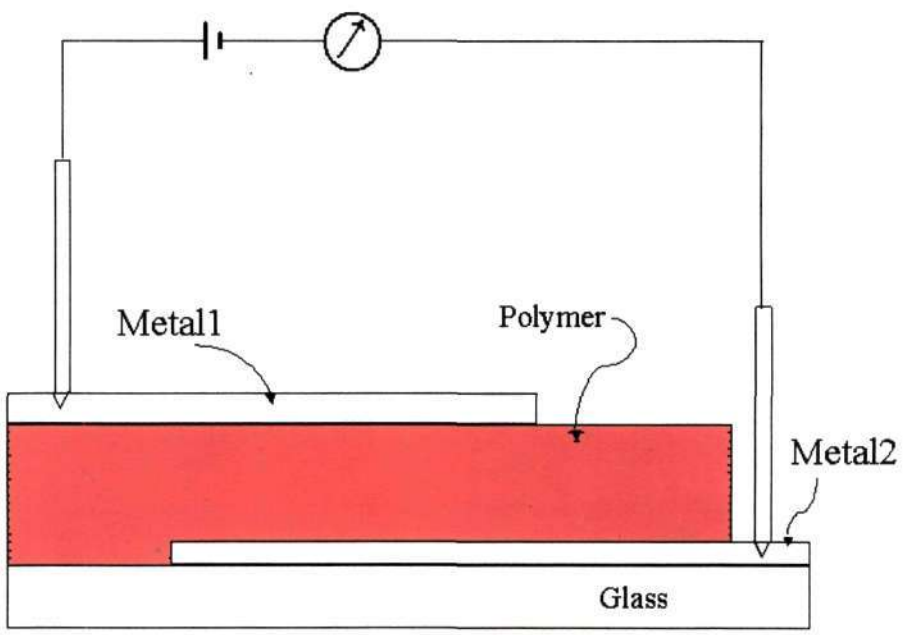

Figure 1.8: Basic single layer structure of a polymer device. The conjugated polymer is sandwiched between high-work function and low-work function metallic electrodes.

Upon photo-excitation the created charges have to be transported selectively to the contacts. The holes are transported by the polymer to the ITO contact and the electrons to the Al. Conjugated polymers show high mobilities along the chains but the mobility is limited by the hopping between the chains. The electrons are transported by the fullerene via a hopping [13] process. The most efficient charge separation is found for a cell containing 80 % fullerene [25,26]. Similar values are found for polymer solar cells with perylene acceptors [27,28]. For charge generation, a few percent would be sufficient. But the interconnection of all acceptor molecules in the bulk is of importance for efficient charge collection. Isolated fullerene molecules or clusters are charge traps and the electrons are captivated there. An easy and good model to describe a polymer diode is the metal-insulator-metal (MIM) diode, introduced by Parker for light emitting

diodes [29]. The polymer is assumed to have a negligible amount of intrinsic charge carriers and can therefore be seen as an insulator. It should be pointed out here, that this assumption is insufficient under illumination. For the contacts, tunneling injection diodes are assumed.

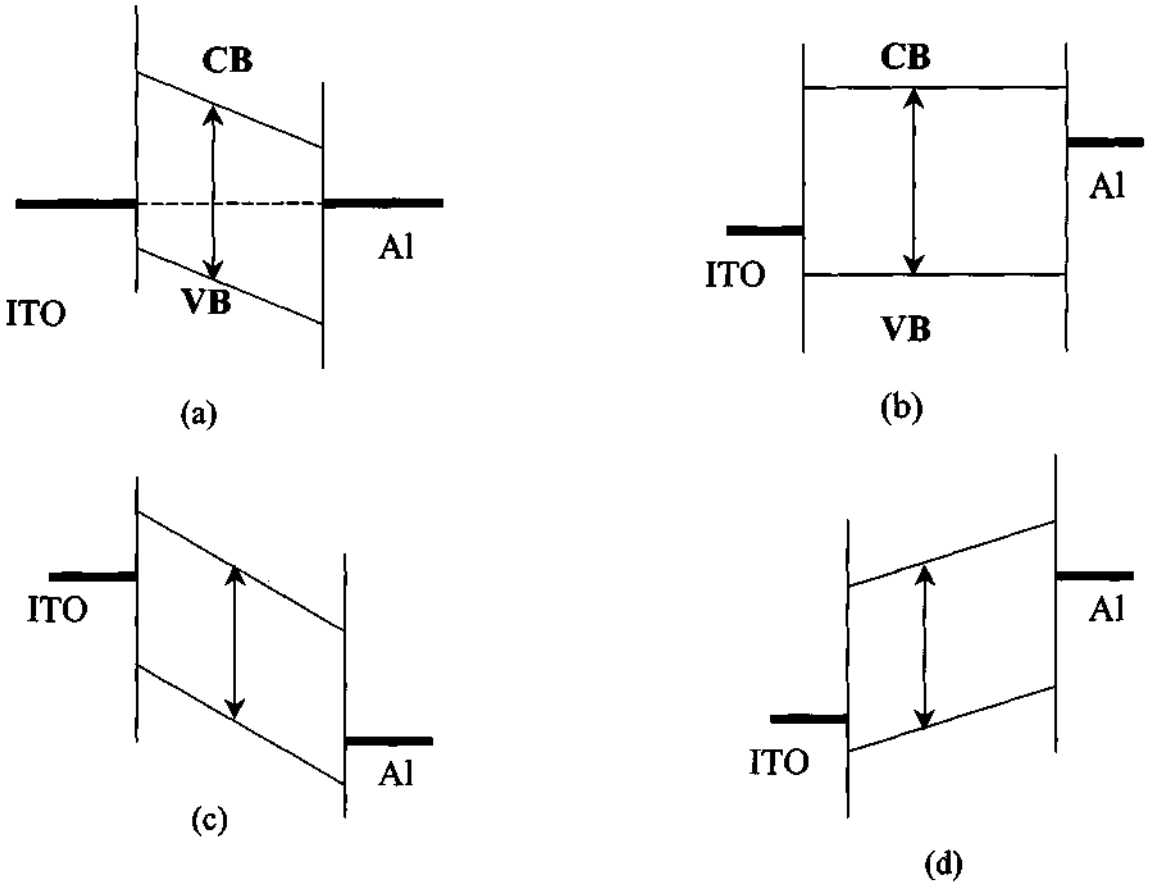

Figure 1.9: MIM picture for a polymer diode under different working conditions (a) short circuit, under illumination where the holes are transported to the ITO contact, the electrons to the Al contact, (b) Open circuit condition under illumination where the V_{OC} in the MIM picture is the work function difference between the two contacts, (c) diode under reverse bias, where the diode work as photodetector, and (d) diode under forward bias where diode can work as light emitting diode.

Figure 1.9 shows a pristine polymer device under different working conditions within the MIM picture. Figure 1.9(a) shows short circuit case, where holes created by photo-excitation transported to the ITO contact and electrons to the Al. The driving force for the separation of holes and electrons is the electric field across the polymer layer. The electric field is constant over the whole layer and is provided by work function difference of the contacts. Under open circuit conditions and illumination, (as is shown in Figure 1.9b), the created charges show no preferred direction. The open circuit voltage cancels the potential difference of the contacts. The maximal observed open circuit voltage V_{oc} is the work function difference between the two contacts. In the case of ITO and Al it is approximately 0.4 V.

In the case of a negative applied bias, i.e. positive contact to the Al and negative contact to the ITO, the diode works as photodetector [30-32] as shown in Figure 1.9. This transport is assisted by external field. Photo-induced charges are selectively transported to the contact electrodes. Holes are transported to the ITO and electrons to the Al. Polymer diodes are known to be very sensitive photodiodes. As an example, polythiophenes show quantum yields of 80 % under 15 V bias [33].

The MIM picture explains well the diode behavior of the devices as well as the solar cell activity of single layer devices. In the case of polythiophene, the work function is estimated to be of the order of 5.1 eV and we can expect an ohmic junction with gold (Φ_m=5.0 eV) but Schottky junction with chromium (Φ_m=4.5 eV), aluminum (Φ_m=4.3 eV) and indium (Φ_m=4.1 eV).

The formation of Schottky barrier at the Al/PPV interface was also observed [34]. The properties of the device studied by this group could be modeled by considering a

Schottky barrier junction at the cathode. The observation of a depletion layer at the Al interface and its dependence on the applied voltage, allows the estimation of the intrinsic hole concentration being as high as 10^{17} cm^{-3} [34]. Schwoerer *et al* [35] reported the photovoltaic effect in PPV Schottky diode with a power conversion efficiency between 0.1 to 1%, for devices with thickness varying from 100 to 500 nm at very low light intensitites.

Although the observations for PPV photodiodes of different groups are quite similar, there are still discussions going on the nature of the polymer-metal contacts and especially on the formation of space charge layer on the Al interface. According to Nguyen *et al* [36] band bending is caused by chemical reaction between the polymer and the metal, and is not directly related to Al deposition but may also be found in other metal/PPV interfaces. Traces of oxygen were found at the metal interface, however, in most of the XPS studies. According to Konstadinis *et al.* [37] oxygen on the surface of the polymer depletes the near surface region of vinylene group, thereby leaving the phenylene groups available for attack by metal atoms. Other models suggest that, photochemical oxidation of PPV results in scission of the polymer chain [38] or a possible reaction of the surface layer of Al with PPV to form covalent bonds [39], thereby generating an insulating barrier.

Understanding the factors influencing photogenerated charge carrier generation and transport, and their efficient collection, is one of the key requirements in optimizing the performance of polymer photovoltaic devices. The fundamental photophysical processes are in themselves of great current interest since they show a variety of novel physical phenomena. Some of these aspects will be investigated in this thesis.

Our aim is to understand the nature of photocarrier generation and transport in conjugated polymers from different system viz.: (i) blending of electron transport moities with conjugated polymers, (ii) ultrafast photoinduced carrier generation for application as fast photodetectors, and (iii) barrier on metal-polymer induced charge carrier generation for the application of position sensing detectors. To achieve this, a number of conjugated polymers have been studied. In the following section of this chapter a short introduction to the main topic dealt in this thesis, viz., photoconductivity, is given within the theoretical framework often used to describe the physics of conjugated polymers.

A dominant voltage drop at one of the electrodes of an ITO/poly(3-alkylthiophene)(P3AT)/Al structure results from band-bending at the electrode, this necessitates a modification of the rigid-band model introduced by Parker [29]. The strong band bending at the anode or cathode in combination with the non-uniform field distribution across the device, lead to the description of a metal/P3AT-contact in terms of the standard Schottky theory for metal/semiconductor contacts. The first description of a metal/P3AT-contact in terms of a Schottky contact between a metal and a p-type semiconductor, was proposed already in 1987 itself by Tomozawa *et al* [40].

When a very high work function electrode, Au is brought into contact with the p-type semiconductor P3AT, electrons will flow from P3AT into the anode to obtain charge equilibrium. This results in a positive space charge zone in the polymer close to the contact and band bending as indicated in Figure 1.10. In practice, however, the Au/P3AT barrier for holes is so small ($\phi_{b,h}=I_p-\chi$ = 5.0-4.9 = 0.1 eV) that it can be treated as an ohmic contact, where holes can pass the barrier when locally a low electric field has been

established. The work functions for Au and Al are average values based on handbook tables and literature reports, which yields (ϕ_{Au}=5 eV, ϕ_{ITO}=4.9 eV and ϕ_{Al}=4.3 eV).

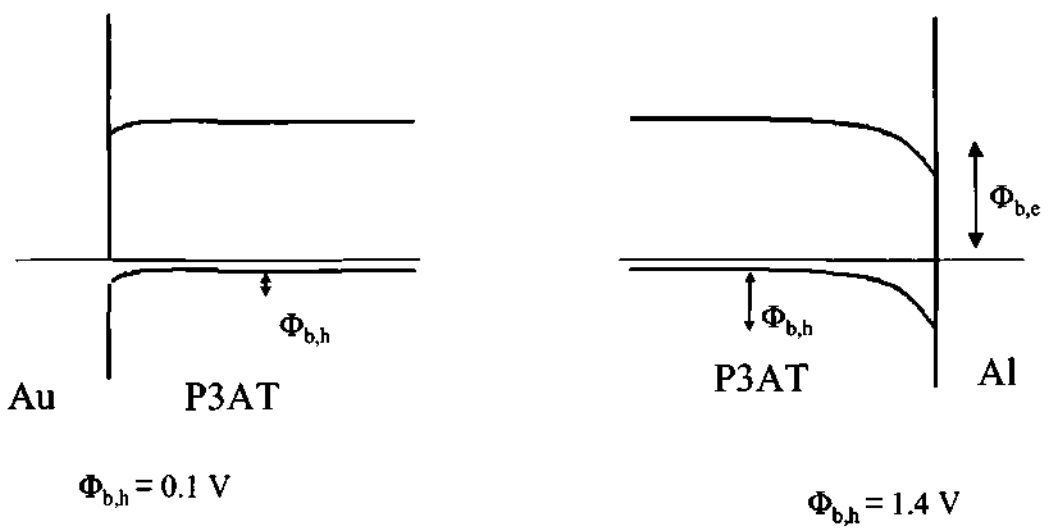

Figure 1.10: Schematic representation of band bending at the Au/P3AT and Al/P3AT.

The opposite situation occurs at the Al/P3AT electrode, where an electron-injecting barrier $\phi_{b,e}=\phi_s-\chi_s$ = 4.3-2.9 =1.4 eV is established at charge equilibrium. This situation is obtained as a consequence of the flow of electrons from the Al electrode into the semiconducting polymer film, establishing a hole-depletion zone in P3AT at the cathodic interface. A barrier of 0.7 eV for holes drifting from the polymer layer into the metal contact is established as a result of the interfacial band bending.

When a positive voltage is applied across the Al/P3OT contact (the positive voltage is applied to the ITO contact while the Al contact is grounded), two contributions to the total current are established; they are: (i) a drift current J_{dr}, of electrons in the strong electric field across the depletion zone and the diffusion zone, and (ii) a diffusion current J_d, the other way around. Thus total current density J at the contact becomes:

$$J = J_s\left[\exp(qV / nK_bT) - 1\right] \qquad (1.11)$$

and

$$J_s = A^{**}T^2 \exp(-q\phi_b/K_bT) \qquad (1.12)$$

where J_s is the saturation current density, V is the applied voltage, n is the ideality factor (equal to 1 for an ideal schottky contact), ϕ_b is the barrier height and A** is the so-called Richardson constant. The expression $exp(-q\phi_b/K_BT)$(Boltzmann factor) reflects the fraction of charges in the metal or semiconductor able to overcome the Schottky barrier by thermionic emission at a specific temperature T.

1.1.6 Modeling of Metal-Polymer Contact

Model: Band bending modified tunneling (BBMT) at the Ca/PPV Interface

Recently published studies suggest that charge injection into the polymer proceeds via tunneling across the barrier at the electrode/polymer interface. The heights of the individual barrier is equal to the difference in work function between the polymer and electrode material [29]. This model assumes that the polymer is fully depleted as a result of the low charge carrier density so that its bands are rigid. Therefore, charge movement normally associated with Schottky barrier formation should not occur at the metal/polymer interface. But the effect of charge transfer at the interface is the formation of a Schottky barrier, calling for the modification of the simple tunneling model.

Unlike the rigid band model previously proposed, the BBMT model postulates that charge transfer at the interface following metal deposition on the polymer produces a built-in electric field, which leads to the formation of a barrier at or near the interface. Support for the existence of this barrier comes not only from the direct measurement of charge transfer into the polymer by XPS, but also from capacitance measurement in

conjugated polymers [42]. From the I-V measurements of Parker [29], it has been found that, the externally applied field is much greater than the built-in field and the current predicted from the rigid band model matches the measured value reasonably well. However as externally applied field drops to a value comparable to that of the built-in field, the current predicted by the rigid band model deviates from the actual data [28]. This has been explained by invoking thermionic emission as a contributor to charge injection. However experimental evidence does not support this model, since the Richardson constant obtained gives a charge carrier mass, 5 orders of magnitude less than that of free charge carriers in polymers.

Although it is recognized that the charge distribution at the interface must satisfy Poisson's equation, it is also assumed for a first approximation, that the built-in electric field is nearly constant near the interface so that the resulting potential varies linearly with distance [41].

The contacts are the elementary building blocks of all the electronic devices. These include interface between semiconductors of different doping types, of different composition and junctions between a metal and a semiconductor, which can be either rectifying (Schottky junction) or ohmic. A metal-semiconductor junction results in an ohmic contact (i.e. a contact with voltage independent resistance), if the Schottky barrier is zero or negative. In such a case, the carriers are free to flow in or out of the semiconductor so that there is a minimal resistance across the contact. For a p-type semiconductor, it requires that the work function of the metal must be close to or larger than the sum of the electron affinity and the bandgap energy.

The electrical properties of these semiconductors and of the metal-semiconductor contacts have been discussed, in the light of fast-growing amount of experimental data, but so far a universal description of charge transport through polymeric LEDs has not been yielded. In order to optimize device performance, it is however very important to know the physics of carrier injection, transport and recombination in detail. Systematic ordering of the available experimental data is difficult, since device properties of organic semiconductor are known to be strongly dependent on fabrication conditions, environmental conditions, sample history, etc. A consistent description of electrical properties of these thin-film polymer devices is difficult as they are highly susceptible to the presence of interfacial layers, which may form unintentionally at the interface between conjugated polymers and metals, as a result of interfacial reactions and the influence of local dopants on the properties of the polymer.

1.1.7 Metal p-type semiconductor interface:

Already long ago, it was observed that a metal-semiconductor contact often shows rectifying properties. These were explained in 1938 by Schottky, to originate from a space charge layer established in the semiconductor close to the metallic contact.

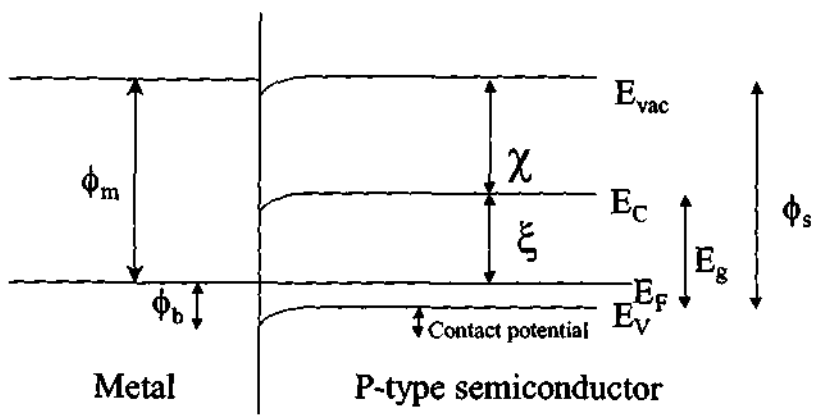

Figure 1.11: Conventional Schottky barrier band scheme for a p-type semiconductor against a low work function metal.

In the case of a p-type undoped organic polymers, an ideal Schottky barrier is formed between the semiconductor and a metal, with a work function Φ_m, that is lower than that of the semiconductor Φ_s, which is given by $\Phi_s = \chi + \zeta$ where χ is electron affinity (energy between the bottom of the conduction band and the vacuum level) and ζ is the energy between the Fermi level and the bottom of the conduction band. The bringing together of the two materials to form the junction must result in the equalization of the Fermi energies (for no applied bias across the junction), and this results in the formation of a dipole charge layer with positive charge density in the metal at the interface, and a region of negative charge density (the depletion region) formed by removal of the mobile positive charge carriers. Providing that the charge concentration in the metal is much greater than that in the semiconductor, all the band bending occurs in the semiconductor. This adjusts the potential between the two sides of the junction by the contact potential, which is given by $\chi + \zeta - \Phi_m$. This in turn sets up a barrier for the flow of holes towards the metal contact, Φ_b which measures from the Fermi energy, given by

$$\phi_b = (\chi + E_g) - \phi_m \qquad (1.13)$$

The potential barrier and its variation with an applied bias, determine the rectifying characteristics of the junction, as discussed below and in principle the barrier height is determined simply from the work functions of the metal and semiconductor. The dominant transport mechanism across the junction is usually considered to be emission of holes from the semiconductor over the top of the barrier into the metal. But quantum mechanical tunneling through the barrier, recombination in the space-charge region and recombination in the neutral region (electron injection) can also contribute [11].

Transport of holes over the barrier is limited by the rate at which they can diffuse through the depletion region (the diffusion model) and the rate at which they are able to cross the barrier (thermionic emission model). The standard result for the variation of the current density, J as a function of bias voltage, V, for the diffusion model is given by

$$J = qN_a \mu E_{max} \left(\exp\{qV/k_B T\}\right) - 1)\exp\{-q\phi_b / k_B T\} \qquad (1.14)$$

where q is the electronic charge, N_a is the concentrations of acceptors, μ the hole mobility, and E_{max} the maximum field in the depletion regime (19). E_{max} is given by

$$E_{max}^{\ 2} = \frac{2qN_a}{\varepsilon_o \varepsilon_r} \left(V_{do} - V\right)) \qquad (1.15)$$

Where V_{do} is the diffusion voltage at zero bias which is equal to ϕ_b-(E_f-E_v). Thus at high reverse bias the current does not saturate but increases as $|V|^{1/2}$.

For the case where current is limited by thermionic emission over the barrier, the current density, J, varies as

$$J = A^{**}T^2 \exp\{-q\phi_b / K_b T\}(\exp\{qV/k_B T\} - 1) \qquad (1.16)$$

where A** is the Richardson constant for thermionic emission modified by substitution

$$A^{**} = \frac{4\pi m^* q k_B^{\ 2}}{h^3} = 1.2 \times 10^6 \frac{m^*}{m_e} A\, m^{-2} K^{-2} \qquad (1.17)$$

of where m* is the semiconductor effective mass, m_e is the free electron mass.

The criterion for thermionic emission that limits current flow across the barrier is given by

$$lqE_{max} > k_B T \qquad (1.18)$$

where, *l* is the mean free path of the carrier in the semiconductor (33). This is equivalent to the criterion that, the mean free path must exceed the distance in which the barrier falls through an amount K_BT/q. In general, here we would expect that low carrier mobilities in the disordered polymeric materials to put the Schottky barriers formed with it in the regime of the diffusion-limited current.

In practice, the variation of *J*, with bias voltage is usually parameterised as

$$J = J_0\left(\exp\{qV/nK_B/T\}-1\right) \qquad (1.19)$$

where *n* is the ideality factor. This should be equal to 1 for the thermionic emission model, but is often found to be considerably larger. There are several possible explanations for this, including the possible role of an interfacial layer of insulator and semiconductor. At higher forward bias voltages, bulk limitations may start to play a role reducing the experimentally observed current density to a value lower than predicted by equation 1.19.

In addition to the thermionic contribution described here there is a small contribution from minority carriers to the current density determined by diffusion of holes from the metal into the semiconductor. This contribution however is orders of magnitude smaller than the thermionic component, and can therefore safely be neglected.

The charge present in the depletion region close to the metallic electrode behaves like the charge stored in a parallel plate capacitor, where the distance between the plates represents the width of the depletion layer. The extent of the depletion zone width and hence the capacitance C, changes with applied bias, as indicated in equation 1.20:

$$\frac{C}{A} = \sqrt{\frac{q\varepsilon_0\varepsilon_r N_a}{2}}\sqrt{\frac{1}{V_{d0}+V}} \qquad (1.20)$$

where A is the area of the junction.

From the experimental results, it is found that there is no true Schottky barrier formed at the interface between polymer and metal interface.

1.1.8 Fowler -Nordheim Tunneling Injection:

Electric field assisted injection of charge carrier into the transport bands of a semiconductor is another process that could result in contact-limited electrical characteristics. The classical Fowler-Nordheim theory [43] for direct tunneling of a charge carrier from the metal Fermi-level into the transport bands of the semiconductor [38] ignores image charge corrections. This leads to an IV characteristic described by:

$$J = BE^2 \exp(b/E), \qquad (1.21)$$

In which B is a prefactor and b depends on the barrier height ϕ and the effective mass m*. For a triangular barrier the factor b is

$$b = 4(2m^*)^{1/2}\chi^{3/2}/3he \qquad (1.22)$$

In which χ is the height of the triangular barrier. At low voltages these equations however are not expected to be valid, since in that regime the carrier tunneling length is to allow for direct tunneling. An alternative for direct tunneling is barrier penetration by a sequence of tunneling steps via localized states within the gap close to the Fermi energy. This process, described by Raikh *et al* [44] lead to an I-V characteristics described by

$$J \sim \exp(\gamma E^{1/2}) \qquad (1.23)$$

In this, γ depends on the barrier height, the effective mass and the probability for a carrier to find a localized state with an energy sufficiently close to the Fermi level energy.

Charge carrier injection, as described in the previous section, in any metal-semiconductor contact, is generally influenced largely by the properties of the metal (Fermi level position) rather than by the properties of the semiconductor (unless surface states or defect states in the semiconductor are prevented which pin the Fermi-level). In contrast, bulk limited charge transport depends on the properties of the active semiconductor itself, and is independent of the choice of the metal electrode.

References

1. Proceedings of the International Conference on Synthetic Metals, Santa Fe, New Mexico, June 1988, Synth. Metals **27-29,** 1998 (1989).

2. A. J. Heeger, S. Kivelson, J. R. Schrieffer, W. P. Su, Rev. Mod. Phys. **60,** 781 (1988).

3. R.E. Peierls, Quantum theory of solids (Oxford University Press, London, 1955) and Osaheni, J. A.; Jenekhe, S. A. Chem. Mater., **4**, 1282 (1992).

4. D. Baeriswyl, D. K. Campbell, S. Majumdar in Conjugated Conducting Polymers, (ed.: H. Kies), Springer, Berlin, 1992.

5 T. Ito, H. Shirakawa, S.J. Ikeda, Polym. Sci. Chem. Ed. **12**, 11 (1974).

6 C. K. Chiang, Y. W. Park, A .J. Heeger, H. Shirakawa, E. J. Louis, A.G. MacDiarmid, Phys. Rev. Lett. **39**, 1098 (1977).

7 J. Roncali, Chem. Rev. **92**, 711 (1992).

8 J. Heinze, Electronically Conducting Polymers in Topics in Current Chemistry, Vol. **152**; Springer-Verlag: Berlin, 1990.

9 T.C. Chung, J.H. Kaufman, A.J. Heeger, F. Wudl, Phys. Rev. B **30**, 702 (1984).

10 J. Brédas, R. Chance, R. Silbey, Phys. Rev. B **26**, 5843 (1982).

11 S. Roth, One Dimensional metals, VCH, Weinheim, 1995.

12. H. Bassler, M. Gailberger, R.F. Mahrt, J.M. Oberski, G. Weiser, Synth. Met. **49-50**, 341(1992).

13. N. F. Mott, E.A. Davis, Electronic Processes in Non-Crystalline Materials Clarenton, Oxford, 1979.

14. A.J. Epstein, H. Rommelmann, M. Abkowitz, H.W. Gibson, Mol. Cryst. Liq. Cryst. **77**, 81 (1981).

15. S. Kivelson, Phys. Rev. B **25**, 3798 (1982).

16 P. Kuivalainen, H. Stubb, H. I sotalo, P. Yli-Lahti, C. Holmstrom, Phys. Rev. B **31**, 7900(1985).

17 N. T. Bihn, L. Q. Minh, H. Bassler, Synth. Met. **58**, 39 (1993).

18 P. W. M. Blom, M. J. M. de Jong, M.G. Van Munster, Phys. Rev. B. **55**, 1 (1997).

19 J. M. Casado, J. J. Mejias, Phil. Mag. B **70**, 111 (1994).

20 D. M. Pai, J. Chem. Phys. **52**, 2285 (1970).

21 G. Horrowitz, D. Fichou, X.Z. Peng, Z. G. Xu, F. Gariner, Solid State Commun. **72**, 381 (1989).

22 J. H. Burroughes, D. D. C. Bradley, A. R. Brown, R. N. Marks, K. Mackay, R. H. Friend, P. L. Burns, A.B. Holmes, Nature **347**, 539 (1990).

23 G. Yu, J. Gao, J. C. Hummelen, F. Wudl, A. J. Heeger, Science **270**,1789 (1995).

24 P. W. M. Blom, M. J. M. de Jong, J.J.M. Vleggar, Appl. Phys. Lett. **68**, 3308 (1996).

25 S. E. Shaheen, C. J. Brabec, N. S. Sariciftci, Appl. Phys. Lett. **78**, 841 (2001).

26 C.J. Brabec, N.S. Sariciftci, Chapter 15 in Semiconducting Polymers edited by G. Hadziiannou and P. F. van Hutten, (2000), p. 515-560.

27 J. J. Dittmer, E.A. Marseglia, R.H. Friend, Advanced-Materials **12**, 1270 (2000).

28 J. J. Dittmer, R. Lazzaroni, P. Leclere, P. Moretti, M. Granstrom, K. Petritsch, E.A. Marseglia, R.H. Friend, J.L Bredas, H. Rost, A.B. Holmes, Solar Energy Materials And Solar Cells **61**, 53 (2000).

29 I.D. Parker, J. Appl. Phys. **75**, 1656 (1994).

30 N.S. Sariciftci, D. Braun, C. Zhang, V. I. Srdanov, A. J. Heeger, G. Stucky, F. Wudl, Appl. Phys. Lett. **62**, 585 (1994).

31 J.J.M Halls, C.A. Walsh, N.C. Greenham, E.A. Marseglia, R.H. Friend, S.C. Moratti, A.B. Holmes, Nature **376**, 498 (1995).

32 L.S. Roman, M.R. Andersson, T. Yohannes, O. Inganäs, Advanced Materials **9**, (1997).

33 G.Yu, K.Pakbaz, A.J. Heeger, Appl. Phys. Lett. **64**, 3422 (1994).

34 S. Karg, W. Reiss, M. Meiier, M. Schwoerer, Mol. Cryst. Liq. Cryst. **79**, 236 (1993).

35 W. Reisss, S. Karg, V. Dyakonoc, M. Meiier, M. Schwoerer, J. of Luminescence **906**, 60 (1994).

36 T.P. Nguyen, V. Masardier, V. H. Tran A. Guyot, Synth. Met. **235**, 55 (1993).

37 K. Konstadinidis, F. Papadimitrakopoulos, M. Galvin, R. L. Opila, J. Appl. Phys.**77**, 2645 (1995).

38 F. Papadimitrakopoulos, M. Yan, L. J. Rothberg, H.E. Katz, E.A. Chandross, M. E. Galvin, Mol. Cryst. Liq. Cryst. **256**, 669 (1994).

39 P. Dannetun *et al*, Synth. Met. **55-57**, 212 (1993).

40 H. Tomozowa, D. Braun, S. Philips, A.J. Heeger, H. Kroemer, Synth. Met. **22**, 63 (1987).

41 S. M. Sze, Physics of Semiconductor Devices, John Wiley and Sons, Inc. 1981.

42 E. Ettdgui, H. Razafitrimmo, Y. Gao, B. R. Hsieh, Appl. Phys. Lett. **67**, 2705 (1995).

43 R. H. Fowler, L. Northeim, Proc. R. Soc. London Ser. **A 119**, 173 (1928).

44 M. Raikh, X Wie, Mol. Cryst. Liq. Cryst. **256**, 563 (1994).

Section: 2

1.2.1 Photodetector:

Photodetectors are opto-electronic devices which convert optical signals into electrical signals through electronic processes. A general photodetector undergoes three processes (i) carrier generation by incident light, (ii) carrier transport and/or multiplication by whatever current-gain mechanism may be present, and (iii) interaction of current with the external circuit to provide the output signal.

When incident light falls on the surface of a semiconductor, carriers are generated either by band to band transition (intrinsic) or by transition involving forbidden-gap energy levels (extrinsic). An incident light whose photon energy is sufficient to generate photo-carriers will continuously lose energy to the semiconductor crystal lattice as the optical field propagates through the semiconductor. As illustrated in Figure 1.12, at the air-semiconductor interface, there is reflection loss due to the difference in refractive index. The Fresnel reflectivity for an optical signal at normal incidence to an interface between two materials is given by

$$R = \frac{(n_1 - n_2)^2}{(n_1 + n_2)^2} \qquad (1.25)$$

Where n_1= index of refraction of first material (for air n_1=1)

n_2= index of refraction of second material.

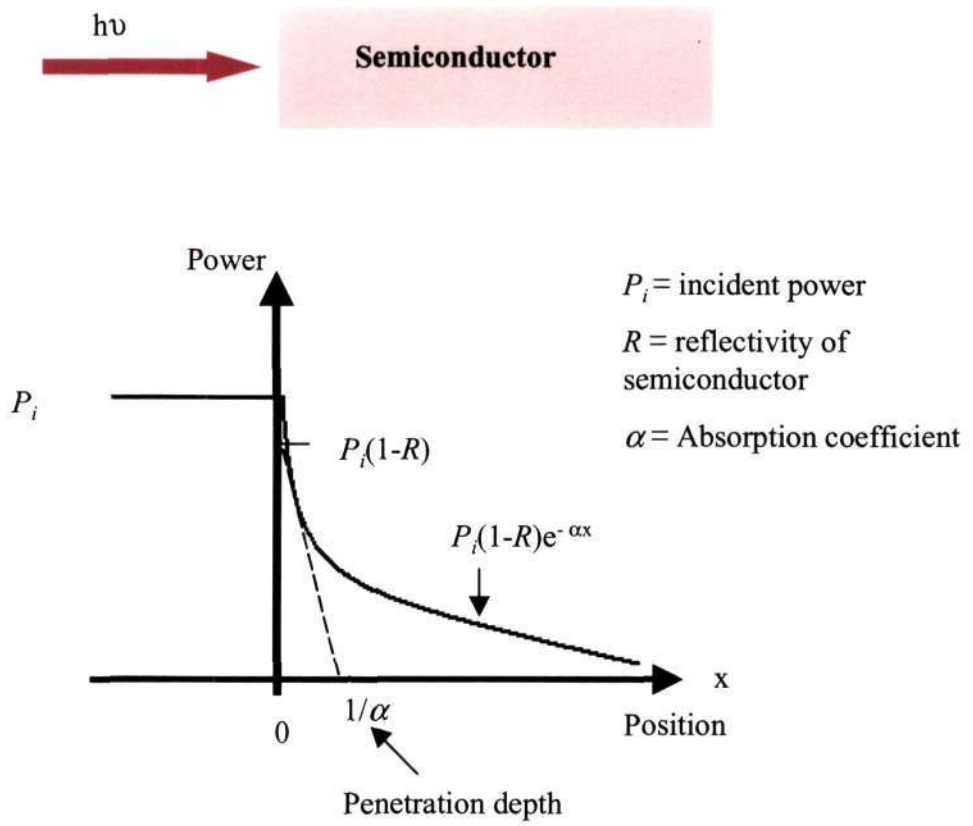

Figure 1.12: Optical absorption in a semiconductor.

Inside the semiconductor, the field decays exponentially as energy is transferred to the semiconductor. The material can be characterized by an absorption coefficient α, and a penetration depth $1/\alpha$. Penetration depth is the point at which $1/e$ of the optical radiation power remains.

The power in the optical field decays with distance. The amount of power absorbed in the semiconductor as a function of position within the material is then

$$P_{abs}(x) = P_i(1-R)\left(1-e^{-\alpha x}\right) \qquad (1.26)$$

The number of photons absorbed, is the power in watts divided by the photon energy ($E=h\nu$). If each absorbed photon generates a photocarrier (i.e., an electron-hole pair), the

number of photocarriers generated per number of incident photons, for a specific semiconductor with reflectivity R and absorption coefficient α, is given by

$$\eta(x) = \frac{\text{number of photocarriers produced}}{\text{number of incident photons}} = (1-R)(1-e^{-\alpha x}) \qquad (1.27)$$

where $0 \leq \eta(x) \leq 1$. This is an equivalent definition for photodetector's quantum efficiency.

Variation in the power in the incident optical field modulates the resistance of the photodetector, leading to the corresponding modulation of the current flow, i_{photo}, in the circuit. Once incident photons cause charge carriers to form, the in-build electric field or externally applied electric field causes the carriers to move towards the electric terminals. The net result is a reduction in the resistance of the materials, which allows an increase in the current circulating in the detector circuit.

The photogenerated carriers do not last indefinitely. There is an associated lifetime, that is a measure of the average time it takes for the carriers to recombine. The photocurrent generated in a photoconductor, illuminated by an optical signal field of average power P_{rcvd}, is influenced by both the carrier lifetime and the time the carriers require to make their way through the device. The photocurrent is given by

$$i_{photo}(t) = \frac{\eta q}{h\nu}\left[\frac{\tau_{carrier}}{\tau_{transit}}\right] P_{recd}(t) + i_{dark} \qquad (1.28)$$

where $\eta q/h\nu$ = R= responsivity of the semiconductor material, $\tau_{carrier}$ = mean carrier lifetime, $\tau_{transit}$= transit time between the electrical contacts, i_{dark}= dark current.

The dark current flows regardless of the amount of illumination present and is a form of leakage current. We can define a photocurrent gain term G, given by

$$G = \frac{\tau_{carrier}}{\tau_{transit}} \tag{1.29}$$

$$\tau_{transit} = \frac{l_d}{v_s} = \frac{l_d}{\mu E_s} \tag{1.30}$$

where l_d = thickness of the absorbing region, v_s = average carrier saturation velocity. One way to achieve performance is to first engineer the semiconductor so that the carrier lifetime is as long as possible, while still maintaining adequate bandwidth. The photocurrent gain is then increased by decreasing the transit time as much as possible.

Photodiodes can be operated in an unbiased mode or they can be operated under either a forward or a reverse bias. These three different bias schemes correspond to the three modes in which a photodiode can be operated when connected to an external circuit. Figure 1.13 illustrates the three modes. They are commonly referred to as open-circuit "photovoltaic" operation, short circuit " photoconductive" operation, and reverse-biased "photoconductive" operation.

1.2.2 Different types of photodetectors are outlined here:

(i) Phototransistor (ii) Photovoltaic cell, (iii) Charge Coupled Detector (CCD), (iv) Metal- Semiconductor-Metal (MSM) Photodiode, (v) Position Sensitive *photo*Detector (PSD), (vi) Resonant Cavity Enhanced (RCE) Photodiode, (vii) Photodiode, (viii) Avalanche Photodiode (APD), and (ix) Photomultiplier Tube (PMT).

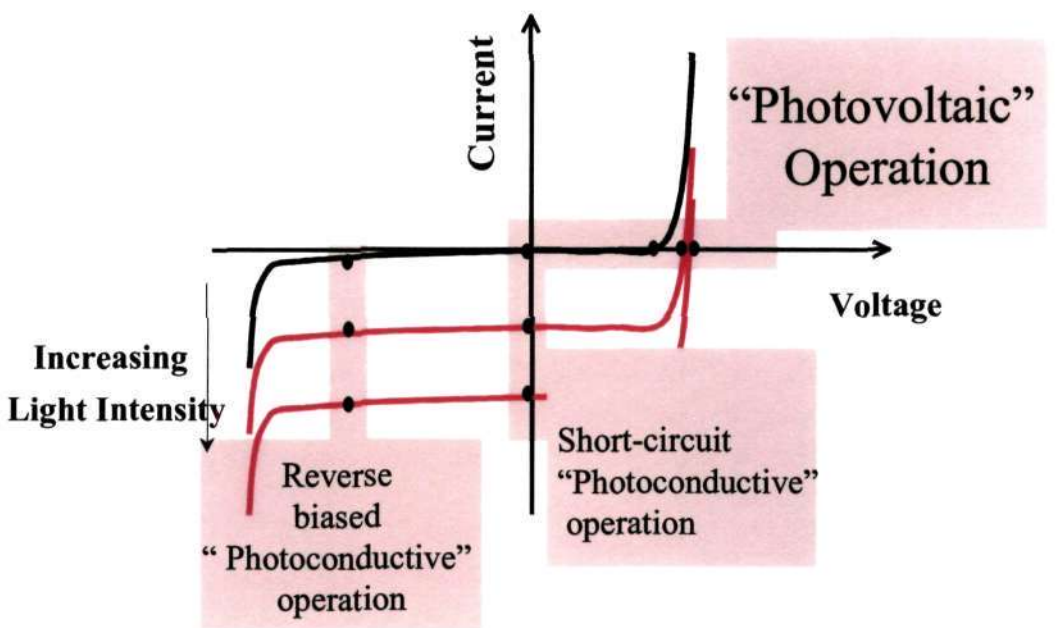

Figure 1.13: Operating regions of a photodiode. (a) Open-Circuit " Photovoltaic." (b) Short-circuit " photoconductive." (c) Reverse-biased " photoconductive."

1.2.3 Figure of merit for photodetectors are:

(i) Low dark current, (ii) High ratio of photocurrent to dark current, (iii) High cutoff frequency, (iv) Wide spectral response, (v) Low noise equivalent power, (vi) High Photoresponsivity, and (vii) Good linearity of photocurrent and intensity of light incident.

1.2.4 Photoconductivity:

Photoconductivity has proven to be an important method for providing fundamental information regarding the nature of the photoexcitations. By comparing the spectral response of both steady state and fast transient photoconductivity with the absorption spectrum, one can demonstrate whether free charge carriers or bound excitons are photo-generated. In particular, picosecond transient photoconductivity studies offer the possibility of monitoring the generation and transport of charge carriers before their

transport is significantly limited by traps. Intensity dependence and temperature dependence studies provide additional information relevant to the photo-generation and transport mechanisms. The description of the phenomena of photoconductivity focuses on the definition of three basic quantities: the photoconductivity, the spectral response, speed of the response and electronic transition due to absorption of light [1].

In organic polymers, the fact that the onset of photoconductivity occurs at a higher energy than the absorption edge in most conjugated polymers, is a clear indication that the photoexcitations generated below the absorption edge are neutral excitons.

On the contrary, in the PPVs, the onset of photoconductivity coincides with the onset of absorption. In the PPVs, mobile charge carriers are photogenerated. In the exciton picture, however, this coincidental onset of photoconductivity and absorption must be explained as an artifact. Initially excitons are photogenerated with subsequent dissociation as a result of secondary processes.

The photocurrent spectral response of a device structure of ITO/Polymer/Al can be better understood on the basis of the following model. The original assumptions of the model are as following:

(i) Photoexcitation produces both free electrons and holes or atleast excitons which immediately form free carriers in the bulk, e.g., by interaction with impurities or traps.

(ii) The most photosensitive region is the region at the aluminum/polymer interface.

(iii) The photocurrent depends on the ability of the minority carrier (electrons) to reach the interface, which acts as a sink for them. Otherwise, the build-up of space charge will occur within the bulk of the film, impeding charge transport.

However, the model can be applied to either diffusing charge carriers or diffusing excitons. Within the excitonic picture, assumption (iii) is supplemented by the requirement of excitons to reach the aluminum electrode to undergo dissociation and produce charge carriers.

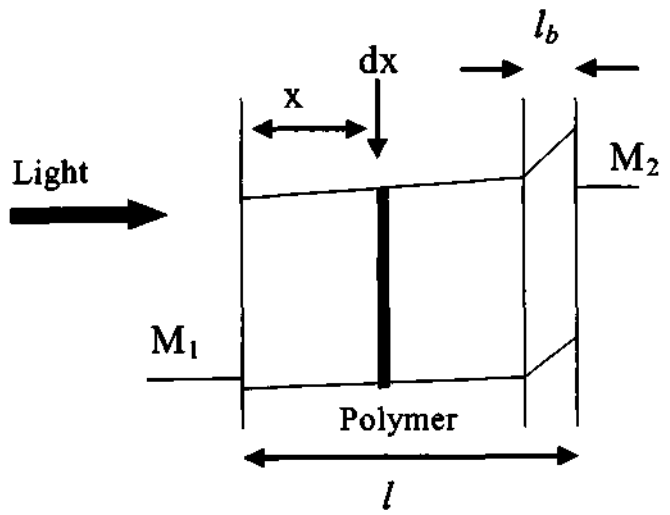

Figure 1.14: Schematic of the cross section of the device, for the model of Ghosh *et al* (1974) [3] for illumination from the side furthest from the barrier region (i.e., from x>0). The total polymer thickness is denoted as l while the thickness of the barrier layer is denoted by l_b with L the effective diffusion length of carriers.

The rate of generation of charge carriers in the bulk, at distance x from the illuminated electrode, is taken to be proportional to the light intensity at x and is given by

$$\frac{dn}{dt} = \theta I_0 \alpha \exp(-\alpha x) \qquad (1.31)$$

where I_o is the number of incident photon cm^{-2} sec, α is the absorption coefficient (cm^{-1}), and θ is the quantum efficiency.

The number of photogenerated carriers within dx, at a distance x from the surface, is proportional to

$$\theta I_0 \alpha \exp(-\alpha x) dx \tag{1.32}$$

The carriers generated at a distance x will have a fraction proportional to

$$\exp[-\beta(l - l_b - x)]\alpha \exp(-\alpha x) \tag{1.33}$$

diffuse to the barrier, where $1/\beta$ is the diffusion length and l_b the barrier width. The total number of carriers n at the barriers is given by

$$n = \int_0^{l-l_b} \theta I_0 \alpha \exp(-\alpha x) \exp[-\beta(l - l_b - x)] dx \quad \text{(bulk)}$$
$$+ \int_{l-l_b}^{l} \theta I_0 \alpha \exp(-\alpha x) 1 dx \quad \text{(barrier)} \tag{1.34}$$

The first term denotes the number of carriers reaching the barrier from the bulk and second term, the carriers generated within the barrier. On integrating we have,

$$n = \int_0^{l_b} \theta I_0 \alpha \exp(-\alpha x) \quad \text{(barrier)}$$
$$+ \int_{l_b}^{l} \theta I_0 \alpha \exp(-\alpha x) \exp[-\beta(x - l_b)] dx \quad \text{(bulk)} \tag{1.35}$$

The model of DeVore [5]; Ghosh and Feng (1974) [6]; and Desormeaux, Max, and Leblanc [7] all share the same diffusion equations. Once formed, charge carriers either leave by diffusion or recombination. The rate of change of charge carrier density at a depth x, is therefore given by the equation 1.36. In this the first term represents photogeneration, the second term represents carriers moving away by diffusion and the third term is recombination of charge carriers on a time scale given by τ, the bulk recombination lifetime.

$$\frac{dn(x)}{dt} = \theta I_0 \alpha \exp(-\alpha x) - \frac{di}{dx} - \frac{n}{\tau} \tag{1.36}$$

At equilibrium, the charge density does not change with time, so *dn(x)/dt* is zero. By setting the time derivative *dn(x)/dt* to zero and recalling the diffusion constant, a time dependent second-order differential equation is obtained for the steady state distribution of carrier density, as shown in 1.37

$$\frac{d^2 n(x)}{dx^2} = \frac{n}{D\tau} - \frac{\theta I_0 \alpha \exp(-\alpha x)}{D} \tag{1.37}$$

Note that in the models of Ghosh and Feng [6] and Desormeaux, Max, and Leblanc [7], the diffusion equation 1.36 and 1.37 can also be applied to diffusion of excitons, when *n(x)* represents the exciton density.

Equation 1.37 has the general solution given by equation

$$n(x) = B\exp(-\beta x) + C\exp(\beta x) + \frac{\theta I_0 \alpha \exp(-\alpha x)}{D(\beta^2 - \alpha^2)} \tag{1.38}$$

Where $\beta = 1/\sqrt{(D\tau)}$ is the reciprocal of the diffusion length. The values of the coefficients B and C, depend on the boundary conditions, which are different for each model.

This model was developed to account for the photoconductivity action spectra of inorganic semiconductors, in which photoexcitations result directly in the formation of pairs of free electrons and holes. Recombination of free electrons and holes can occur in the bulk after a mean lifetime τ, or at either surface at a rate which is represented by a recombination of current $i_R = n_s S$, where n_s is the density of electron-hole pairs at the

surface and S is the surface recombination velocity. When the thickness of the film is comparable with the reciprocal of the maximum velocity S [much greater than the bulk recombination rate, $\beta D=\sqrt{(D/\tau)}$] , it results in an antibatic response, while a low surface recombination rate gives a symbatic response.

The diffusion equation 1.37 is solved for two boundary conditions, given in equation 1.39 and 1.40, from which expression for B and C can be obtained. At the illuminated surface,

$$(i_R)_0 = -D\left(\frac{dn}{dx}\right)_{x=0} = -n_0 S \qquad (1.39)$$

At the far surface,

$$(i_R)_l = -D\left(\frac{dn}{dx}\right)_{x=l} = -n_l S \qquad (1.40)$$

The coefficients B and C are then given as in equation 1.41 and 1.42

$$B = \frac{\theta I_0 \alpha / D}{(\beta^2 - \alpha^2)}\left\{\frac{(S-\alpha D)(D\beta - S)\exp(-\alpha l) + (S+\alpha D)(D\beta + S)\exp(\beta l)}{(D\beta - S)^2 \exp(-\beta l) - (D\beta + S)^2 \exp(\beta l)}\right\} \qquad (1.41)$$

$$C = \frac{\theta I_0 \alpha / D}{(\beta^2 - \alpha^2)}\left\{\frac{(S-\alpha D)(D\beta + S)\exp(-\alpha l) + (S+\alpha D)(D\beta - S)\exp(-\beta l)}{(D\beta - S)^2 \exp(-\beta l) - (D\beta + S)^2 \exp(\beta l)}\right\} \qquad (1.42)$$

The increase in conductivity is assumed to be proportional to the total number of carrier pairs, i.e., the integral of the carrier density over the length of the film, as in equation 1.43.

$$N = \int_0^l n(x)dx = \frac{1}{\beta}\{B(1-\exp(-\beta l)) + C(\exp(\beta l) - 1)\} + \frac{\theta I_0 \alpha / D}{\alpha(\beta^2 - \alpha^2)}(1-\exp(-\alpha l)) \qquad (1.43)$$

This only strictly applies to surface-cell configuration.

The photoconductivity $\sigma_{ph,}$ is then given by expression $\sigma_{ph}=N/I_o\tau$, and simplifies to the expression given in equation (1.42), again only valid for a surface cell geometry.

$$\sigma_{ph} = \frac{1-\exp(-\alpha l)}{1+(S/\beta D)\coth(\beta l/2)} \times \left\{1+\frac{(S/\beta D)\beta[\beta\coth(\beta l/2)-\alpha\coth(\alpha l/2)]}{\beta^2-\alpha^2}\right\} \qquad (1.44)$$

As noted in an appendix of a publication by Greg, Fox, and Bard [8], it may not be appropriate to integrate the charge density across the film when calculating the photocurrent action spectrum for a sandwich cell geometry. When mobilities of the charge carriers are low, it may in fact be more appropriate to consider the variation of resistance along the thickness of the film. These are viewed as several resistance along the thickness of the film, arranged in series. The conductivity of the film in the sandwiched cell geometry, is determined by the most resistive sections rather than the most conductive one. In this case, it is more appropriate to integrate the resistance of each differential length element across the film thickness, rather than integrating the charge density.

Therefore the De Vore theory [5] is adapted to sandwich cell geometry. The method is the same up to the derivation of the charge carrier density equations, 1.37-1.40. The photocurrent in the sandwich cell is then the integral of the resistivity, as in equation 1.45.

$$\sigma_{ph}(\alpha) \propto \frac{1}{\int_0^l \frac{1}{n(\alpha,x)}dx} \qquad (1.45)$$

where carrier density $n(x)$ is given by equation 1.38-1.40.

As expression has no solution, to use this equation, one has to perform the integration numerically, dividing the film thickness into 200 steps and optimizing the parameters β, S and D to minimize the sum of the squared difference between experimental and simulated profiles.

An antibatic photocurrent response can occur, because the photocurrent is limited by the most resistive region, which is generally furthest from the illumination. Hence weakly absorbed light can penetrate throughout the film. Assuming intrinsic carrier generation, this results in generation of charge carriers throughout the film. Conversely, strongly absorbed light does not penetrate far into the film. Thus, while it can generate a high charge density close to the illuminated electrode, the remaining film, beyond a *1/e* light penetration depth of approximately 30 nm, is much more resistive. Therefore, for relatively thick films, the model predicts a maximum photocurrent peak in the low energy tail of the absorption spectrum.

In a later paper, Ghosh and Feng [6] developed a model which has some initial similarities with the model of De Vore [5]. It is based on the diffusion of photogenerated species, except that these were again taken to be excitons in merocynine, just as in tetracene and anthracene, rather than free electrons and holes, as in MgPh. It is also important to note that Ghosh and Feng model [6] was developed for a sandwich cell geometry. The same diffusion equation appears equation 1.38, though subject to slightly different boundary conditions. Namely, the exciton density falls to zero at the electrodes (n=0 at x=0). Solution of the diffusion equation subject to these boundary conditions yields, an expression for the exciton density, as given in equation 1.46,

$$n = \frac{\alpha\theta I_0}{\beta^2 - \alpha^2}\left[\left(\frac{e^{\beta l} - e^{-\alpha l}}{e^{-\beta l} - e^{\beta l}}\right)e^{-\beta x} - \left(\frac{e^{-\beta l} - e^{-\alpha l}}{e^{-\beta l} - e^{\beta l}}\right)e^{\beta x} + e^{-\alpha x}\right] \qquad (1.46)$$

where $\beta=1/\sqrt{(D\tau)}$. Further, the photocurrent is taken to be proportional to the gradient of the exciton density at the aluminum electrode. In the modified De Vore model, the photoconductivity in a surface cell geometry is evaluated by integrating the resistivity over the thickness of the film. For illumination through the aluminum electrode, the photocurrent is given by equation 1.47 resulting in a symbatic response

$$J_{Al} = -D\left(\frac{dn}{dx}\right)_{x=0},$$

$$J_{Al} = \frac{\alpha\theta I_0 D}{\left(\beta^2 - \alpha^2\right)} \times \left\{\frac{\beta\left[e^{\beta l} - e^{-\alpha l}\right] + \beta\left[e^{-\beta l} - e^{-\alpha l}\right] + \alpha\left[e^{-\beta l} - e^{\beta l}\right]}{\left[e^{-\beta l} - e^{\beta l}\right]}\right\} \qquad (1.47)$$

For illumination through the silver electrode, the photocurrent is given by equation 1.48-1.49. This results in an antibatic response for sufficiently thick film and is given by

$$J_{Ag} = -D\left(\frac{dn}{dx}\right)_{x=l}, \qquad (1.48)$$

$$J_{Ag} = \frac{\alpha\theta I_0 D}{\left(\beta^2 - \alpha^2\right)} \times \left\{\frac{2\beta - e^{-\alpha l}\left[\beta e^{-\beta l} + \beta e^{\beta l} - \alpha e^{-\beta l} + \alpha e^{\beta l}\right]}{\left[e^{-\beta l} - e^{\beta l}\right]}\right\} \qquad (1.49)$$

Recently systematic studies on the dependence of the dc and ac photocurrent of MEH-PPV photodiodes on the film thickness as well as applied voltage, have been presented by M.G. Harrison *et al* [2]. Generally the same feature as for PPV diodes were observed in the case of MEH-PPV.

Under the forward bias the photocurrent follows more the absorption spectrum (symbatic response) as under reverse bias (antibatic response). With increasing device thickness the symbatic and antibatic become more pronounced. Several theoretical models developed to relate the spectral photocurrent to the absorption were considered, i.e. the model of Ghosh *et al* [3] Tang and Albrecht [4], De Vore [5], Ghosh and Feng [6] and Desormeaux [7]. The first two models [3,4] only consider photoinduced charge carrier generation within a narrow region close to one of the electrode, while the other three models [5-7] solve the diffusion equation to specify boundary conditions. However, the simulated action spectra calculated by these models are all very similar and in addition, the simulation are in rather poor agreement with the experimental data and the symbatic and antibatic response of the devices could only be reproduced qualitatively.

References

1. R. H. Bube, Photoelectronic Properties of Semiconductors, Cambridge University Press, Cambridge 1992.
2. M.G. Harrison, J. Gruner, G. C. W. Spencer, Phys. Rev. **B. 55**, 7831 (1996).
3. A.K. Gosh *et al*, J. Appl. Phys. **45**, 230 (1974).
4. C. W. Tang, A.C. Albrecht, J. Chem. Phys. **62**, 2139 (1975).
5. H. B. DeVore, Phys. Rev. **B 102**, 86 (1966).
6. A. K. Ghosh, T. Feng, J . Appl. Phys. **49**, 5982 (1978).
7. A. Desormeasux, J. J. Max, R. M. Leblanc, J. Phys. Chem. **97**, 6670 (1993).
8. B. A. Gregg, M. A. Fox, and A. J. Bard, J. Phys. Chem. **94**, 1586 (1990)

Chapter

2

Photoconductivity: Nanoparticle TiO_2 and polymer blend structure

2.1 Introduction:

Hybrid organic-inorganic materials have emerged as a class of electronic and optoelectronic media for a number of potential technological applications. Nanocomposites consisting of inorganic quantum dots and functional polymers have shown promise for use in photorefractive applications, light emitting diodes and photovoltaic devices. The advantages offered by the nanocomposites are tunability of the electronic and optical properties of the quantum dots with the functional and structural flexibility of a polymer [1-6]. However, very little fundamental understanding of charge carrier transport in such hybrid materials exists.

It has been demonstrated that through this approach several advantages are realized. Perhaps the most attractive one concerns, the ease with which the spectral properties of the quantum dots are modified [7,8]. The tuning of the spectral properties of the nanocrystals is made possible by the fact that, the magnitude of the optical band gap depends on the size of the nanocrystal.

Over the last decade, soluble conjugated polymers have become attractive for use as inexpensive large area photodetectors and solar cells. Although polymer photoconductivity is severely limited by low charge carrier mobility, short exciton diffusion lengths, and low absorption [9,10], recent work has shown that the use of interpenetrating donor-acceptor network such as polymer/C_{60} nanoparticle composite

[11,12] and polymer/CdSe nanoparticle composites [13] and interpenetrating polymer networks [14] can substantially improve the photoconductivity and thus the quantum efficiency of polymer based photovoltaics. In these devices an exciton photogenerated in the active material, diffuses towards the donor/acceptor interface, and dissociates via charge transfer across the interface. The internal electric field set by the difference between the electrode energy levels, and the donor-acceptor morphology control the quantum efficiency of the cell. An alternative approach to efficient large area photovoltaic was introduced by O'Regan and Gratzel in 1990, using porous dye-sensitized TiO_2 nanocrystalline layers to form efficient electrochemical solar cells. In these devices, the high power efficiencies (10%) are attributed to the ultra-fast charge transfer from the dye to the TiO_2, high surface area of the TiO_2 film, the broad absorption of the dye and the efficient separation of opposite charge into different materials. Here the quantum efficiency and internal electric field are dependent up on the relative energy levels and bonding properties of the photoconducting dye and the porous TiO_2 nanoparticle surface[20].

A very generally cited limitation of polymeric material is their relatively slow response time. The photocurrent transients exhibits features typical of dispersive transport in an amorphous semiconductor. One of the limiting parameters is the free charge carrier mobility. Here the knowledge of the influence of nanoparticle doping on charge transport in the composites becomes important. The idea out here is that the presence of nanoparticles does not lead to increased trapping of holes. Conversely, a surprising result is observed: the mobility of the host polymer actually increases with the increase of nanoparticle concentration though it is well below the percolation limit.

More recently, TiO_2 nanoparticles blended with electroluminescence organics have shown to undergo lasing action with greatly reduced threshold pump powers. Our understanding of effects of nanoparticles on the performance of electro-optic polymer devices is far from complete. But, it has been generally thought that the enhanced properties are due to either the ability of a group of nanoparticles to act as charge carriers, as electrooptically active centers or as optical microcavities.

Device fabrication with composites of conjugated polymers and Buckminster fullerene C_{60} as the active layer with efficient photoinduced charge transfer, preventing the initial electron–hole recombination, was a significant advancement in the exploration of polymeric photodiodes and photovoltaic cells [15,16]. Studies of charge separation at the interface between organic molecules and nanocrystals, particularly systems of organic dyes adsorbed on TiO_2 nanocrystalline films, as a basis for efficient photovoltaic devices, have also generated considerable interest [17]. In a recent report, it was shown that in a nanocrystalline TiO_2|PPV composite, excitons photogenerated in the polymer could be dissociated at the interface between the components with the electrons transferred to the nanocrystals [18].

2.2 Our Approach:

Initially we carried out the following sequence of experiments: (i) Comparison of absorption of TiO_2, MEH-PPV and different concentrations of TiO_2-MEH-PPV (2, 5 and 10 % TiO_2 weight ratio). (ii) Morphology of the composite film through SEM (iii) Comparison of photoluminescence (PL) spectrum (iv) Photoconductivity (PC) studies. The optical absorption spectrum (Figure 2.1) of MEH-PPV/TiO_2 composite shows no significant feature of TiO_2 for 2% TiO_2 weight ratio and singnificant feature when TiO_2

concentration increases. Looking at the morphology of the films for 2, 5 and 10 % TiO_2 weight ratio; we found that 2% gives a film with no agglomeration and the film did not indicate any macro phase separation (Figure 2.2). Hence most of our studies focus on the 2% TiO_2:MEHPPV samples. Uniform films could be obtained by casting and spin-coating methods, with an average TiO_2 interparticle distance ~ 100 Å. From the PL studies of pristine MEH-PPV and 2% TiO_2 weight ratio, we found that spectrum is not changed along with insignificant quenching of PL for the present concentration of TiO_2 (Figure 2.3). PL is sensitive to the morphology and distribution of the nanocrystalline TiO_2. From the studies of photoconductivity, we get a well-resolved photocurrent spectral response as shown in Figure 2.1C, along with enhancement by one order of magnitude in the photoconductance measurement in the surface configured samples.

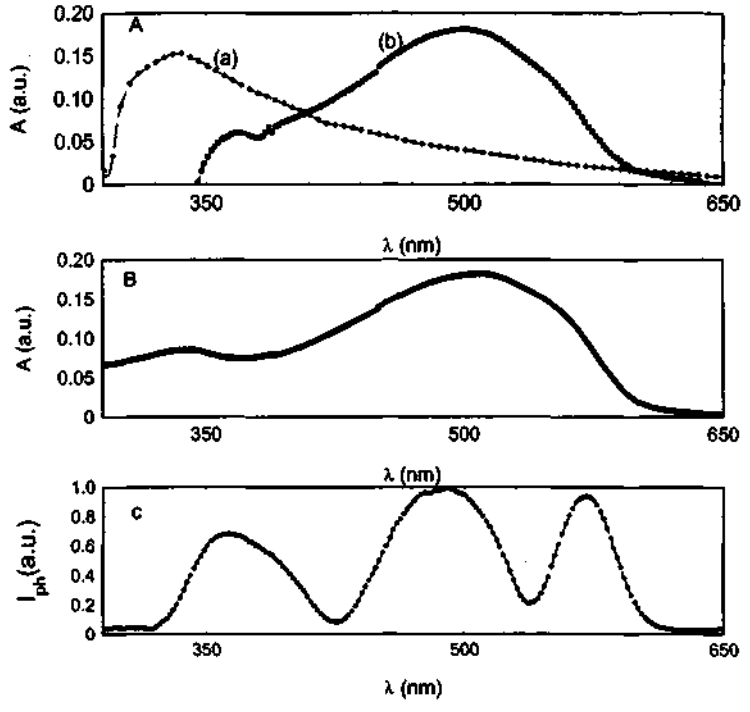

Figure 2.1: A: Absorption spectrum of thin films of (a) TiO_2 (b) MEH-PPV B: TiO_2-MEH-PPV and C: Photocurrent spectral response of ITO/TiO_2-MEH-PPV/Al with no external field applied with light illumination from ITO side.

The later has lead to confusion since (i) polymer/nanoparticle composites have not been shown to quenching of PL efficiency at lower concentration and (ii) high reasonable photovoltaic which require effective charge separation.

It has been reported [19] that PL efficiency of polymer is quenched by blending with TiO_2 particles. Giving the value of 1 to PL of pristine polymer, the PL in the composite is reduced to 0.065, 0.06 and 0.5, respectively, at 5, 20 and 50 % TiO_2 weight ratio. This suggests that electron transfer from polymer to TiO_2 is occurring and that the charge transfer is fast enough to compete with the radiative recombination of polymer exciton.

Figure 2.2: SEM picture of 2% wt. ratio of TiO_2 with respect to MEH-PPV.

In the present study, the insignificant quenching of PL in the polymer suggests that the isolation of individual nanoparticles within the polymer limits the occurrence of charge transfer. As shown in Figure 2.4(b), the alignment of energy levels at the

TiO_2/MEH-PPV interface is such that an electron in the polymer may lower its energy by charge transfer to a TiO_2 nanoparticle. Nanoparticle isolation within the polymer matrix, however, can prevent significant charge transfer because electron transfer from the MEH-PPV to the isolated nanoparticles would result in charge build up on a single site, impeding further charge transfer from the MEH-PPV [20]. Therefore, nonpercolating aggregation of the TiO_2 nanoparticles inhibits the formation of internal network of donor-acceptor heterojunctions, required for sustained charge transfer from the polymer to the TiO_2.

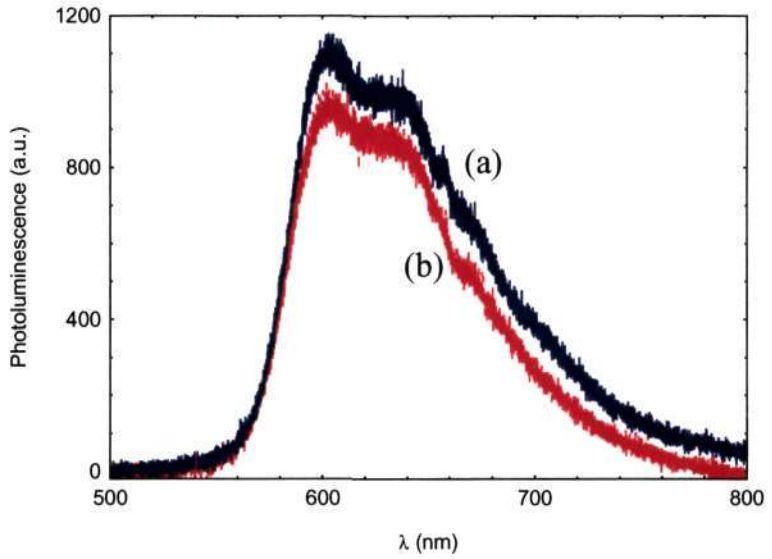

Figure 2.3: Photoluminescence of thin film of (a) pristine MEH-PPV (b) 2% weight ratio TiO_2 blended MEH-PPV.

The question then is, why do the nanoparticles so pronouncedly improve the efficiency of photocurrent generation even at this low concentration of TiO_2. Unlike TiO_2, excellent acceptor property of C_{60} is due to the structural relaxation of the fullerene following photoexcitation which is assumed to be forming long living charges. The electron transfer to C_{60} occurs faster than 1 ps thereby strongly quenching the PL as well as triplet exciton formation of the conjugated polymer. This implies that this process is

efficiently competing with the dipole-allowed radiative emission as well as other non-radiative channels. However, the successful and efficient charge separation is influenced by a number of limiting factors. Generally, the ionization potential of the excited state of the donor (I_D*), the electron affinity of the C_{60} (χ_{C60}) and the Coulomb attraction of the separated radicals (U_C) including the polarization effects should match the following inequality:

$$I_D - \chi_{c_{60}} - U_C < 0 \qquad (2.1)$$

Studies by Janssen *et al* [21] pointed out, that equation 2.1 is a necessary but not sufficient condition. Some other factors may inhibit the charge transfer, such as a potential barrier preventing the separation of the photoexcited electron–hole pair or the morphology of the blend preventing the overlap of the donor and acceptor excited state wave functions due to too large intermolecular spacings.

Ideal picture for a photo-induced charge transfer, TiO_2-MEH-PPV, is shown in Figure 2.6. Under photoexcitation, an exciton generated in the MEH-PPV layer transfer negative charge to the conduction band of the TiO_2 and transfer of positive charge to the low work function electrode. The negative charge must also continue to flow out of the TiO_2 to the high work function electrode. All of the above charge transfer process are energetically favorable.

In this section we investigate the effect of lightly dispersed TiO_2 nanocrystals in MEHPPV. TiO_2 even in dilute quantities acts as a charge separator, with the primary photogeneration and carrier transport essentially occurring in the polymer backbone. An

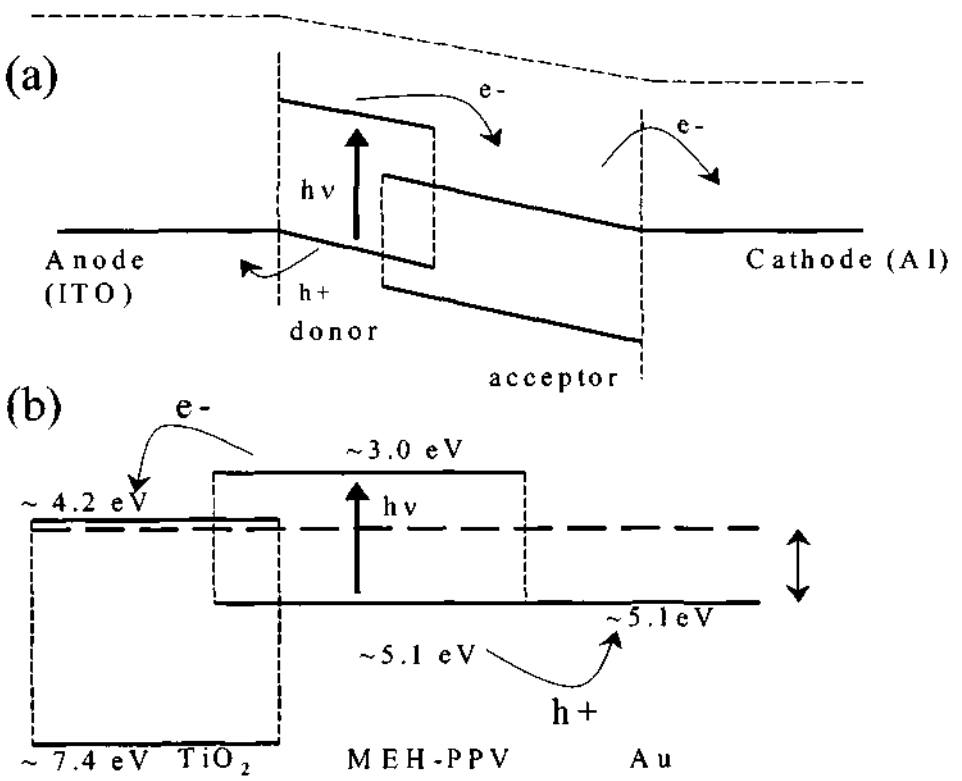

Figure 2.4: Energy diagrams depicting the transfer of charge for the (a) traditional donor-acceptor model and (b) the Grätzel-like model. In traditional donor-acceptor photocells, the open circuit voltage is mainly due to the difference in work functions between the anode (ITO) and the cathode (Au) because the polymer layer is insulating at low voltages. In Grätzel cells, the anode and the cathode serve only as quasi-ohmic contacts and the maximum open circuit voltage is determined by the difference between the Fermi level of the TiO_2 under illumination and the HOMO of the replenishing species [15,20].

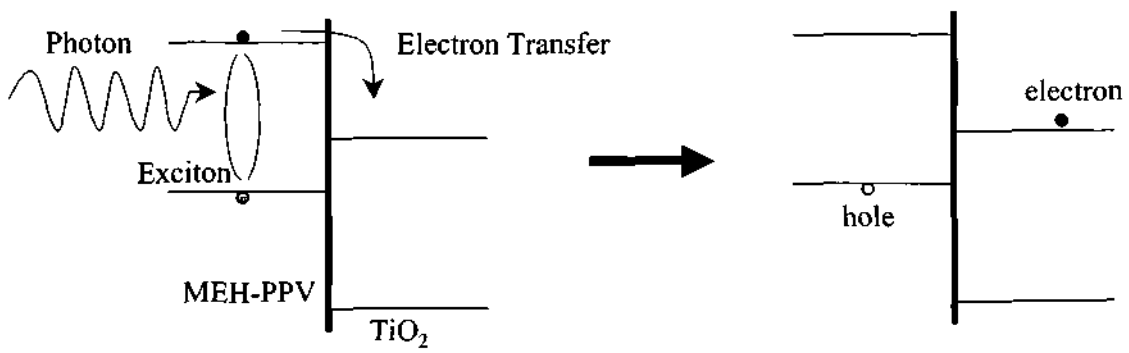

Figure 2.5: Charge transfer across the interface in *MEH-PPV/TiO_2* blends

important aspect which has not been addressed in these devices stems from the fact that photodiodes are typically used in the reverse bias for maximum sensitivity, and under these bias conditions the spectral range of interest should not pose a limitation. In pristine MEHPPV-based devices, the photocurrent spectral response $I_{ph}(\lambda)$ in the reverse bias peaks at the absorption edge (antibatic response) with practically no I_{ph} in the absorbing region. This has been explained qualitatively on the basis of exciton quenching at the Al interface and the low electron mobility of the polymer [23]. In the presence of electron acceptor moieties, such as TiO_2, the spectral range can be controlled by the magnitude of the bias voltage V. We also highlight important differences in the switching response in the forward bias and reverse bias and its implication in photodetector devices.

To achieve a highly efficient photodetector, one needs to have high efficient charge carrier generation and separation. We chose the present system based on the ideas of classical physics: (i) Large surface area (ii) Increased effective pathlength (iii) Electro-optic centers. It is important to have large area of interface between the two materials, in order to achieve high quantum efficiency of charge separation. It is also assumed that due to difference in dielectric constant of the nanoparticle and polymer, there has been increased in optical scattering. Another advantage is that photoexcited carriers can encounter increased effective path length in this composite system. Apart from this we have another quantum mechanical picture, which says that upon photoexcitaion, an exciton is created at the polymer and an electron the excited state will be transferred to high electron affinity nanoparticle TiO_2. In this process results in separation of an electron and hole separated which is necessary for photocurrent generation.

2.3 Materials:

We used NanoTek Titanium Dioxide of high purity (99.5+%) with Crystal Phase of 80% anatase / 20% rutile. Bulk Density is 0.20 g/cc with average particle size of 25 - 51 nm. The polymer used was MEH-PPV ~ Poly-2-Methoxy-5-(2′-ethyl-hexoxy) 1, 4 paraphenylenevinylene from Kodak Inc.

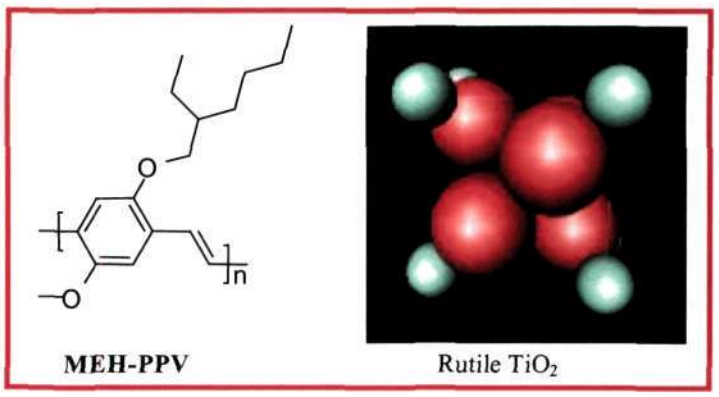

Figure 2.6: Chemical structure of MEH-PPV and crystal structure of Rutile TiO_2.

2.4 Experimental method:

TiO_2 nanocrystals with particle size ~ 36 nm were obtained from Nanophase Corporation. TiO_2 in weight ratios 2%, 5%, and 10% with respect to MEHPPV was dissolved in *p*-xylene along with MEHPPV to form clear solutions. The present studies focus on the 2% TiO_2:MEHPPV samples where electron microscopy observations did not indicate any phase separation. Uniform films could be obtained by casting and spin-coating methods, with an average TiO_2 interparticle distance ~ 100 Å. Typical devices were ~ 0.25 cm^2 in dimension with thickness of the blended layer being ~ 2730 Å. I_{ph} measurements, as shown in Figure 2.8, were carried out on sandwich devices of ITO|TiO_2:MEHPPV|Al with the light incident on the indium tin oxide ITO side, using

lock-in techniques and dc methods. Due to the observation of a sizable persistent photocurrent, as described later, dc current (I) measurements were measured under dark

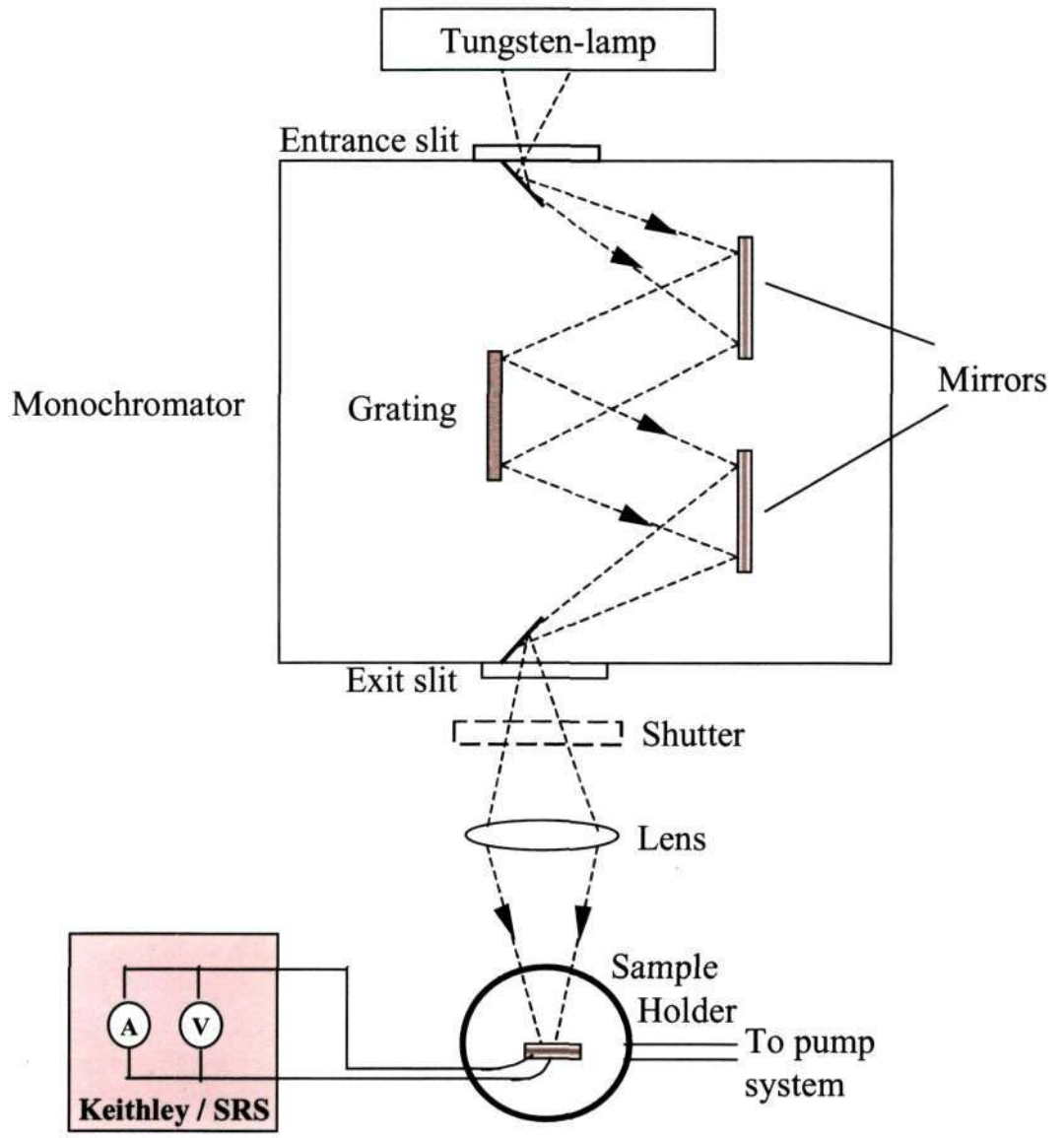

Figure2.7: Experimental set-up for measurement of photocurrent spectral response.

and light conditions, with sufficient elapse time until stable values were obtained. For the spectral response studies, the second-harmonic effects were eliminated and the data presented are the normalized $I_{ph}(\lambda)$.

2.5 Results and Discussion:

Measurements of the I_{ph} in the surface configuration were done with an interelectrode spacing of 0.5 mm. These uniform illumination measurements indicate the high charge separation efficiency in the 2% TiO_2 blended polymer compared to that in the pristine polymer by an order of magnitude with the following values of photoconductance; 10^{-14} S for pristine MEHPPV, which is in agreement with earlier reported results [24], and 10^{-13} S for the 2% TiO_2:MEHPPV sample, with identical photon flux and voltage bias of 9 V.

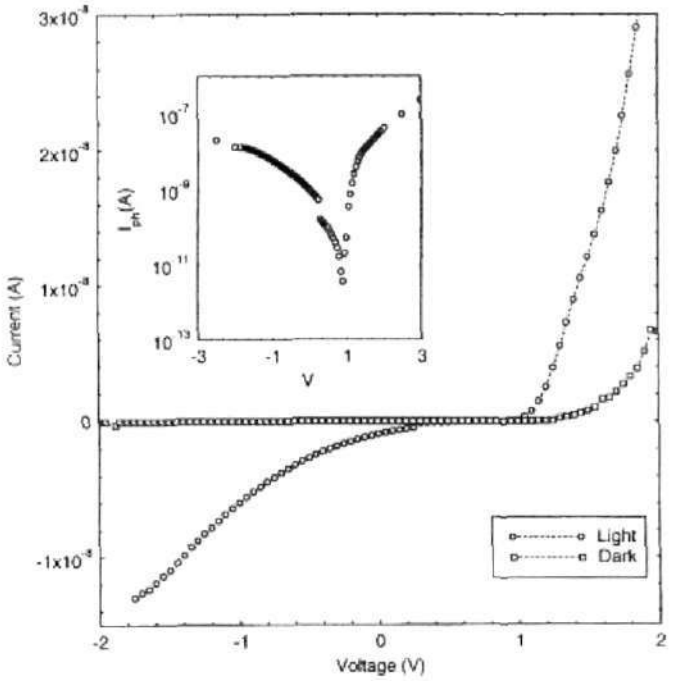

Figure 2.8: dc current vs voltage in dark and white light (20 $\mu W/cm^2$) of the ITO|2% TiO_2:MEHPPV|Al device. Inset is the current under illumination in the log scale vs voltage.

The I–V response of the ITO|TiO_2:MEHPPV|Al device in the dark shown in Figure 2.8 is similar to that of polymer-based devices with large rectification ratios[23,24]. Figure 2.8 also shows the I–V response of the device under white light and highlights the large photoresponse in this system. The I_{ph}/I_{dark} ratio in the reverse bias is as high as 10^4 at – 4.5 V with responsivity of ~ 50 mA/W at – 9 V and I_{dark} = 10 nA. The open-circuit voltage, as shown in the inset, is in the range of ~ 0.8 V with a short-circuit current density of ~ 5 nA/cm^2 at photon density of 10 W/cm^2. The intensity dependence of I_{ph} for input power 0.1 μW/cm^2–1 mW/cm^2 is linear in the entire voltage range.

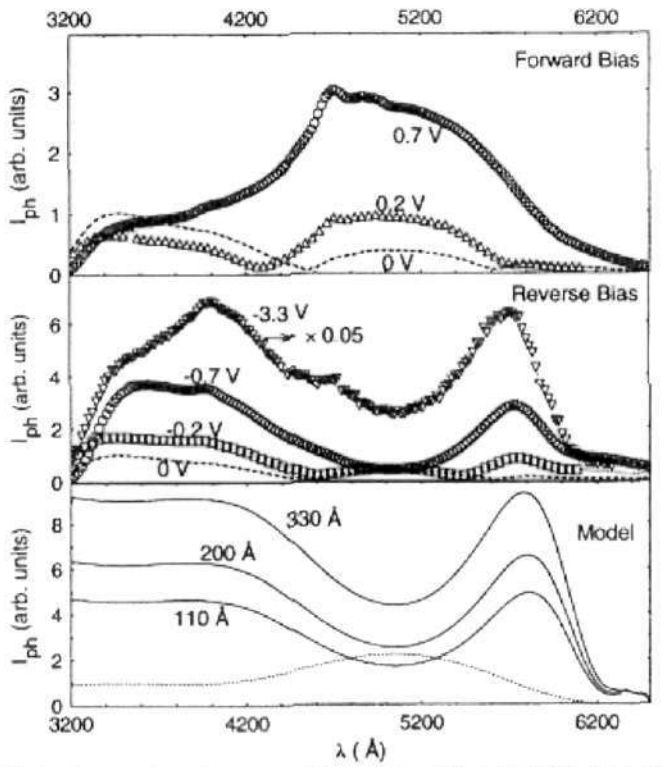

Figure 2.9: $I_{ph}(\lambda)$ in forward and reverse bias of the ITO|2% TiO_2:MEHPPV|Al device along with the model of Ghosh *et al.* [31]. Note that the response for V = – 3.3 V is reduced by a factor of 20 for comparison purpose. l = 2500 Å and l_b = 200 Å along with different 1/β values as indicated were used for the model, the dashed line in the model is the symbatic response.

The forward bias spectrum, with the illuminated ITO side biased positive (V = 0.7 V) in Figure 2.9 has the onset at the absorption edge. This corresponds to that of

MEHPPV and increases gradually with increasing photon energy indicating a symbatic response. The response for bias voltage for the values in the region $-0.3 < V < 0.3$ V, consists of both symbatic and antibatic features, and can be subdivided into three spectral regions. Region 1 is at the absorption onset with a sharp maxima at 5735 Å, followed by the symbatic feature in the region 4600Å $< \lambda <$ 5600 Å, and then a third distinct region for $\lambda <$ 4500 Å. At larger reverse bias voltage $V = -3.3$ V, as shown in Figure 2.9, regions 1 and 3 overlap and for $V > -4.5$ V, $I_{ph}(\lambda)$ is almost uniform thereby offering a wide spectral coverage for detection (3100–6300 Å). I_{ph} vs V measurements at different λ were consistent with the spectral response observations.

Differences in the $I_{ph}(\lambda)$ in the forward and reverse bias has been reported for MEHPPV [23,27]. The results were for samples which were 7000 Å thick with a peak for $I_{ph}(\lambda)$ at the absorption edge. They were explained on the basis of exciton quenching at the cathode, and the absence of photocurrent at higher photon energies due to the reabsorption by the relatively thick polymer film [23]. Thinner samples indicated the presence of $I_{ph}(\lambda)$ at higher photon energy [23]. In the present case of TiO_2-dispersed samples, the spectral features are more sensitive to the magnitude of the reverse bias. TiO_2 nanocrystals, which have large surface area, play the role of electron acceptors since the interparticle distances are in the same order of magnitude as the singlet exciton/carrier diffusion length (5–15 nm) observed in MEHPPV[28,29,32]. At higher absorption, $\lambda <$ 3400 Å, where electron–hole pairs are generated in TiO_2 nanocrystallites, there may be a process of hole transfer onto the polymer from TiO_2.

Results on MEHPPV devices have indicated that I_{ph} in the reverse bias depends on ambient conditions. It has been explained on the basis of the extrinsic process for charge

generation, enhancing dissociation of the excitons [23,30]. However, for the TiO_2-dispersed polymer devices, I_{ph} is relatively stable with respect to ambient conditions with spectral responses similar to that in vacuum conditions. This is indicative of energetically preferential TiO_2 sites for charge-carrier separation. The interpretation of the $I_{ph}(\lambda)$ maxima at the band edge on the basis of the recombination of the high density of carriers or excitons within a narrow region close to the electrode is unlikely due to the appearance of the feature at extremely low photon flux. Additionally, possible factor apart from TiO_2-mediated exciton quenching at the cathode interface, which can lead to the bias-dependent spectral responses, can arise from a gradient in a distribution along the thickness of the film. This can then provide asymmetry in the charge-carrier distribution. Similar responses are expected with the light incident on partially transparent negative-biased metal electrodes as observed for MEHPPV [23]. The length scales of the device which may decide the spectral width of the different regions are the thickness of the polymer layer l, $1/(\alpha)$ where α is the absorption coefficient, exciton/free-carrier diffusion length $1/\beta$, and the barrier width l_b.

The bias dependency of $I_{ph}(\lambda)$ can be qualitatively understood in terms of the model by Ghosh *et al* [31]. I_{ph} here depends on the ability of the minority carriers (electrons) generated in the bulk to reach the interface. This is characterized essentially in terms of $1/\beta$ and l_b. This argument is applicable to excitons too which diffuse and undergo dissociation. The barrier in the present case is primarily at the metal–polymer interface and is ~ 100–200 Å wide [23]. For illumination from the ITO side which is opposite the barrier, the expression for I_{ph} results in an antibatic response [26] :

$$I_{ph} = \int_0^{l_b} \theta\, I_0 \alpha \exp(-\alpha x) \quad \text{(barrier)}$$
$$+ \int_{l_b}^{l} \theta\, I_0 \alpha \exp(-\alpha x)\exp[-\beta(x - l_b)]dx \qquad \text{(bulk)} \tag{2.2}$$

Figure 2.10 also shows the numerical estimates of $I_{ph}(\lambda)$ for different $1/\beta$ values. $I_{ph}(\alpha)$ predicted from the model are remarkably similar to the experimental results. It is noted that the model yields better fits to the experimental results if β is a stronger function of V compared to the barrier width dependency on V.

The I_{ph} switching responses of ITO|TiO_2:MEHPPV|Al devices were done with different modulation of the incident light. The high photocurrent signals from the devices could be directly observed on a HP 54520 oscilloscope, CRO, without any preamplification. In fact, photoinduced undistorted signals as large as $V_{p-p} \sim 500$ mV could be observed at – 9 V bias and incident power of 100 μW/cm^2, 1 MΩ scope input. Figure 2.10(a) shows the I_{ph} signals as measured by the CRO in the single-shot mode and triggered by a pulse from a function generator HP 8116 A driving a standard green light - emitting diode (LED) source with an out put of 10 μW/cm^2. The device in the reverse bias responds to the 50 μs wide pulse with a rise time < 100 ns and a decay time of < 10 μ s. The response duration can be attributed to a variety of sources including the LED switching response and the junction capacitance. The forward bias response to the LED pulse, in contrast, is much slower with the presence of the current of magnitude persisting for several milliseconds after switching off. It is to be noted that these results are not true for transient photoconductivity measurements probing the initial buildup and initial decay which is on the scale of less than 100 ps [24,30]. The non-single- exponential,

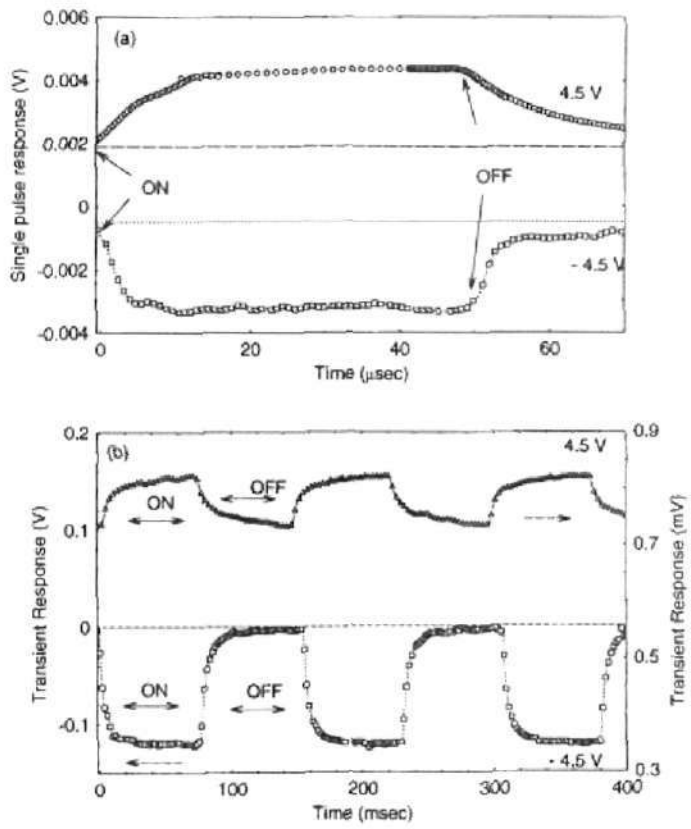

Figure 2.10: Oscilloscope response, 1 MΩ input, of the ITO|2% TiO_2:MEHPPV|Al device in forward and reverse bias to: (a) pulsed green LED, 10 μW/cm^2, the dashed lines indicate the dark dc values in the different bias. (b) 13 Hz chopped, 532 nm, 100 μW/cm^2 diode laser source, note that the *Y* scale for the forward bias is on the right-hand side.

which have long-lifetime responses may be accounted for by considering that charge-carrier recombination is restricted by a dispersive diffusion mechanism [29]. This effect of forward bias is magnified at higher intensities. This is shown in Figure 2.10(b), on the right *Y*-axis, as observed by the signal profile on the CRO in response to a regularly chopped (13 Hz) incident laser, λ= 532 nm, incident power ~ 100 W/cm^2. In the forward

bias, Figure 2.9(a), the dc value ~ 0.12 V of the response profile of the polymer device response with the light on is much greater than the dark $V_{dc} \sim 0$. The persistent photocurrent which lasts longer than the chopper period $_{chopper}$, adds up after each exposure of the chopped light pulse. This increases the dc value of the output pulse with a corresponding decrease in $I_{peak-peak}$ value over a period (several seconds) and can be observed in real time on the scope. The reverse bias response, as shown in Figure 2.10 (b), in this chopping frequency range does not show such cumulative effects since $\tau_{rev} > \tau_{chopper}$, where τ_{rev} is the duration of the persisting photocurrent in the reverse bias. The results indicate the usefulness of these devices in the reverse bias directly, without any modifications for applications with bandwidth specifications < 10 kHz

It is to be noted that photocurrent depends on nanoparticle size which leads to the following issues like (i) high surface/volume ratio, (ii) Higher rate of agglomeration, (iii) Amplified light/scattered light. We also studies blend system of poly, 3-octylthiophene P3OT-TiO_2. Photocurrent generation efficiency increases by an order of magnitude. We also studied the photocurrent by varying the thickness of the polymer layer. We found that the threshold thickness for polymer film thickness for achieving highest photocurrent is approximately 70 nm.

2.6 Conclusion:

TiO_2–MEHPPV systems exhibit stable and efficient photodiode properties. $I_{ph}/I_{dark} \approx 10^4$ at *–3 V*. In the presence of *TiO_2*, the spectral range can be controlled by the magnitude of the bias voltage *V*. Spectral response is governed by *l*, $1/\alpha(\lambda)$, $1/\beta$, and barrier width l_b. The switching response in the forward and reverse bias are different.

References

1. Y. Wang and N. Herron, J. Lumin. **70**, 48 (1996).
2. K. Rajeshwar, N. R. de Tacconi, and C. R. Chenthamarakshan, Chem. Mater. **13**, 765 (2001).
3. Y. Wang and N. Herron, Chem. Phys. Lett. **200**, 71 (1992).
4. Y. Wang, Pure Appl. Chem. **68**, 1475 (1996).
5. N. Herron and D. L. Thorn, 3.0.CO; 2-6"Adv. Mater. **10**, 1173 (1998).
6. M. Lal, M. Joshi, D. N. Kumar, C. S. Friend, J. Winiarz, T. Asefa, K. Kim, and P. N. Prasad, Mater. Res. Soc. Symp. Proc. **519**, 217 (1998).
7. S. H. Wang, S. H. Yang, C. L. Yang, Z. Q. Li, J. N. Wang, and W. K. Ge, J. Phys. Chem. B **104**, 11853 (2000).
8. J. Nanda, K. S. Narayan, B. A. Kuruvilla, G. L. Murthy, and D. D. Sarma, Appl. Phys. Lett. **72**, 1335 (1998).
9. S. Barth, H. Bässler, H. Rost, and H. H. Hörhold, Phys. Rev. **B 56**, 3844 (1997).
10. D. Moses, J. Wang, G. Yu, and A. J. Heeger, Phys. Rev. Lett. **80**, 2685 (1998).
11. G. Yu, J. Gao, J. C. Hummelen, F. Wudl, and A. J. Heeger, Science **270**, 1789 (1995); G.Yu and A. J. Heeger, J. Appl. Phys. **78**, 4510 (1995).
12. C. J. Brabec, V. Dyakonov, N. S. Sariciftci, W. Graupner, G. Leising, and J. C. Hummelen, J. Chem. Phys. **109**, 1185 (1998).
13. N. C. Greenham, X. Peng, and A. P. Alivisatos, Phys. Rev. **B 54**, 17628 (1996).
14. J. J. M. Halls, C. A. Walsh, N. C. Greenham, E. A. Marseglia, R. H. Friend, S. C. Moratti, and A. B. Holmes, Nature (London) **376**, 498 (1995).
15. B. O'Regan and M. Grätzel, Nature (London) **353**, 737 (1991).

16. F. Cao, G. Oskam, and P. Searson, J. Phys. Chem. **99**, 17071 (1995).

17. G. Yu, J. Wang, J. McElvain, and A. J. Heeger, Adv. Mater. **10**, 1431 (1998).

18. N. S. Sariciftci, L. Smilowitz, A. J. Heeger, and F. Wudl, Science **258**, 1474 (1992).

19. S. Luzzati, M. Basso, M. Catellani, D. Gebeyehu, N.S. Sariciftci, C.J. Brabec, Thin Solid Films **52-56,** 403 (2002).

20. A.C. Arango, S.A. Carter, P.J.Brock, Apll. Phys. Lett. **74**, 1698 (1999).

21. R. A. Janssen, N. S. Sariciftci, and A. J. Heeger, J. Chem. Phys. **109**, 1185 (1998).

22. G. Yu, J. Gao, J. C. Hummelen, F. Wudl, and A. J. Heeger, Science **270**, 1789 (1995)

23. M. G. Harrison, J. Gruner, and G. C. W. Spencer, Phys. Rev. **B 55**, 7831 (1997).

24. C. H. Lee, G. Yu, D. Moses, K. Pakbaz, C. Zhang, N. S. Sariciftci, A. J. Heeger, and F. Wudl, Phys. Rev. **B 48**, 15425 (1993).

25. D. Braun and A. J. Heeger, Appl. Phys. Lett. **58**, 1982 (1991).

26. H. Antoniadis, B. R. Hsieh, M. A. Abkowitz, S. A. Jenekhe, and M. Stolka, Synth. Met. **62**, 265 (1994).

27. R. N. Marks, J. J. M. Halls, D. D. C. Bradely, R. H. Friend, and A. B. Holmes, J. Phys.: Condens. Matter **6**, 1379 (1994).

28. J. J. M. Halls, K. Pichler, R. H. Friend, S. C. Moratti, and A. B. Holmes, Appl. Phys. Lett. **68**, 3120 (1996).

29. B. Dulieu, J. Wery, S. Lefrant, and J. Bullot, Phys. Rev. **B 57**, 9118 (1998).

30. C. H. Lee, G. Yu, N. S. Sariciftci, A. J. Heeger, and C. Zhang, Synth. Met. **75**, 127 (1995).

31. A. K. Ghosh, D. L. Morel, T. Feng, R. F. Shaw, and C. A. Rowe, J. Appl. Phys. **45**, 230 (1974).

32. J. S. Salafsky, Phys. Rev. B. **59**, 10889 (1999).

Chapter

3

Geometry induced photocurrent studies of semiconducting polymer

3.1 Introduction:

Fundamental optical processes have known to be modified in a characteristic way within a resonant cavity, resulting in various phenomena e.g., inhibition or enhancement of spontaneous emission [1,2], thresholdless laser action [3,4], strongly directed emission [5], and spectral narrowing [6,7] of otherwise broad molecular flouresence.

To enhance the quantum efficiency of photogeneration, several techniques including multiple passes [8], highly folded interfaces [9] interpenetrating polymer network [10,11,12] and light trapping [13] have been introduced. All these reports emphasize on increasing efficiency with the light which $\lambda < hc_o/E_g$. The problem here is that these are very slow photodetectors because of reasonably thick polymer film.

We explore a set of interesting features in a Schottky-type polymer photodiode which is confined in a one-dimensional microcavity. The concept of "resonance cavity enhanced" (RCE) photodiodes for inorganic devices demonstrated by Chin and Chang [14], Ünlü and co-worker [15,16], Murtaza *et al.*[17], Tzeng, Li, and Ho [18] has been adapted here for polymer-based structures. The procedure entails the introduction of a thin (about 500 Å) polymer active layer in the microcavity, which is essentially a resonator with an effective cavity length of half the wavelength of light. The essential theme here is that the gain is not compromised while decreasing the photogenerated

charge carrier transit time across the thin polymer layer. We demonstrate the tunability of these polymer photodiodes to detect light of wavelength $\lambda > hc/E_g$, approaching the near-infrared region.

Our present approach to increase efficiency is much more than an improved light collection due to reflecting electrodes. We use an optical cavity length $L \cong \lambda/2n$, where n is the refractive index of the medium involved. A prior knowledge of the optical field distribution enables us to tailor the device by positioning the thin active medium at the antinode of the cavity. The internal quantum efficiency of the I_{ph} generation is dependent on the light-intensity distribution within the device. We compute the spatially varying optical-field pattern inside the resonant cavity using basic optical constants of the constituent layers to design the device. The computation involves solving the electromagnetic wave equation on a real-space mesh with a higher-order finite-difference formula for the Laplacian and establishes the link between the response and resonant or stationary states of the cavity. This strategy results in high gain and fast photodetection in a predetermined spectral region. In the process, we overcome the limitation on the detection region posed by the E_g of the polymers. The low but finite optical absorption coefficient is amplified in the cavity, resulting in a sizable photoresponse. The magnitude of α, as measured by photothermal deflection studies of polythiophenes, is in the range of 10–100 cm^{-1}, for the low-energy tail of the principle absorption edge, [19] compared to the maximum of 10^5 cm^{-1}. It has been attributed to excitations typical of low-dimension conjugated systems, and disorder effects arising from variation in conjugation length, [20] orientation, and phonon broadening processes. The I_{ph} caused by subgap absorption is generally discussed in terms of photoexciting the carrier to localized band-gap states,

which subsequently requires an optical or a thermal process to a delocalized state. There are other mechanisms assisted by interfacial bad-gap states [21] and charge transfer across the electrodes, which can also give rise to free-carrier generation. Processes like internal photoemission of electrons in the metal to an energy above the Schottky barrier [22] have also been the source of the I_{ph} below the absorption edge. The RCE geometry enables us to speculate on the possible I_{ph} mechanisms at the subgap regime using temperature-dependent studies. In the present case, the subgap photocurrent probably arises from the interfacial gap states prevalent in metal/thin-polymer/metal junctions.

In resonance cavity photodiode, the most important photodiode design consideration is its absorption coefficient α. If α is too small, a thick absorption layer is required, degrading the high-speed properties of the device by increasing the carrier transit time. On the other hand, large values of α require very thin absorber to keep the total cavity loss low. However, this emphasizes the complications associated with the effect of the standing wave. It is to be noted that for a resonance cavity photodiode, efficiency is not a strong function of α, and this higher value of α does not linearly increase at its maximum attainable efficiency. To obtain the maximum value of efficiency for a given value of α, however, other cavity parameters have to be optimized accordingly. Transit time is time taken by a charge carrier to diffuse through the active medium to an electrode, which is given by equation 1.30, where, d is the thickness of the absorbing medium, V_s is the average carrier saturation velocity. The photocurrent gain is given by equation 1.29.

When we reduce the $\tau_{transit}$, we are achieving a larger gain. But this poses a problem. While reducing the $\tau_{transit}$, thickness of the absorbing medium has to be

minimum which results in reducing the absorption. One can overcome this problem by having a resonant cavity enhancement of light absorption, with even thin absorbing medium. We have a cavity formed by two mirrors.

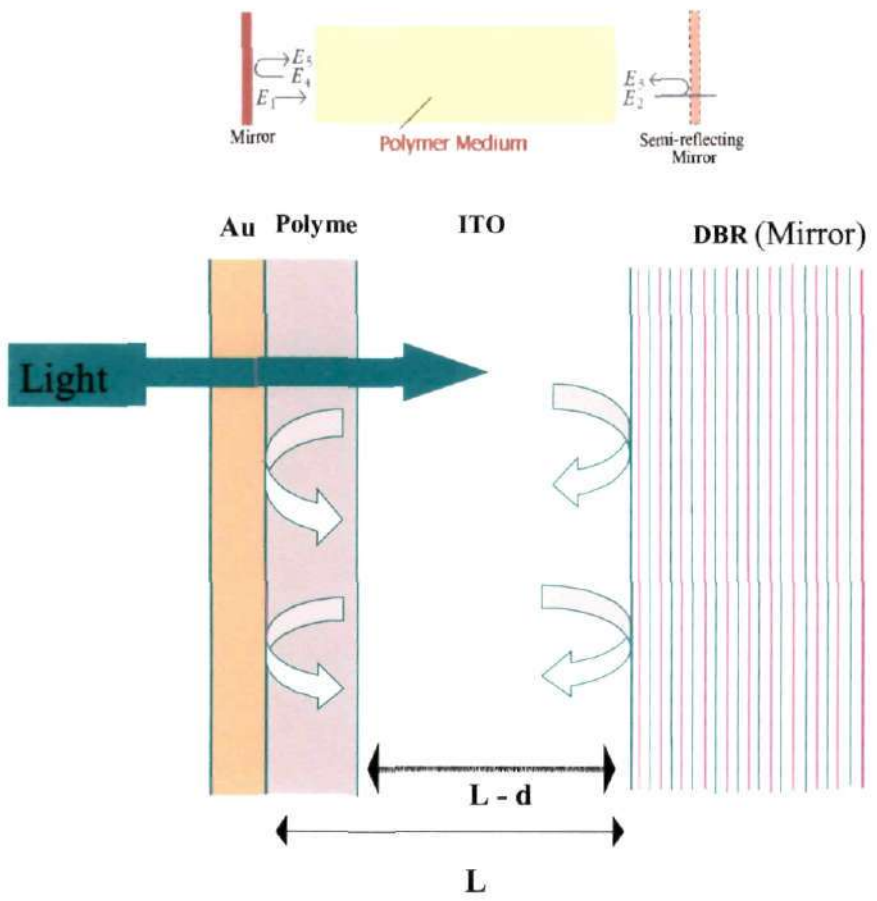

Figure 3.1: Top: Schematic of a resonant cavity. Bottom: Device structure of the resonance micro-cavity Photodiode.

We used two methods to find out the spatial dependence of optical electric filed inside the micro-cavity which is formed by various layers of different dielectric constants.

3.2 Real-Space method:

A novel method for simulating optical response of a resonant cavity using basic optical constants of its constituents is presented here. The method involves solving the electromagnetic wave equation on a real-space mesh with a higher order finite difference formula for the laplacian. The method provides a link between the response and resonant or stationary states of the cavity.

First, we summarize the methods described by Ünlü *et al* [16]. In the analytical treatment they use, reflections at the interfaces between the active layer and other material inside the cavity is neglected. They use reflection coefficients and phase changes at the reflectors and then sum up the reflections taking into account the optical constants of the materials inside the cavity. The spatial variation in the optical field inside the cavity is thus neglected. The latter gives rise to a "standing wave effect", which is an important issue for cavities with relatively thin active layers. They include this effect in the calculation by defining an effective absorption coefficient for the active layer. They also present an exact numerical simulation based on the transmission line model. In this, frequency-dependent impedence of every interface and layer in the cavity is considered.

We use a novel method, which borrows its concepts from the recent real-space methods in the electronic structure theory, but solves the electromagnetic wave equation. In the present context, for simplicity, we restrict ourselves to normal incidence of radiation on the cavity. The cavity is assumed to have a wide cross-section, thus the spatial variation of fields in the planes parallel to mirrors is not important. Along the direction of the propagation (axis of the cavity), we describe the optical field on a fine

mesh in real space $E(x_i)$, where $x_i=(i\text{-}1)\Delta x$ is a point on the mesh with spacing of Δx. The time dependence of the field is assumed to be:

$$E(x,t) = E(x)e^{i\omega t}$$

ω being the angular frequency of light. From the wave equation, it is clear that the time independent field $E(x)$ satisfies a simple equation:

$$\frac{d^2E}{dx^2} + \frac{\varpi^2}{c^2}\varepsilon(x)E = 0 \qquad (3.1)$$

Where, c is the speed of light in vacuum and ε is complex dielectric constant whose spatial dependence arises from the layers of different materials inside the cavity. In Figure 3.2, we show the mesh used in a typical simulation and the dielectric constant obtained by smoothening the interfacial region over a length-scale much smaller than the wave-length, but larger than the mesh spacing.

The laplacian in equation 3.1, is then made discrete on the mesh using a higher order (say, 6) finite-difference formula from Chelikowsky et al [23]. This converts the laplacian operator into a symmetric matrix L_{ij}.

$$\frac{d^2E}{dx^2} \Rightarrow \sum_j L_{ij}E(x_j)$$

The boundary conditions for the differential equation have to be imposed correctly for the evaluation of laplacian near the ends of the cavity (x_0 and x_N). In the present problem we

assume that the incident optical field has an amplitude 1 at x_i=0 and the reflected field has to be determined self-consistently. The boundary conditions we use are:

(1) The transverse electric fields are continuous at the end of the interface, and

(2) The derivative *dE/dx*, which is proportional to the transverse magnetic field, is also continuous.

The equation 3.1, along with the boundary conditions becomes (upon discretization) a matrix equation:

$$\sum_j M_{ij} E(x_j) = b_i \tag{3.2}$$

where, M is a sum of the sparse matrix L' and a diagonal matrix ε:

$$M_{ij} = L'_{ij} + \varepsilon(x_i)\delta_{ij}$$

The matrix L' is the Laplacian matrix obtained by incorporating boundary conditions and the presence of the reflected and transmitted optical field outside the cavity.

$$L'_{ij} = L_{ij} + \delta_{j,1}\delta_{i<o+1}\sum_{l=i}^{o} L_{1,l+1}\exp[ik(l+1-i)\Delta x] +$$

$$\delta_{j,N}\delta_{i<o+1}\sum_{l=i}^{o} L_{1,l+1}\left[E_+\exp\{k_g(l+1-i)\Delta x\} + E_-\exp\{-K_g(l+1-i)\Delta x\}\right]$$

L_{ij} is a real symmetric sparse matrix that represents finite-difference laplacian and its order to determines the sparsity. E_- and E_+ are incoming and outgoing field coefficients for the Bragg reflector. Symbols k and k_g are wave vectors in air and the first layer of Bragg reflector respectively. Vector b is proportional to the amplitude of the incident field and describes how it couples with the field inside the cavity.

$$b_{i,(i<o+1)} = -E_{inc}\sum_{l=i}^{o} L_{1,l}\left[\exp\{ik(l+1-i)\Delta x\} - \exp\{-ik(l+1-i)\Delta x\}\right]$$

The equation is then readily solved to get the optical-field profile inside the cavity:

$$E(x_i) = \sum_j M_{ij}^{-1}\vec{b}_j \qquad (3.3)$$

With the knowledge of the field profile, the optical response of the cavity is completely determined.

Physical interpretation of equation 3.3 is very rewarding, as it provides a link between the optical response and the resonance states of the cavity. Let m_i and $|i>$ be the eigen values and eigen vectors of the matrix M. Then it can be readily shown:

$$E = \sum_i \frac{1}{m_i}|i\rangle\langle i|b\rangle$$

Eigen states $|i>$ are the stationary (resonance) states of the cavity with appropriate boundary conditions. The eigen values are however shifted by the square of the wave vector of the incident radiation. The smallest eigen value (stationary state with frequency closest to that of the incident field) corresponds to the harmonic, which contributes the most to the optical response when the incident field does not exactly match the frequencies of the cavity.

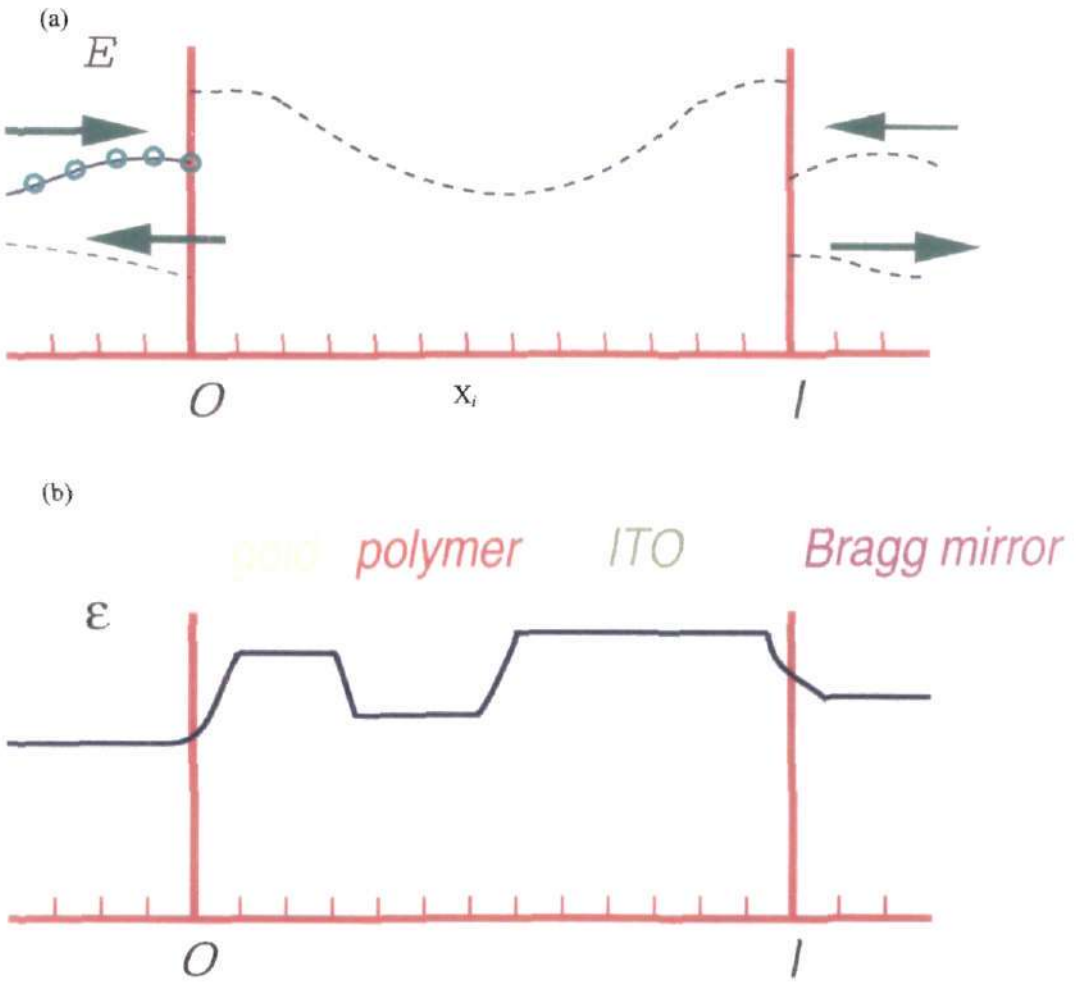

Figure 3.2: Schematic of (a) the mesh used to represent fields inside the cavity and (b) smoothened dielectric constants of materials inside cavity. The points outside are shown to indicate the knowledge of field there is used in imposing the boundary conditions, namely in evaluation of finite difference Laplacian.

3.3 Standing wave effect method:

A simplistic approach for modeling the standing wave effect in the cavity is done on the basis of summing up the forward E_f and backward component E_b of the electric field E, in terms of E_f at $z = 0$ and E_b at $z = L$. For a polymer of thickness d, total cavity

length L, top and bottom mirror layer reflectivity r_1 and r_2, and phase change of ψ_1 and ψ_2 at the top and bottom mirror, λ - wavelength, n - refractive index, and $\beta = 2\pi n/\lambda$

$$E_f(0) = tE_i + r_1 r_2 e^{-\alpha d - \alpha_{ex} L} e^{-i(2\beta L + \psi_1 + \psi_2)} E_f \qquad (3.4)$$

$$E_b = r_2 e^{-\alpha d/2} e^{-(\alpha_{ex}/2)L} e^{-i(\beta L + \psi_2)} E_f \qquad (3.5)$$

the net field $E(z)$ is then

$$E = E_f(0)\exp(-j\beta z) + E_b(L)\exp(j\beta(z-l)) \qquad (3.6)$$

and

$$|E|^2 = |E_f(0)|^2 + |E_b(L)|^2 + 2.\mathrm{Re}\{E_f^*(z).E_b(z)\} \qquad (3.7)$$

and upon simplification as in Ref. [16]

$$|E|^2 = \left\{\frac{|1 - r_1^2|}{|1 - r_1 r_2 e^{i(2\beta L + \psi_1 + \psi_2)}|^2}\right\} \times$$
$$\left[1 + r_2^2 + 2r_2\cos[2\beta(L-z) + \psi_2]\right]|E_i|^2 \qquad (3.8)$$

We further simplify the model by making the following assumptions: (i) Absorption of light occurs only within the active polymer layer in the cavity (ii) The phase change upon reflection at the DBR layer depends on its reflectivity (iii) The phase change at the gold electrode layer is ~ 0.25 rd, r_1= 0.7, n_{ITO}= 1.8, $n_{polymer}$= 1.9, α = 500 cm^{-1}. This data are as according to [24]. As indicated in Figure 3.1, the optical field pattern in the cavity based on Equation 3.8 is shown in Figure 3.3. The enhancement factor of the intensity, I in the

region in the vicinity of the gold mirror for the chosen cavity parameters justifies the placement of the active polymer layer in that region.

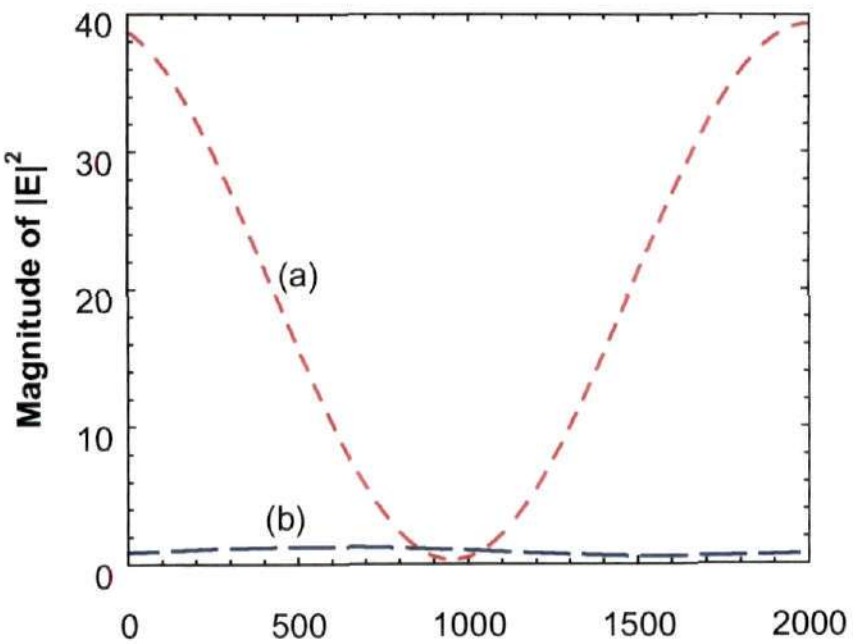

Figure 3.3: Spatial electric field for (a) DBR with r_2 =0.99 (b) DBR with r_2=0.2

3.4 Distributed Bragg Reflectors (DBR):

It is well known that a film of thickness $\lambda/4n_f$ where λ is the free space wavelength and n_f is the film refractive index (which lies between the refractive indices of the two surrounding media) acts like an antireflection layer. This happens due to the destructive interference occurring between the wave reflected from the top and bottom interface. The converse is also true that is the refractive index of the film was smaller (or greater) than both the surrounding media, then in such a case, in addition to the phase difference due to the additional path traveled by the wave reflected from the lower interface, there would be an extra phase difference of π between the two reflected waves.

Thus, in such a case a film of thickness $\lambda/4n_f$ would also increase the reflectivity rather than reduce it. In such a condition a reflectivity as high as 99.99% at desired wavelength is achievable.

If we consider a medium consisting of alternative layers of high and low refractive indices of $n_0+\Delta n$ and $n_0-\Delta n$ of equal thickness d as shown in the Figure 3.4. Such a medium is called a periodic medium and the spatial period of refractive index variation is given by $\Lambda = 2d$ and

$$n_0 = \frac{n_1 + n_2}{2}$$

$$\Delta n = n_1 - n_2$$

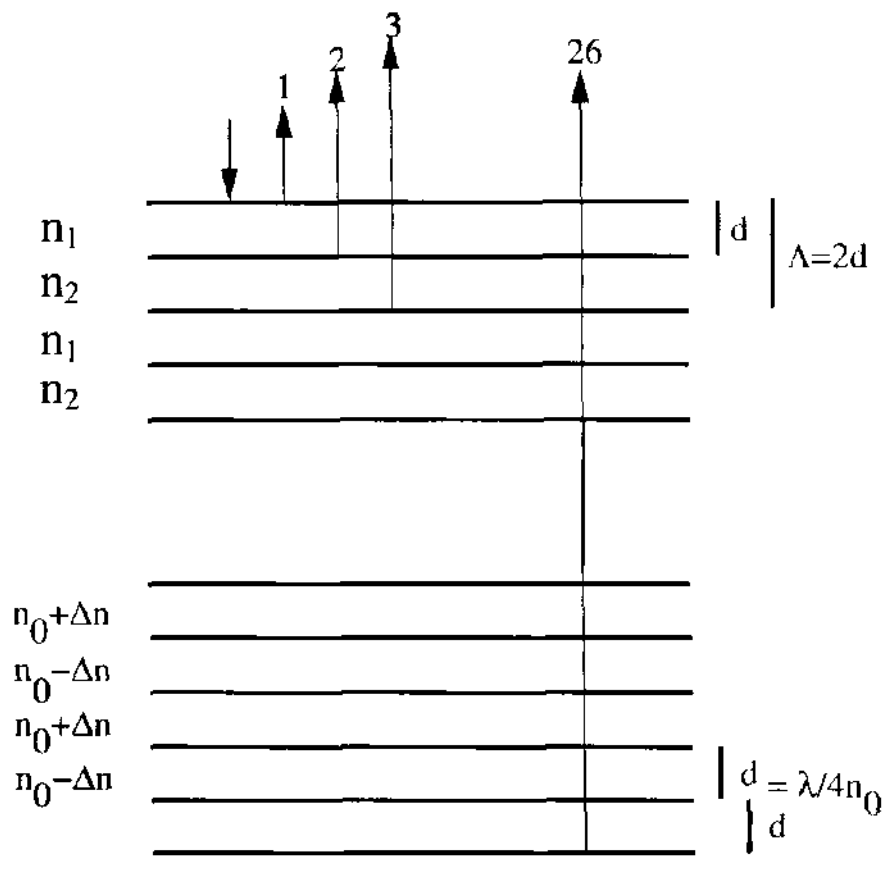

Figure 3.4: Reflectivity from a periodic structure consisting of alternative layers of refractive indices $(n_0+\Delta n)$ and $(n_0-\Delta n)$, each of thickness $d = \lambda_o/4n_0$.

Now if $\Delta n << n_o$, and if we choose the thickness of each layer to be

$$d = \frac{\lambda}{4 n_0} \cong \frac{\lambda}{4\left(n_0 + \Delta n\right)} \cong \frac{\lambda}{4\left(n_0 - \Delta n\right)}$$

Then the reflections arising out of individual reflections from the various interfaces would all be in phase and should result in a strong reflection. Thus for strong reflection at a chosen (free space) wavelength λ_c, the period of the refractive index variation should be

$$\Lambda = 2 d = \frac{\lambda_c}{2 n_0}$$

This is referred to as the Bragg condiction. When the periodic medium is made up of 30 layers (15 periods) then one can approximately achieve reflectivity as high 100%.

3.5 Experimental Procedure:

The device structure shown in Figure 3.1 was fabricated to achieve a low-loss microcavity, with resonant features centered at 7760Å ($<E_g$) by choosing appropriate mirrors, transparent-conducting spacers of desired thickness, and approximately positioning the active semiconducting polymer at the antinode of the calculated optical-field pattern. The device consists of a transparent conducting layer of indium–tin–oxide (ITO) of desired thickness plasma deposited on a distributed Bragg reflector (DBR) constructed for 7760 Å. Regioregular poly-3, octyl thiophene, P3OT blended with 1% weight ratio of the electron acceptor 2, 3-dichloro-5, 6-dicyano-1, 4 benzoquinone in p-xylene solution was spin coated on the ITO. The polymer films coating was of uniform with thickness 500 Å. The top mirror/electrode was a 200 Å gold layer deposited by vacuum evaporation at 10^{-6} Torr. The typical device area was 0.8 mm×0.8 mm.

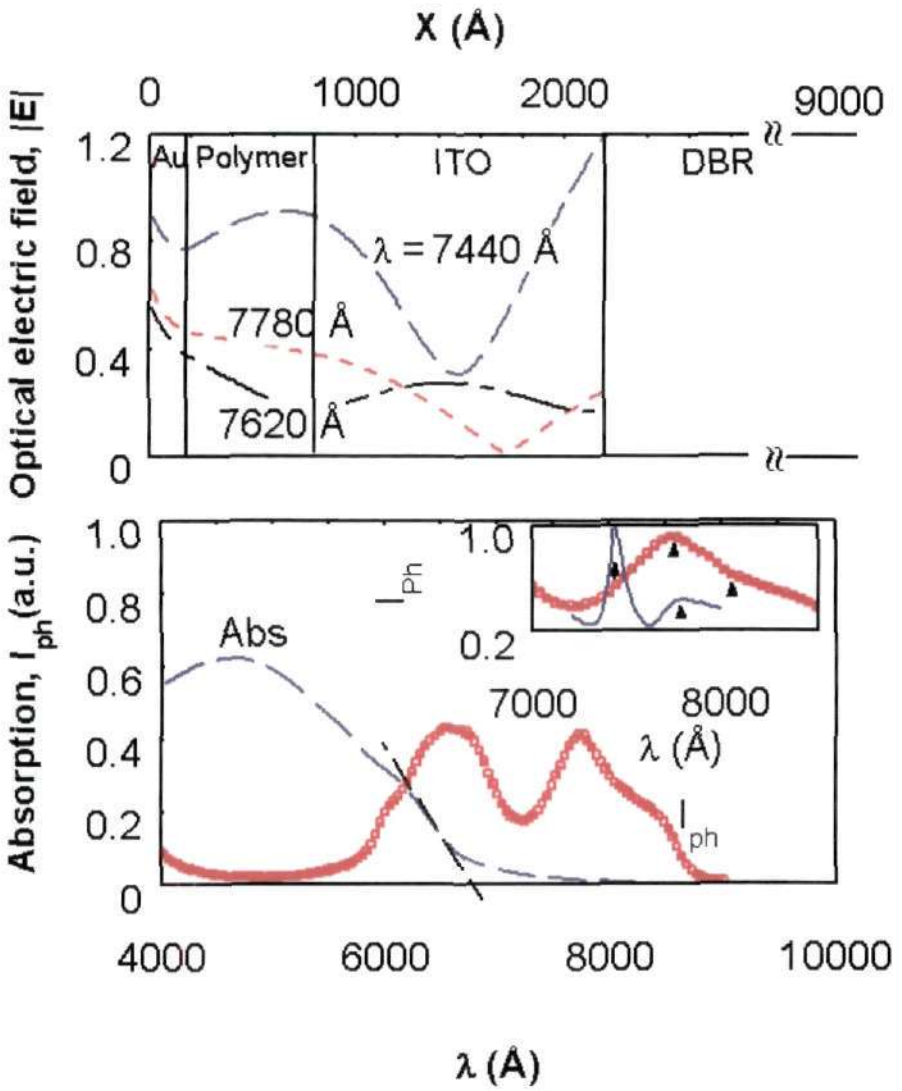

Figure 3.5: (a) Resonance cavity photodiode (RCP) along with spatial variation of optical field for λ =7440 Å , 7620 Å and 7780 Å. 16 pairs of AlGaAs/AlAs layers form the bottom mirror (DBR) with reflectivity of 0.99 at the center wavelength. ITO of 1500 Å forms the spacer and electrode layer, and a semitransparent gold layer acts as the top electrode/mirror. (b) Absorbance (dashed line) of polymer film and $I_{ph}(\lambda)$ of the RCP, inset, also shows results from simulation (solid line) and experiments in resonance region.

3.6 Results and discussion:

The band edge of the polymer film, as determined from the intercept of the tangent corresponding to $|d(\text{absorbance})/d\lambda|_{max}$, near the absorption onset, Figure 3.5(b), is 6800 Å. A substantial I_{ph} in the short-circuit mode of the device was observed even at low-light levels with a responsivity of 50 mA/W. $I_{ph}(\lambda)$ indicates a prominent feature with a local maxima = 7760 Å and width of 900 Å. The response also indicates local maxima at λ= 6600 and 4700 Å. The I_{ph} spectral response of the device is depicted in Figure 3.5(b). The inset in Figure 3.5(b) reveals the significant I_{ph} at the subgap region of the polymer. Interestingly, the substantial I_{ph} observed at the spectral region (10000 Å<E_{ex}<7000 Å) with a local λ_{max} = 7760 Å is significantly redshifted from the photoluminescence/electroluminescence spectral maximum (6850 Å) of the polymer film. The I_{ph} features in the strongly absorbing region, can arise from the nonuniform carrier distribution and is controlled by parameters like, diffusion length, barrier width, and mobility of the charge carriers. We emphasize on the cavity induced I_{ph} centered at λ= 7700 Å and correlate this feature to the calculated intensity pattern at different λ. Assuming $I_{ph}(\lambda)$ as a measure of λ, a shift of 300 Å in the spectral response from the calculated field pattern is observed [Figure 3.5(b), inset]. This discrepancy can partly arise from the experimental parameters such as nonhomogeneities in the coatings, and errors in the values of mobility, α, n, conductivity, reflectance of the bottom mirror, and layer thickness. A detailed modeling of $I_{ph}(\lambda)$ requires the knowledge of barrier and transport parameters. However, the essential feature of expected local maxima at low absorption, which is well shifted from E_g, is obtained experimentally.

The dependence of the $I_{ph}(\lambda)$ peak at 7800 Å on the geometry is also evident from the following studies: (i) $I_{ph}(\lambda)$ variation with DBR mirror substrates tuned to different λ values, (ii) Angular dependence studies of I_{ph}, and (iii) Temperature dependence of $I_{ph}(T)$. In the absence of mirrors, $I_{ph}(\lambda)$ essentially follows the absorbance of the film. Features in the low region appear only in devices with DBR mirror substrates with sizable reflectance. $I_{ph}(\lambda)$ generation efficiency in this spectral region decreases sharply as a function of the angle compared to that of the incident light within the absorbing region (not shown here).

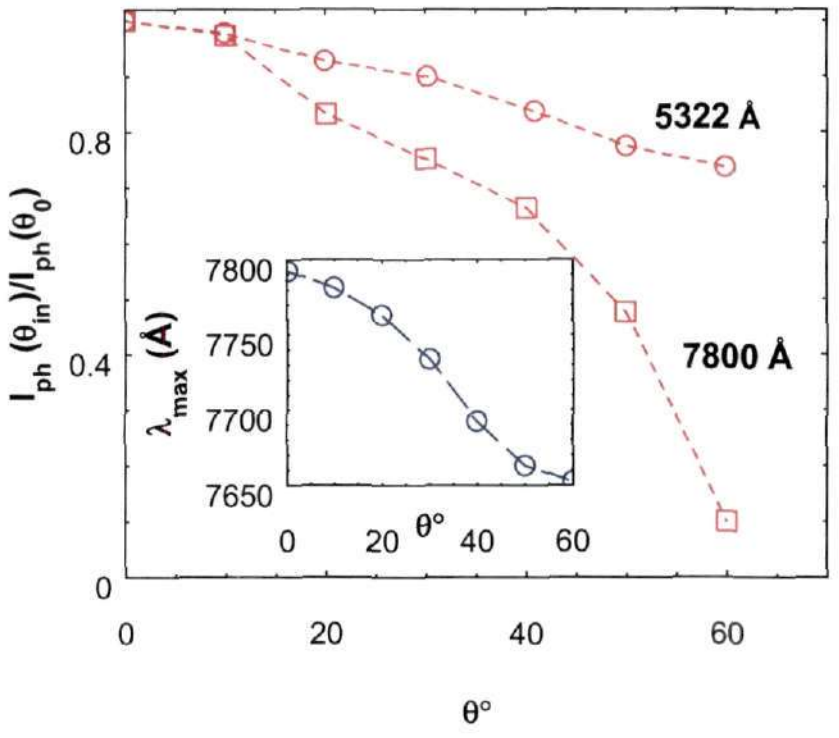

Figure 3.6: I_{ph} as a function of θ_{in} at resonance wavelength and off-resonance wavelength. Inset shows the resonance peak position, λ_{max} of the RCP variation with θ_{in}

Angular dependence of $I_{ph}(\lambda)$ is depicted in Figure 3.6. $I_{ph}(\lambda)$ generation efficiency in this spectral region decreases sharply as a function of angle, compared to that of the incident light with λ in the absorbing (off-resonance) region. Analyzing $I_{ph}(\lambda)$

around the resonant maxima with gaussian fits, we find that the peak value is blue shifted as a function of angle as shown in the inset of Figure 3.6. Analogous results for the angular dependence of emission from microcavity based light emitting devices, are observed by Dirr *et al* [25] with increasing path length as a function of angle inside the cavity. This feature of the blue-shift with angle can be understood simplistically from the modified stationary wave solution

$$2m\pi = 2\beta L_{eff} \cos\theta_{in} + \psi_1 + \psi_2 \qquad (3.9)$$

Ψ_1 and Ψ_2 are the phase changes upon reflection at the gold and DBR mirrors, θ_{in} is the incident angle of light, L_{eff} is the effective cavity length.

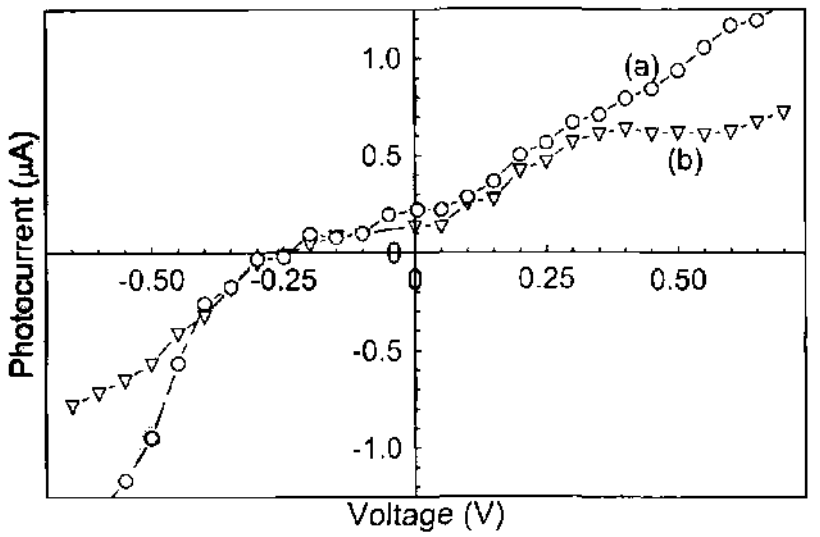

Figure 3.7: I_{ph} as a function of voltage characteristics of RCP, I_{ph} was obtained by measurement of difference of current at dark and light of (a) 1 mw/cm^2 λ= 6321 Å (b) 113 μW/cm^2 λ = 7800 Å. Au electrode biased positive is the forward bias.

The direction of the I_{ph} in the Au|Polymer|ITO device indicates the nature of the photogenerated carriers. The measured photo-induced current indicates that the photogenerated holes in the barrier drift to ITO electrode with the electrons getting transferred to the Au electrode. The I_{ph}-V results shown in Figure 3.7, reveals the

presence of the built-in bias and the sizable short-circuit current. These results are in expected qualitative agreement assuming a Schottky barrier formation at the polymer/ITO interface, a higher hole mobility and the higher work-function of gold relative to ITO. As shown in the Figure 3.7, the responsivity of the detector increases with the bias voltage however at the expense of signal to noise ratio, since the background-dark current increases more rapidly with the bias.

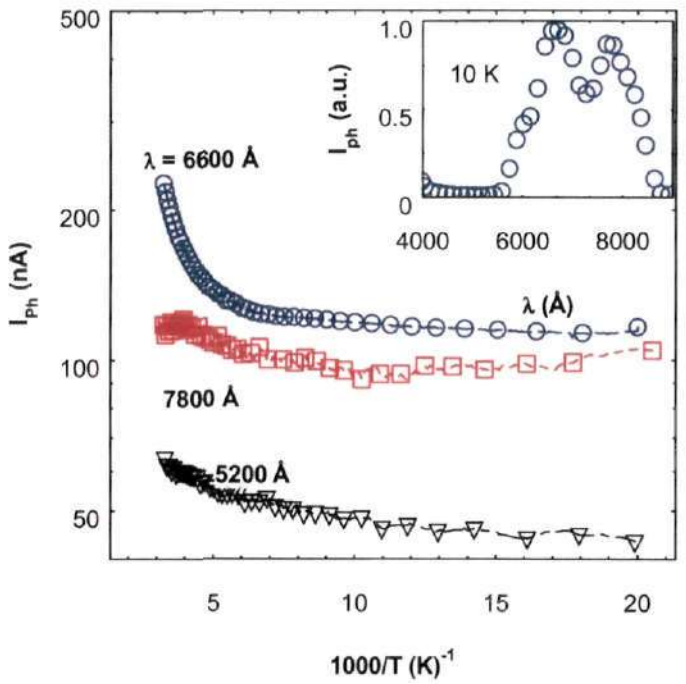

Figure 3.8: I_{ph} as a function of temperature, at RCE λ_c≈7800 Å (a), incident power P_i≈ 160 μW; λ_c≈ 6600 Å (b), P_i≈ 110 μW; λ_c≈ 5200 Å (c), and P_i≈ 100 μW. Inset shows I_{ph} spectral response at 10 K.

Figure 3.8 depicts the temperature dependence of the steady state $I_{ph}(\lambda)$ and the spectral response at 10 K. I_{ph} at λ = 7800 Å varies marginally with T over the entire range. The strongest T dependence of I_{ph} was observed for λ= 6600 Å. I_{ph}(T) irrespective of λ, does not fit to a single activated model over the entire T range. A measure of barrier can be ascertained by how it fits to the single activated barrier model over the limited T

range 300<T<200 K. 4 meV for λ = 7800 Å, 10 meV for λ = 5320 Å, and 25–50 meV for λ= 6600 Å is estimated. At lower T, T<200 K, I_{ph}(T) is nearly independent of T for all λ. The weak T dependence of I_{ph} at sub-gap wavelengths λ= 7800 Å, is indicative of photogenerated transport processes mediated by interfacial gap states, rather than an exclusive thermally assisted transition from the gap states. The temperature-independent steady state I_{ph}(T) in the subgap region reveals the non-applicability of a simplistic Onsager picture for the origin of photogenerated carriers.

The combination of improved speed along with a reasonable gain in the RCP is evident in transient I_{ph} studies. Sizable transient signals were obtained in response to a pulsed laser source tuned to the RCE wavelength 7810 Å, at a moderate photon flux of 10^{10} photons/pulse, without preamplification under short-circuit bias conditions (Figure 3.9). Neglecting processes such as diffusion, the maximum bandwidth that is possible for a 500 Å thick device is estimated to be atleast 1ns. Also the transit time is governed by the properties of the polymer. The number of photogenerated carriers N_e, per pulse can be evaluated by the integral $\int I_{tr} dt$, which results in an external yield ≈1%. The decay curve shown in Figure 3.9 can be represented by a relaxation process consisting of two components with a dominant fast process, $I_{ph}(t) = A \exp(-t/\tau_1) + B \exp(-t/\tau_2)$, where $\tau_1 \approx$ 100 ps and $\tau_2 \approx$700 ps. The entire current, however, completely decays within 1.7 ns, indicating the fast nature of I_{ph}.

The response observed is faster by a factor of 10 than the expected value, based on the predicted transit time calculated from the value of $\sim d^2/\mu V_{oc} \sim 2$ nsec, where V_{oc} is the built-in voltage, and μ is the mobility. A field effect μ as high as 0.53×10^{-2} cm^2-V/sec has been recently obtained in our laboratory for the regioregular P3OT films of thickness

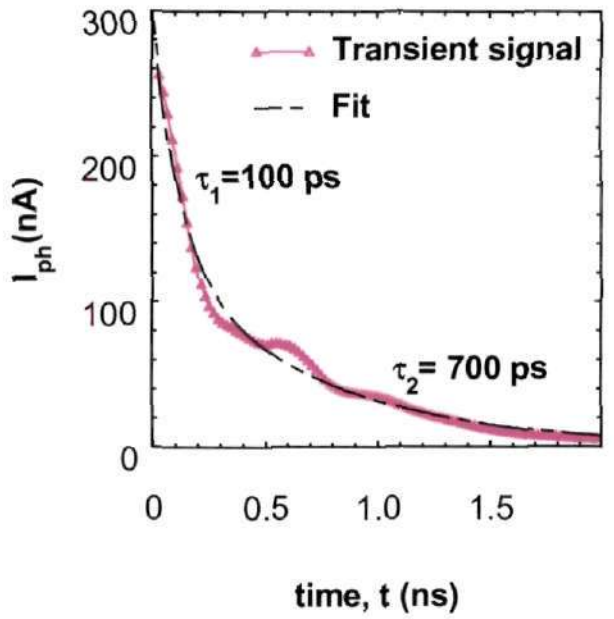

Figure 3.9: Transient short-circuit I_{ph} of the RCP as detected by a 2.25 GHz scope (50 Ω i/p), upon being exposed to 7810 Å laser light with 1.3 ps pulse width, 800 kHz repetition rate, and energy of 2 nJ/pulse. Low-loss 7 GHz, coaxial cable was used to form stable contacts on the metal-padded ITO and Au electrodes. The gold electrode was in contact with a gold-plated extended central conductor of coaxial cable. The dashed line is its fit.

~ 1000 Å in the field effect geometry. A thickness dependent mobility has also been observed [26], with the trap concentration (which affects the mobility) getting reduced considerably for thinner films, thereby increasing the mobility. A possible increase in the mobility and other thin film-effects can probably explain this enhancement of the speed. It is to be noted that this estimate of η can be increased further by optimizing the cavity, or by applying a voltage bias and having an antireflection coating on the top electrode. The detection quantum efficiency is expected to scale with the voltage bias as shown in Figure 3.7. The η, though considerably less than the existing inorganic RCE, is higher than most existing organic photodiodes designed for 0 bias. The highest values of η reported for conventional organic molecular based devices is ~ 75 % at a bias of -10 V

[27]. In the present case, it is to be emphasized that the gain is in the spectral regions where the absorption is considerably low.

Short-circuit current responsivity of 50 mA/W, along with a switching response of 100ps at standard LED/diode laser wavelength, reveals promising applications. This concept of resonant enhancement of I_{ph} was also verified for other semiconducting polymers with different E_g. The features in these detectors can be further enhanced by having an additional antireflection coating, or operating in a reverse bias mode, and even introducing bilayer polymer junctions with the antinodes of the field at the space charge region.

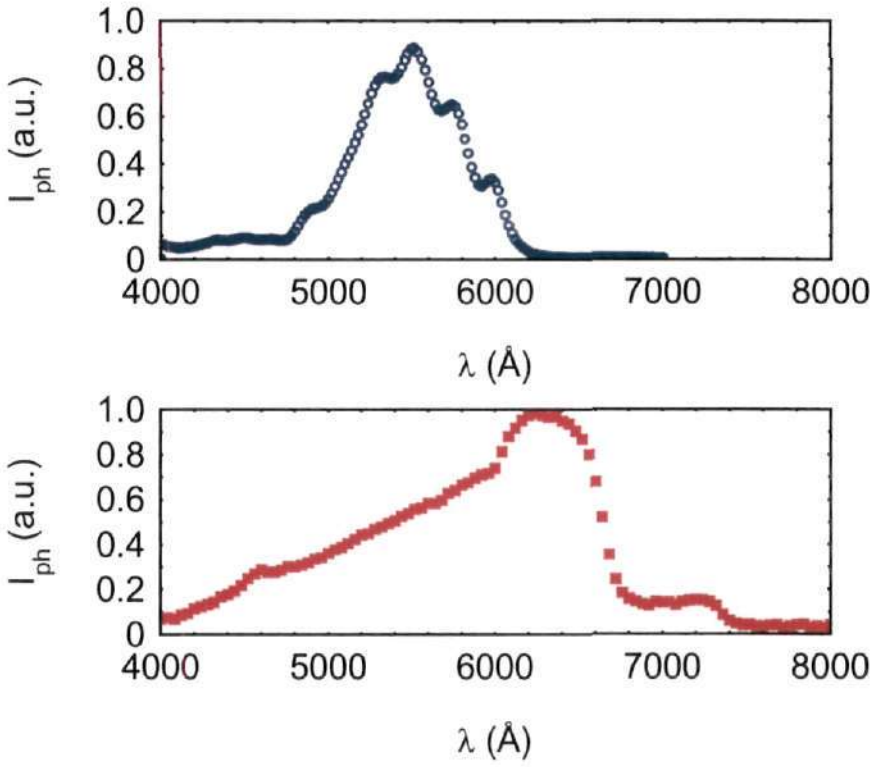

Figure 3.10: I_{ph} (λ) for A: DBR mirror which reflectivity is highest at 5320 Å and B: DBR mirror which reflectivity is highest at 6700 Å.

The results of the DBR mirror tuned to other wavelength are shown in Figure 3.10. The results reveal the tunability of photocurrent spectrum as a function of DBR

mirror reflectivity. Recently our results have been reproduced by Lemmer *et al* [28] who have constructed multilayer thin-film organic microcavity photodiodes with the photoactive layer comprised of a spin-coated conjugated polymer and an evaporated C_{60} layer. They could design a microcavity which allows a simple tuning of the spectral response by varying the layer thickness. They used these devices for studying one and two-photon photocurrents.

3.7 Conclusion:

A micro-cavity photodetector has been demonstrated. Fundamentals of optical field confinement in a micro-cavity is modeled using- (a) Self-consistent method. (b) Real space Method. Theoretical predictions of spectral response of the micro-cavity photodetector have been made. $I_{ph}(\lambda)$ peak at 7800 Å is also confirmed from the following studies: (a) $I_{ph}(\lambda)$ variation with DBR mirror tuned to different λ (b) Angular dependence studies and (c) Temperature dependence studies. Detection of I_{ph} at the sub-gap region of the polymer. I_{ph} varies marginally for the entire range of T : photogenerated transport processes mediated by interfacial gap states, rather than exclusive thermally assisted transition from gap states. Short circuit current responsivity is of 50 mA/W along with switching response of 100 ps. Combination of improved speed, along with a reasonable gain in the micro-cavity photodetector is evident in transient I_{ph} studies. We demonstrated of the tunability of these polymer photodiodes to detect light of wavelength $\lambda > hc/E_g$, approaching the NIR region.

References

1 E. M. Purcell, Phys. Rev. **69**, 681 (1946)

2 R. S. Hullet, E.S. Hilfer, and D. Kleppner, Phys. Rev. Lett. **55**, 2137 (1985); P. Goy *et al.*, Phys. Rev. Lett. **50**, 1903 (1983); F. De Marteni *et al.*, Phys. Rev. Lett. **59**, 2955 (1987).

3 S. Haroche and D. Kleppner, Phys. Today **42**, 24 (1989), H. Yokoyama, Science **256**, 66 (1992); Y. Yamamato and R. E. Schusher, Phys. Today **42**, 24 (1994); S. Haroche and D. Kleppner, Phys. Today **46**, 66 (1993).

4 F. De Marteni and G.R. Jacobovitz, and P. Mataloni, Phys. Rev. Lett. **59**, 2955 (1987).

5 T. Tsutsui, N. Takada, S. Saito, and E. Ogino, Appl. Phys. Lett. **63**, 2032 (1993).

6 N. Takada, T. Tsutsui, and S. Saito, Appl. Phys. Lett. **63**, 2032 (1993).

7 N. Tessler, G. J. Denton, and R. H. Friend, Nature **382**, 695 (1996).

8 S. Karg *et al*, Synth. Met. **54**, 427 (1993).

9 J. H. Burroughes and R. H. Friend, in Conjugated Polymers, edited by J. L. Brédas and R. Silbey (Kluwer Academic Press, The Netherlands, 1991).

10 R. N. Marks *et al.*, Synth. Met. **55-57**, 4133 (1993).

11 I. D. Parker J. Appl. Phys. **57**, 1656 (1994).

12 P. Peumans, V. Bulovic, and S.R. Forrest, Appl. Phys. Lett. **76**, 2650 (2000).

13 J.J. M. Halls *et al.*, Nature **376**, 498 (1995).

14 A. Chin and T. Y. Chang, J. Vac. Sci. Technol. **B 8**, 339 (1990).

15 K. Kishino, M. S. Ünlü, J. Chyi, J. Reed, L. Arsenault, and H. Morkoc, IEEE J. Quanton Electron **QE-27**, 2025 (1991).

16 M. S. Ünlü and S. Strite, J. Appl. Phys. **78**, 607 (1995).

17 S. S. Murtaza, I.-H. Tan, J. E. Bowers, E. L. Hu, K. A. Anselm, M. R. Islam, R. V. Chelakara, R. D. Dupuis, B. G. Streetman, and J. C. Campbell, J. Lightwave Technol. **14**, 1081 (1996).

18 Y. Tzeng, S. S. Li, and P. Ho, IEEE Trans. Electron Devices **40**, 348 (1993).

19 C. H. Seager, M. Sinclair, D. McBranch, A. J. Heeger, and G. L. Baker, Synth. Met. **49**, 91 (1992).

20 N. F. Colaneri, D. D. C. Bradley, R. H. Friend, P. L. Burn, A. B. Holmes, and C. W. Spangler, Phys. Rev. **B 42**, 11670 (1990).

21 D. Vanmaekelbergh and L. van Pieterson, Phys. Rev. Lett. **80**, 821 (1998).

22 I. Kimukin, E. Ozbay, N. Biyikli, T. Kartaloglu, O. Aytür, S. Ünlü, and G. Tuttle, Appl. Phys. Lett. 77, 3890 (2000);R. H. Fowler, Phys. Rev. **38**, 45 (1931).

23 J. R. Chelikowsky, N. Troullier, K. Wu, and Y. Saad, Phys. Rev. **B 50**, 11355 (1994).

24 This datas are directly measured values in our laboratory which is also consistent with data given in the Handbook of Optical constants of solids, edited by E. D. Palik (Academic, London, 1991) and R.H. Friend et al, Appl. Phys. Lett. 81, 2825 (1997).

25 S. Dirr, *et al.*, Adv. Mater. **10**, 167 (1998).

26 D. Moses *et al.*, Phys. Rev. Lett. **80**, 2685 (1998).

27 P. Peumans, V. Bulovic, and S.R. Forrest, Appl. Phys. Lett. **76**, 3855 (2000).

28 R. Koeppe, J. G. Müller, J. M. Lupton, and J. Feldmann, U. Scherf and U. Lemmer, Appl. Phys. Lett. **82**, 2601(2003).

Chapter

4

Metal Semiconductor Metal Structure Devices

4.1 Introduction:

Following the previous chapter on how to achieve high efficient and high speed (>100 GHz) photodetectors we were aiming to achieve such a photodetector from organic polymer. With this in the mind we fabricated an organic polymer based phototransistor without a dielectric gate but having a Schottky metal as an active gate. Unfortunately we could not succeed in realizing the device. This aspect is discussed in detail in the present section of the thesis. Further we found that contact between a low work function metal and polymer does not form an ideal Schottky barrier necessary for achieving such structure devices. We found that on evaporation of low work function metal viz. Al and Mg, a barrier is formed. This barrier depends on the type of the metal evaporated on the polymer. The barrier plays a major role in determining the magnitude of dark as well as photocurrent. We have also found that presence of this barrier introduces a variation in electric field which is suitable for making position sensitive photodetector.

A field effect in organic semiconductors was first reported in 1970 [1]. However, it is only more recently that organic FET (OFET) have been made with attractive performance. The blossoming of OFETs apparently occurred soon after the discovery of conducting polymer, in the late seventies. The first polyacetylene OFET was reported in 1983 [2]. But the issue was really launched just four years later, with a polythiophene-

based device [3]. Almost simultaneously small molecules [4] and particularly conjugated oligomers [5,6], have also proven to be very promising organic semiconductors. But in particular there has not been any significant report on realizing organic metal-semiconductor FET (MESFET). The reason could be the unintentionally formed surface states between the metal-polymer interface. A Schottky type barrier is created by the intimate contact of a low work function metal and a semiconductor surface. A characteristic of a Schottky-type contact is, having a thin depletion layer where the thickness depends on diffusion potential: $\sqrt{(2\varepsilon\varepsilon_0 V_d/eN_a)}$ where, V_d is the diffusion potential and all the symbols have the usual meaning [7]. In doped inorganic semiconductors the charges are delivered via impurity ionization. This gives rise to the formation of a thin schottky-type depletion layer whose thickness depends on the applied voltage. To obtain a thickness in the order of 10^{-5} cm at 1V, carrier density needs to be of the order of 10^{17} cm^{-3}. On the other hand, carrier densities of that order of magnitude are difficult, if not impossible to incorporate in semiconducting polymers. In molecular crystals and modestly clean polymers, donor/acceptor concentrations are too low for formation of thin schottky depletion layers. Band bending in the vicinity of the contacts is therefore, in most cases, negligible [8]. Hence in diodes with PPV and MEHPPV, there is little evidence of a change of depletion width with bias. At the interface formed between Al and polythiophene, Al reacts with both the sulfur atoms and the carbon atoms in the backbone of the thiophene units [9]. The following points can be noted for a metal-organic semiconducting polymer interface: (a) The reverse current does not appear to saturate, contrary to the prediction of the thermionic emission model, this is probably caused by the formation of small interfacial layer between the polymer film and the

blocking contact, (b) The electrical characteristics of the schottky barrier between aluminum and polymer indicate that device is operating in the conventional way, whereby the depletion layer boundary does not move under the influence of the applied bias voltage, and (c) The formation of inversion and accumulation charge layers in a semiconductor device is restricted to semiconductors that are free of defects with energy levels within the semiconductor gap. But interestingly there are reports of formation of Schottky barrier at the Al/PPV interface. The PPV photodiodes prepared by the Bayreuth group [10] appears to be considerably more conducting. The properties of the device studied by this group could be modeled by considering a Schottky barrier junction at the cathode. The observation of a depletion layer at the Al interface and its dependence on the applied voltage allows the estimation of the intrinsic hole concentration as being as high as 10^{17} cm^{-3} [10]. Although the observations for PPV photodiodes of different groups are quite similar, there is still discussion going on regarding the nature of the polymer-metal contacts and especially, on the formation of space charge layer on the Al interface. According to Nguyen *et al* [11] band bending in metal/PPV interface is caused by chemical reaction between the polymer and the metal. Traces of oxygen were found at the metal interface, however, in most of the XPS studies. According to Konstadinis *et al.* [12] oxygen on the surface of the polymer depletes the near surface region of vinylene group, thereby leaving the phenylene groups available for attack by metal atoms. Other models suggest that photochemical oxidation of PPV results in scission of the polymer chain [13] or a possible reaction of the surface layer of Al with PPV to form covalent bonds [8], thereby generating an insulating barrier. Very recently, the results of schottky barrier formation between Al and doped or undoped polythiophene [14-17] and

derivatives of PPV [18] through the rectification ratio of current- voltage and capacitance-voltage characteristics have been widely reported. An easy and good model to describe a polymer diode is the metal-insulator-metal (MIM) model, introduced for light emitting diodes [19]. The polymer is assumed to have a negligible amount of intrinsic charge carriers and can therefore be seen as an insulator. It should be pointed out here, that this assumption is insufficient under illumination. A model based on band bending modified tunneling is developed to explain such a mechanism in the interface [18]. This interfacial region is also thought to be an active region for photo-induced charge generation process in an excitonic framework [20].

In this part of the thesis, we discuss the direct evidence for the formation of charge depleted region upon contacting the polymer surface with certain metals viz. Al and Mg from *in-situ* measurements of lateral conductance, K. The utility of a planar device consisting of Au-ohmic electrodes on the two sides of a schottky-barrier region is demonstrated. An *in-situ* measurement of K between two Au lateral contacts was carried out while depositing Al and Mg patch as well as Au. The K is lowered along with a corresponding increase in photocurrent. Enhanced photo-induced charge generation processes and manipulation of this structure for position sensitive device is also demonstrated. The structure also provides a model system to map the electric field from spatially resolved photocurrent measurements directly, with the resolution controlled by the device dimensions and the optical-probe size. These results are explained through a numerically calculated electric field beneath the electrodes. This structure possesses enhanced photo-induced charge generation processes and manipulation of this structure for position sensitive device is also demonstrated.

4.2 Experimental Details:

Regioregular poly,3-hexylthiophene P3HT obtained from Aldrich were further purified and films of typical thickness ≈ 100 nm were coated on glass substrates in an inert glove box environment equipped with spin-coater. The films were dried at 50^0C for 6 hours and were transferred to an evaporation unit and metal depositions were carried out in hi-vacuum conditions.

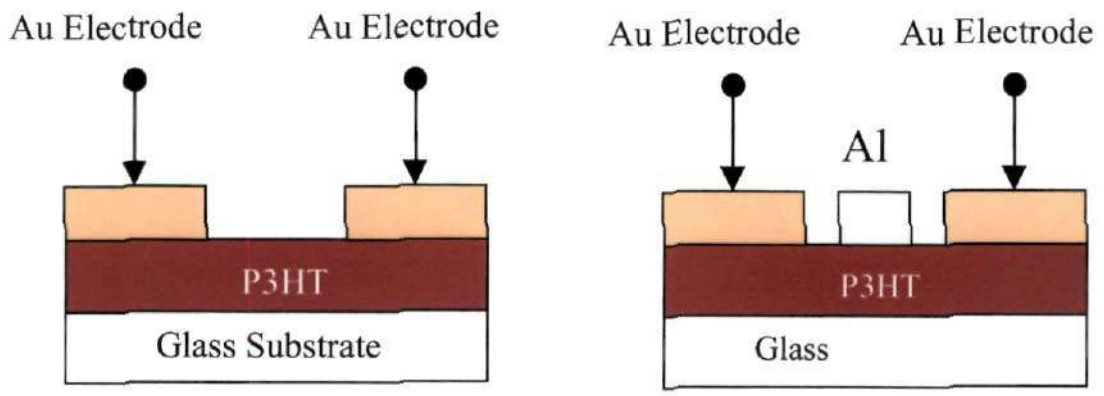

Figure 4.1: (a) Two-terminal planar configuration (b) with aluminum deposited in between two gold electrodes.

Physical shadow masks were used for structures with inter-electrode distances ranging from 60 μm to 1 mm as shown in Figure 4.1. For obtaining inter-electrode lengths in the range 20 - 50 μm conventional photolithography procedures were used to fabricate electrode patterns on glass substrates. The semiconducting polymer was deposited on these patterns for these shorter channel, bottom contact devices. *In-situ* measurements for the top contact structures were carried out in the four probe and two probe geometry in the hi-vacuum conditions. *Ex-situ* measurements were carried out under inert conditions. Photocurrent spectral response $I_{ph}(\lambda)$ was measured with a white-light source coupled to a monochromator using a lock-in technique. Spatially resolved

experiments were carried using a sub-micron stage and He-Ne source, coupled to a fiber, or focussed to a narrow beam spot.

4.3 Results:

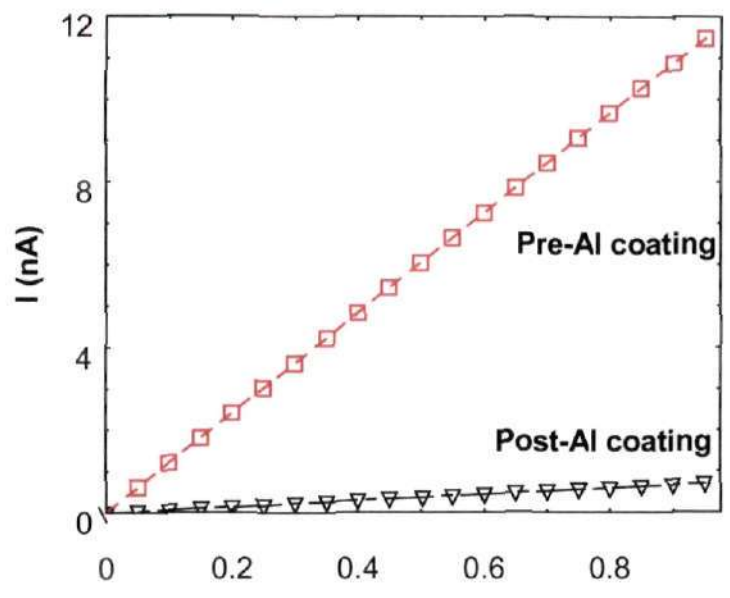

Figure 4.2: I(V) of the P3HT before and after the introduction of the intermediate Al strip in the planar structure with an interelectrode spacing of 1000 μm

I(V) of a typical device exhibited linear characteristics in the voltage range shown in Figure 4.2. The conductivity using a 4-probe setup is $\approx 0.5 \times 10^{-6}$ S/cm. The K measurement between the two lateral Au contacts was carried out in a vacuum-evaporator chamber and was monitored continuously as Al is evaporated on the polymer surface at a symmetrically centered location between the electrodes. Figure 4.3 depicts the results of I(t) during the stages of pre-deposition and post-deposition. The conductance drops by an order of magnitude when the Al strip is introduced. The evolvement of a barrier

formation at the Al/polymer interface is observed, as K decreases gradually over a period of time to an asymptotic constant value.

This particular feature of drop in K with introduction of Al was observed for all structures of different inter-electrode length. Measures were taken to minimize thermal effects of the polymer substrate and diffusion of Al away from the shadow mask region. Microscopic measurements were done to confirm the integrity of the polymer and the well defined area of the Al electrode. The following salient features summarize the set of results from these experiments: (i) The decrease in K, ΔK scales with the area of the Al electrode, (ii) Differential K after Al coating, and the ΔK does not vary significantly over

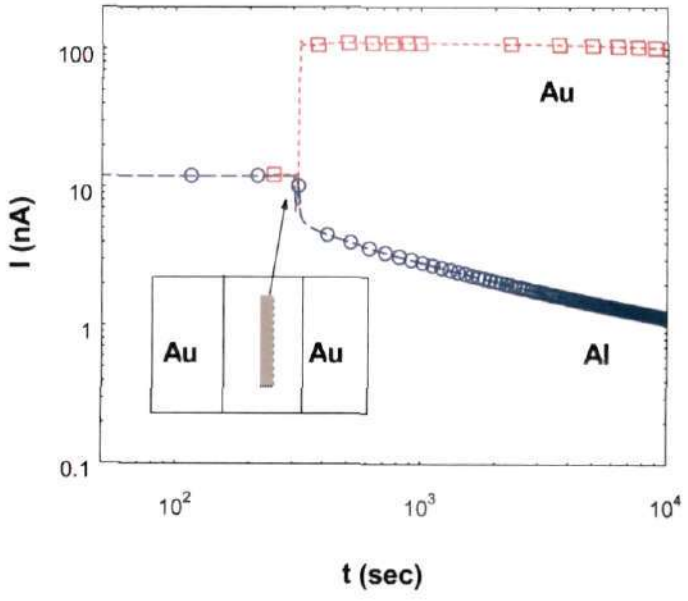

Figure 4.3: I(t) under a constant bias of 2 V in-situ during the deposition of the intermediate Al and Au layer along with a schematic of the structure. The time-dependent measurements were also carried out in the 4-probe geometry with additional two outer electrodes and constant current source, yielding similar results.

the measured voltage range, (iii) When Al is coated on the side opposite to that of the Au electrode (bottom contact geometry) the magnitude of ΔK is reduced (decreases by a factor of 3) but is still significant, (iv) The K between the outer Au electrodes is higher than that between Au and the middle Al electrode in the measured voltage regime, and (v) These results were qualitatively similar when Al was replaced by Mg.

The results are in sharp contrast to the rise in K when a Au strip is introduced in the lateral structure, instead of Al. A drop in resistance is clearly observed in this case for a wide range of size and dimensions of the sample. The K-increase scales with the Au area as expected in a resistor network model.

This set of observations are clearly consistent with the idea of a schottky barrier formation between the low-work function Al and Mg and the p-type P3HT and the resulting charge transfer process upon contact [10-13]. Evaporation of reactive metals such as Al is observed to dedope the polymer at the interface [10,14]. However, it is difficult to reconcile to the magnitude of the K-drop solely based on estimated density of carriers of P3HT $\approx 1.8 \times 10^{16}/cm^3$ and the corresponding depletion width $\approx$ 30 nm. An asymmetric distribution of carriers with higher densities on the surface and the non-uniform electric field E(x,y,z) along with other changes introduced in the polymer due to thermally induced effect can be sources for this discrepancy.

In-situ photoconductance studies reveals that contrast to the decrease in K, the photoconductance of the surface configured structure increases significantly by factor of 3 for post-Al coating (Figure 4.4).

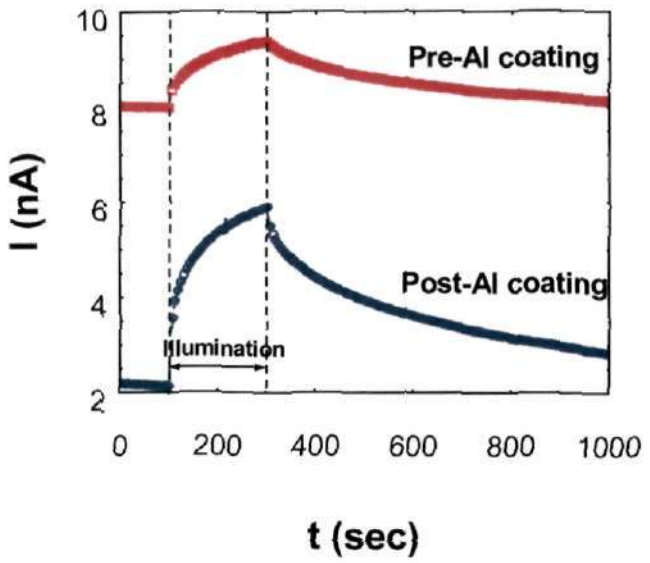

Figure 4.4: *In-Situ* photoconductance measurement of the planer device for before and after the introduction of the intermediate Al strip in the planar structure

The effect of introducing Al is also apparent in spectroscopic and spatially resolved photocurrent measurements. In contrast to the decrease in K, the photoconductance of the surface configured structure increases significantly (by a factor of 10) with improved photoresponsivity as high as ≈ 2mA/W at 10 V bias for the device dimension shown in Figure 4.1. In a conventional 2-terminal surface configuration, the spectral response of $I_{ph}(\lambda)$ follows the absorption curve. Upon introducing the intermediary Al strip, an increase in absolute I_{ph} is accompanied by a red-shifted response around the absorption edge with an appearance of a sharp maximum at 630 nm as shown in Figure 4.5. This peak at the absorption edge can be attributed due to the presence of Al-schottky barrier. The pathway for photocurrent is found to be different from that of dark current. The large E-field associated with the barrier promotes excitonic dissociation of charge carrier generation. The antibatic features have been previously been observed in $I_{ph}(\lambda)$ sandwich configuration involving ITO/P3HT/Al devices and it was speculated

based on the results that Al/polymer was the active region at this low energy spectral region[12,13]. Several theoretical models developed to relate the spectral photocurrent to the absorption were considered, i.e. the model of Ghosh *et al* [20] Tang and Albrecht [21], De Vore [22], Ghosh and Feng [23] and Desormeaux [24]. The first two model [21,22] only consider photoinduced charge carrier generation within a narrow region close to one of the electrode, while the other three models [22-24] solves the diffusion equation to specify boundary conditions. We borrowed the concept of these models for surface cell geometry for our planar device without the middle Al patch. However simulated action spectra calculated by this model is in rather poor agreement with the experimental data except for DeVore's model [22] which takes into account of surface and bulk recombination in the case of planar device structure without Al. Such a photocurrent response can occur because the photocurrent is limited by the most resistive region. weakly absorbed light can penetrate throughout the film and assuming intrinsic carrier generation, generate charge carriers throughout the film. Conversely, strong absorbed light does not penetrate far into the film and, thus, while it can generate a high charge density close to the illuminated side, remainder of the film, beyond a 1/e light penetration depth of approximately 30 nm, is much more resistive. In the present case, light illumination is from the polymer side which is far from the metal-polymer interface. An accurate modeling of the photocurrent in this geometry should involve (i) The diffusion and drift component of both the positive and negative carriers due to the transverse electric field in the bulk region, (ii) The diffusion of the excitons towards the locally high Al/polymer electric-field region, and (iii) The drift/diffusion component of the charge carriers at the polymer-Al interface due to the transverse and vertical field.

These processes are evident from results where a spatially resolved experiments involving a light source is scanned over this structure.

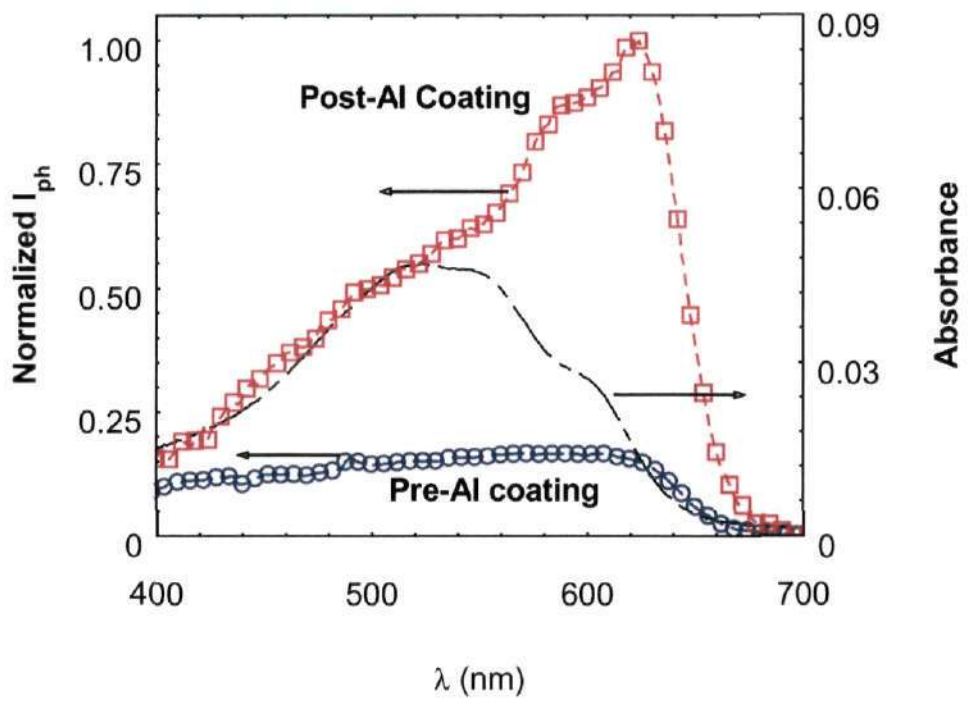

Figure 4.5: The normalized $I_{ph}(\lambda)$ of uniformly-illuminated, planar-surface geometry device without Al (O) and upon introducing the intermediate Al (□) along with the absorbance spectrum (dashed) of pristine P3HT film.

Figure 4.6(b) indicates the $I_{ph}(x)$ measurements for different polarity of the electrode. The $I_{ph}(x)$ results indicate the existence of two local peaks of different in the Al region enveloped by a gradient or a I_{ph} drop as one traverses to the negative polarity. The peaks interchange their positions upon reversing the polarity, revealing an asymmetric aspect of the carrier (holes and electrons) dynamics.

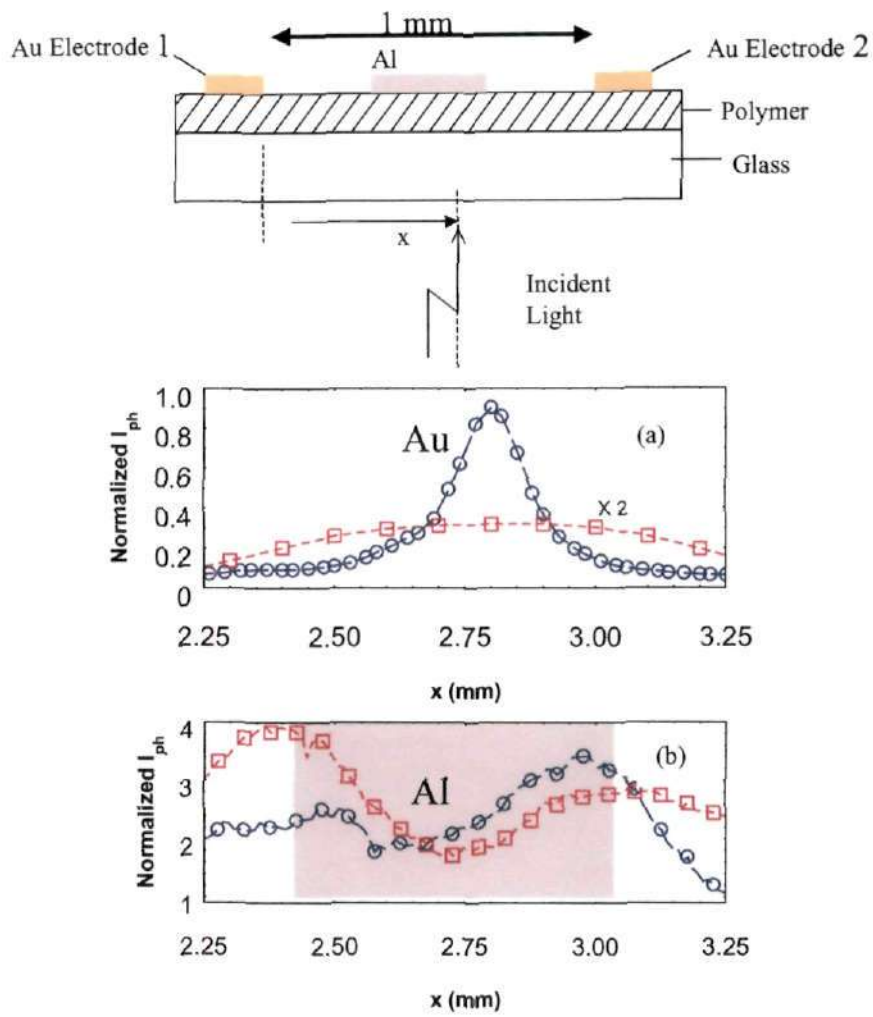

Figure 4.6: Top: schematic illustration of spatially resolved photocurrent measurements. Spatial dependence of the surface geometry $I_{ph}(x)$ using a 50-μm diameter gaussian beam spot using a 630 nm light source, on a 1000 μm -gap scanned over the (a) (□) polymer layer between two gold electrodes, (O) Au strip symmetrically located (width 200 μm) on the polymer layer in between the two Au electrodes, (b) (□) Al strip (shaded area) symmetrically located (width 900 μm) between two gold electrodes with positive polarity on the left side electrode and (O) positive polarity on the right side electrode.

When a constant field is applied and illumination creates free electrons and holes, these electrons and holes have to travel to the opposite electrode. The probability for both the electron and holes to diffuse to the electrodes are higher when illuminated in the center. But when illuminated near the electrode, even though the mobilities are different,

either electron or hole has to take a longer route to reach electrode. Hence magnitude of photocurrent is higher approximately in the center and lesser and lesser at the electrode side.

As the bias voltage increases the peaks merge giving rise to a broad central profile. The $I_{ph}(x)$ can be taken to be a measure of the field variation within the device and provides a system for mapping the electric field. In contrast to this rich $I_{ph}(x)$ variation, Figure 4.6(a) shows variation in a 2-terminal system or a Au-strip modified 2 terminal device When the intermediate gold strip is introduced an additional back reflection component (glass/polymer/Au) is introduced and the spatial I_{ph} follows gaussian distribution around this region.

An important implication of these measurements is that the introduction of the Al/polymer barrier can provide the spatial variation necessary for sensitive position dependent sensing. The patterning of the surface with these barriers along with an optimum choice for the device dimensions and near field optical probing can result in measurable current variation even in 100 nm length scale. Results from a structure similar to a conventional 1-D position-sensing detector (PSD) consisting of a bottom Al electrode and two top Au electrodes, are shown in Figure 4.7. A variation of the difference in the short-circuit-current from the two arms (Au and Al) is observed as a function of the beam position with a minima located at the centre of the interelectrode region. These photo-induced ac measurement studies in conjunction with dc measurements indicate a current path arising from the electron transfer to the Al electrode (enhanced by Al/polymer barrier) and a lateral hole displacement leading to hole transfer across the gold electrode. Transient photocurrent measurements also indicate a

displacement component in the current along with a presence of position-dependent transient profiles.

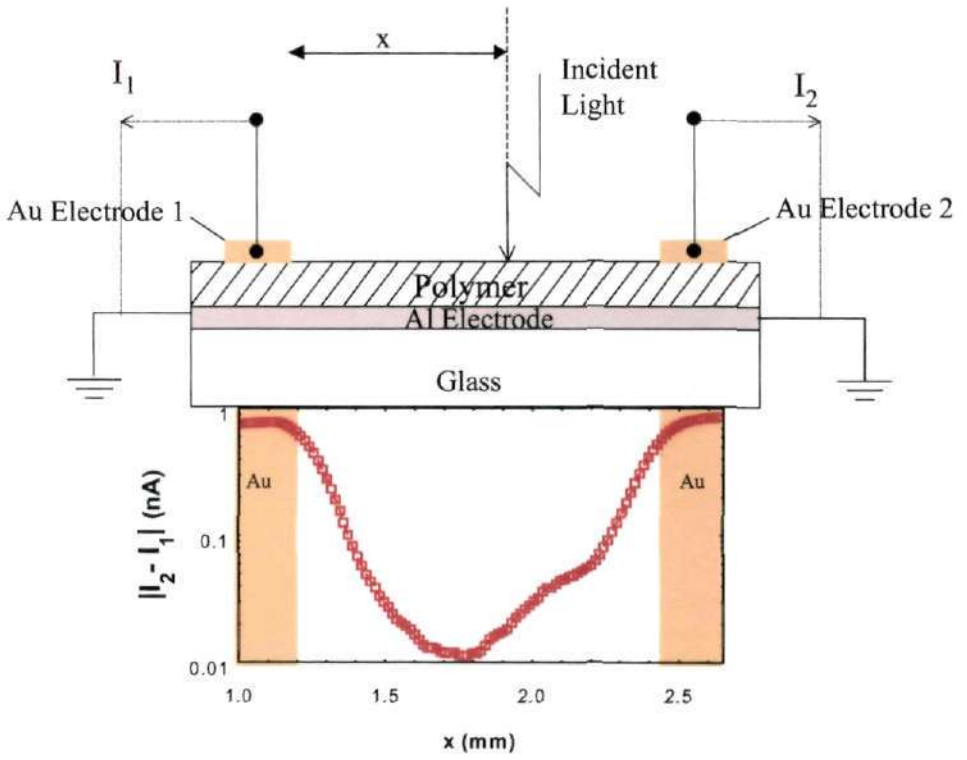

Figure 4.7: Top: schematic illustration of 1D position sensitive detector. Bottom: $I_{ph}(x)$ shown here is I_2-I_1 with Al as common electrode.

4.4 Discussion:

The lateral conductance measurement of two-terminal planar configuration devices shows that Au electrodes forms a good ohmic contact which agrees with the fact that work function of the Au is close to the sum of the electron affinity and the band gap energy of the P3AT. When a very high work function electrode Au is brought into contact with the p-type polymer P3AT, holes will flow from P3AT into the metal to obtain charge equilibrium. This result in a positive space charge zone in the polymer close to the contact and band bending as indicated in Figure 1.10. In practice, however, the Au/P3AT barrier for holes is so small ($\phi_{b,h}=I_p-\chi$ = 5.1-5.0 = 0.1 eV) that it can be

treated as an ohmic contact, where holes can pass the barrier when locally a low electric field has been established. The work functions for Au and Al are average values based on handbook tables and literature reports, which yields ($\phi_{m,Au}$=5.0 eV) and $\phi_{m,Al}$=4.3 eV). The opposite situation occurs at the Al/P3AT electrode, where an electron-injecting barrier $\phi_{b,e}=\phi_s-\chi_s$ = 4.3-2.9 =1.4 eV is established at charge equilibrium. This situation is obtained as a consequence of the flow of electrons from the Al electrode into the semiconducting polymer film, establishing a hole-depletion zone in P3AT at the Al interface. A barrier of 0.7 eV for holes drifting from the polymer layer into the metal contact is established as a result of the interfacial band bending. Our experimental result of lowering of conductance after Al evaporation tells that there exists a build in field at the interface due to Al evaporation. This direction of electric field is found (assumed) to be not only orthogonal but also horizontal. When we apply voltage the outer Au electrode, there is a resultant electric field in the horizontal direction. The magnitude of this electric field goes to minimum at a place where Al is centered. The observation of drop of lateral conductance after Al evaporation is because of this reduction in electric field. For the photoconductance it has been proved that in presence of such a charge depleted barrier and hence electric field, a greater drift velocity of separated charge carriers can drift to the respective electrode with a less probability of reduced rate of carrier recombination. Hence photoconductance increases with Al evaporation. The present results provide a direct validation of these inferences. The magnitude of photoconductance in the present case increases even though dark conductance due to applied electric field is reduced after Al evaporation. This result is valid for light wavelength, which can reach the metal interface, where there is an in-build electric field.

Our calculation shows that this electric field is within the charge-depleted region and is highest in the metal polymer interface and gradually drops to the end of the depleted region. Hence our spectral response tell that in presence of Al there is a photocurrent enhancement of four times for the wavelength of light near to the absorption edge. It is to be noted that the photoconductance measurement is done with light illumination throughout the Al area. Further when we study the spatial dependence of photocurrent we found that electric field beneath these metals plays a very vital role in photocurrent generation. Under the assumptions that under a constant field applied and charge carrier generation due to photoexcitation, to the two-terminal planar configuration the probability of drifting of electron and holes to the respective electrodes are higher in the center of the two electrodes. When we illuminate the light near to one of the electrodes the probability of charge carrier is lesser as it had to travel a longer route before it recombines and annihilates. The lifetime of the charge carriers are given by $\tau = \Delta\sigma/[q(\mu_n+\mu_p)A\Phi$ where $\Delta\sigma$ is the change in conductance, Φ is measured photon flux density, q is the elementary charge, μ_n and μ_p are the electron and hole mobility, respectively, and A is the optical absorption of the sample. This is the reason why we see a maximum photocurrent at the center position between the two Au electrodes and gradually drops near to the electrode. This result is no longer valid when we evaporate Al. Due to presence of in-build field, we have an enhancement in photocurrent generation. Apart from this enhancement the resultant electric field at the center point of the Al position, its magnitude is minimum. Our observation shows a drop of photocurrent at the center point of Al position. The response curve is also asymmetric; it shows a higher photocurrent at the side of applied electric field and interchangeable.

4.5 Model:

A simple analytic model of the metal-polymer junction is presented based on the full depletion approximation. This approximation is obtained by assuming that the polymer is fully depleted over a distance x_d, called the depletion region. While this assumption does not provide an accurate charge distribution, it does provide very reasonable approximate expressions for the electric field and potential throughout the polymer. These are derived in the following section.

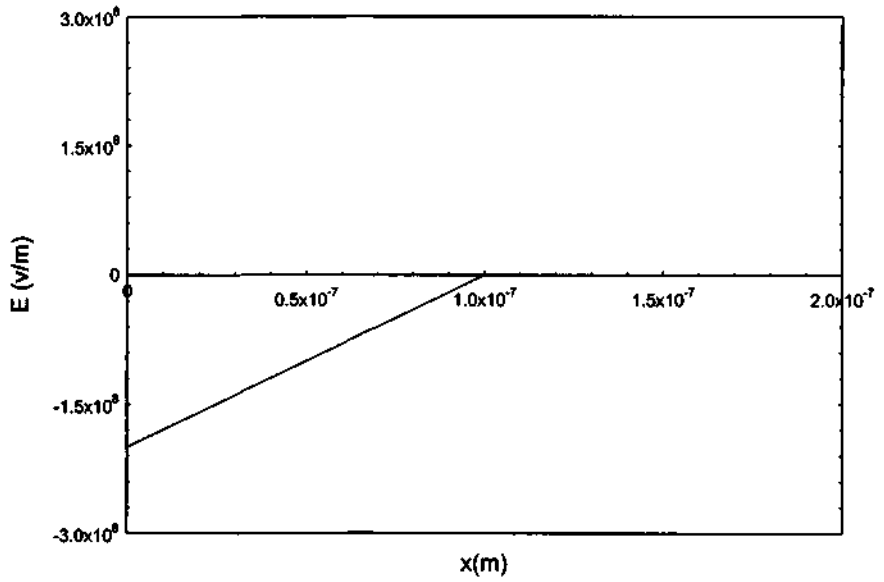

Figure 4.8: Electric field as obtained with full depletion analysis at the Al/polymer interface without considering the oxide layer formed at the interface.

We now apply the full depletion approximation to a metal polymer junction. We define the depletion region to be between the metal-polymer interface ($x = 0$) and the edge of the depletion region ($x = x_d$).

As the polymer is depleted of mobile carriers within the depletion region, the charge density in that region is due to the ionized donors. Outside the depletion region,

the polymer is assumed neutral. This yields the following expressions for the charge density, ρ.

$$\rho(x) = qN_d; \qquad 0\langle x\langle x_d \qquad (4.1)$$

$$\rho(x) = 0; \qquad x\rangle x_d \qquad (4.2)$$

Where we assumed full ionization so that the ionized donor density equals the donor density, N_d. The charge in the polymer is exactly balanced by the charge in the metal, Q_M, so that no electric field exists except around the metal-polymer interface.

Using Gauss's law we obtain electric field as a function of position, also shown in Figure. 8.

$$\varepsilon(x) = -\frac{qN_d}{\varepsilon_S}(x_d - x); \qquad o\langle x\langle x_d \qquad (4.3)$$

$$\varepsilon(x) = 0; \qquad x_d\langle x \qquad (4.4)$$

where ε_s is the dielectric constant of the polymer. We also assumed that the electric field is zero outside the depletion region. It is expected to be zero there since a non-zero field would cause the mobile carriers to redistribute until there is no field. The depletion region does not contain mobile carriers so that there can be an electric field. The largest (absolute) value of the electric field is obtained at the interface and is given by:

$$\varepsilon(x=0) = -\frac{qN_d x_d}{\varepsilon_s} = -\frac{Q_d}{\varepsilon_s} \qquad (4.4)$$

where the electric field was also related to the total charge (per unit area), Q_d, in the depletion layer.

We have calculated electric filed at the interface of Al and Polymer with an assumption: q= 1.602 176 462 x 10^{-19} C and ε= 9 ε_0= 8.854 187 817... x 10^{-12} F m^{-1}, N_d=$10^{24}/m^3$, x_d=10^{-7}m. When we plot this we get a highest electric field of the order of 10^8 V m^{-1} at x=0 (at the interface) and at x=x_d, we get minimum electric field. Hence the field distribution inside the charge-depleted region has a gradient of electric field.

Since the electric field is minus the gradient of the potential, one obtains the potential by integrating the expression for the electric field, yielding

$$\phi(x) = 0 \qquad x \le 0 \qquad (4.5)$$

$$\phi(x) = \frac{qN_d}{2\varepsilon_s}\left[x_d{}^2 - (x_d - x)^2\right] \qquad 0\langle x\langle x_d \qquad (4.6)$$

$$\phi(x) = \frac{qN_d x_d}{2\varepsilon_s} \qquad x_d \le x \qquad (4.7)$$

We now assume that the potential across the metal can be neglected. Since the density of free carriers is very high in a metal, the thickness of the charge layer in the metal is very thin. Therefore, the potential across the metal is several order of magnitude smaller that that across the polymer, even though the total amount of charge is the same in both regions. A more elaborate model of the Schottky barrier contains an interfacial layer between the polymer and the metal. Typically this layer is a thin oxide, with thickness d, which naturally forms on the surface of a polymer during the metal evaporation. The analysis of the Schottky diode can now be repeated using the full depletion approximation yielding the following relation:

$$\phi = \frac{qN_d x_d^2}{2\varepsilon} + \frac{qN_d x_d d}{\varepsilon_{ox}} = \phi_n + \phi_{ox} \qquad (4.8)$$

from which the depletion layer width can be solved. The interfacial layer reduces the capacitance of the Schottky barrier diode and built-in voltage is increased However the potential across the polymer is decreased due to the voltage drop across the oxide layer.

We can calculate the lateral electric field, taking into account of the applied electric filed and in-build electric field:

$$E(x) = \frac{V_o\left|\left(\frac{x_d}{2} - x\right)\right|}{l} - \frac{qN_d}{\varepsilon}\int_0^{-x}(x_d - x)dx + \frac{V_o\left|\left(\frac{x_d}{2} + x\right)\right|}{l} + \frac{qN_d}{\varepsilon}\int_0^{x}(x_d - x)dx \qquad (4.9)$$

Where V_o is the voltage applied across a gap of two electrodes. First term of equation (4.9) describes the build-in electric field and second term is the applied electric field, third and fourth in identical magnitude to first and second respectively but reverse in direction. When we plot lateral electric field we get a parabolic curve with a minimum electric field around at the center of the Al position.

4.6 Outlook:

Although presented results are sufficient to address the initial objective to understand whether formation of charge depletion region at the metal-polymer interface, understanding of the insight physics is far from complete. It will be very interesting and useful to model the device structure with proper boundary conditions. Experimentally, the present limitation of 100 μm optical probe size can be reduced to 1-5 μm. This will give very accurate and most important results of such structure. In order to be able to carry out the analysis of the position-response non-linearity, the current across the contact must be calculated as a function of the position of the incident light beam. To understand more insight physics, one would need a derivation of the PSD equation which involve

solving Lucovsky equation and Lucovsky's differential equation, which derives the lateral photoeffect. Characteristics of PSD (i) Linearity (ii) Dynamic behavior (iii) Noise sources can also be done. Interesting phenomena, like time dependent behavior of PSD viz., dead time and rise time and influence of the time dependent behavior on position determination can be studied.

4.7 Conclusion:

The $I_{ph}(x)$ can be taken to be a measure of the field variation within the device and can provide a system for mapping the electric field. Devices with no middle electrode that the electrode spacing being larger than the incident light spot size, I_{ph} is maximum at the center. When the intermediate gold strip is introduced, an additional back reflection takes place and the spatial I_{ph} follows Gaussian distribution around this region. Barrier formation at Al/polymer and Mg/polymer interface is observed from *in-situ* lateral conductance and photocurrent spectroscopic measurements, along with demonstration of the utility of such structures for 1-D PSD.

References

1. D. F. Barbe, C. R. Westgate, J. Phys. Chem. Solids **31**, 2679 (1970).
2. H. Sirakawa, E. J. Louis, A. J. McDiarmid, C. K. Chiang, A. J. Heeger, J. Chem. Soc. Chem. Commun. **578,** (1977).
3. F. Edisawa, T. Kurokawa, S. Nara, J. Appl. Phys. **54**, 3255 (1983).
4. H. Ebisawa, A. Tsumura, T. Ando, Synth. Met. 1987, 18, 699; A. Tsumura, H. Koezuka, T. Ando Synth. Met. **25**,11 (1988).
5. C. Clarisse, M. T. Riou, M. Gauneau, M. Le Contellec, Elctron. Lett. **24**, 674 (1988).
6. G. Horrowitz, D. Fichou, X. z. Peng, Z. G. Xu, F. Garnier, Solid State Commun. **24**, 381 (1989).
7. E. H. Rhoderick and R. H. Williams in Metal-Semiconductor Contacts, (Clarendon Press, Oxford, 1988).
8. P. Dannetun *et al*, Synth. Met. **55-57**, 212 (1993).
9. K. Yoshino, H. Takahashi, K. Muro, Y. Ohmori and R. Sugimoto, J. Appl. Phys.**70**, 5035 (1991).
10. S. Karg, W. Reiss M. Meiier, M. Schwoerer, Mol. Cryst. Liq. Cryst. **79**, 236 (1993).
11. T.P. Nguyen, V. Masardier, V. H. Tran A. Guyot, Synth. Met. **235**, 55 (1993).
12. A. K. Konstadinidis, F. Papadimitrakopoulos, M. Galvin, R. L. Opila, J. Appl. Phys. **77**, 2645 (1995).
13. F. Papadimitrakopoulos, M. Yan, L. J. Rothberg, H.E. Katz, E.A. Chandross, M. E. Galvin, Mol. Cryst. Liq. Cryst. **256**, 669 (1994).
14. H. Tomozowa, D. Braun, S. Philips, A.J. Heeger, H. Kroemer, Synth. Met. **22**, 63 (1997).

15. E. Kinbara, Y. Kunugi, Y. Harima, and K. Yamashita, Appl. Phys. Lett. **114**, 295 (2000).

16. W. Bantikassegn and O. Inganas, Synth. Met. **87**, 5 (1997).

17. S. Nagamatsu, S. S. Pandey, W. Takashima, T. Endo, M. Rikukawa, and K. Kaneto, Synth. Met. **121**, 1563 (2001).

18. E. Ettdgui, H. Razafitrimmo, Y. Gao, B. R. Hsieh, Appl. Phys. Lett. **67**, 2705 (1995).

19. I. D. Parker, J. Appl. Phys. **75**, 1656 (1994).

20. A. K. Ghosh *et al.*, J. Appl. Phys. **45**, 230 (1974).

21. C. W. Tang, A.C. Albrecht, J. Chem. Phys. **62**, 2139 (1975).

22. H. B. DeVore, Phys. Rev. **B. 102**, 86 (1956).

23. A. K. Ghosh, T. Feng, J. Appl. Phys. **49**, 5982 (1978).

24. A. Desormeaux, J. J. Max, R.M. Leblanc, J. Phys. Chem. **97**, 6670 (1993).